General Disclaimer

One or more of the Following Statements may affect this Document

- This document has been reproduced from the best copy furnished by the organizational source. It is being released in the interest of making available as much information as possible.

- This document may contain data, which exceeds the sheet parameters. It was furnished in this condition by the organizational source and is the best copy available.

- This document may contain tone-on-tone or color graphs, charts and/or pictures, which have been reproduced in black and white.

- This document is paginated as submitted by the original source.

- Portions of this document are not fully legible due to the historical nature of some of the material. However, it is the best reproduction available from the original submission.

IN SITU MEASUREMENTS OF THE MESOSPHERE AND STRATOSPHERE

Charles Croskey

Pennsylvania State University

Prepared for:

Army Research Office

23 January 1976

SECURITY CLASSIFICATION OF THIS PAGE (When Data Entered)

REPORT DOCUMENTATION PAGE

READ INSTRUCTIONS BEFORE COMPLETING FORM

1. REPORT NUMBER: 442	2. GOVT ACCESSION NO.
3. RECIPIENT'S CATALOG NUMBER	
4. TITLE (and Subtitle): In Situ Measurements of the Mesosphere and Stratosphere	5. TYPE OF REPORT & PERIOD COVERED: Scientific Report
6. PERFORMING ORG. REPORT NUMBER: PSU-IRL-SCI-442	
7. AUTHOR(s): Charles Croskey	8. CONTRACT OR GRANT NUMBER(s): DAHCO4-75-G-0031
9. PERFORMING ORGANIZATION NAME AND ADDRESS: The Ionosphere Research Laboratory, 318 Electrical Engineering East Building, University Park, Pennsylvania 16802	10. PROGRAM ELEMENT, PROJECT, TASK AREA & WORK UNIT NUMBERS
11. CONTROLLING OFFICE NAME AND ADDRESS	12. REPORT DATE: January 23, 1976
	13. NUMBER OF PAGES: 130
14. MONITORING AGENCY NAME & ADDRESS (if different from Controlling Office): Information Processing Office, U.S. Army Research Office-Durham, Box CM, Duke Station, Durham, North Carolina 27706	15. SECURITY CLASS. (of this report): NONE
	15a. DECLASSIFICATION/DOWNGRADING SCHEDULE

16. DISTRIBUTION STATEMENT (of this Report)

[illegible] STATEMENT A
[illegible] release;
[illegible] Unlimited

17. DISTRIBUTION STATEMENT (of the abstract entered in Block 20, if different from Report)

Supporting Agencies

18. SUPPLEMENTARY NOTES

DDC
RECEIVED
APR 7 1976
A

19. KEY WORDS (Continue on reverse side if necessary and identify by block number)

D-Region
Chemical Aeronomy
Rocket-Satellite Techniques and Measurements

20. ABSTRACT (Continue on reverse side if necessary and identify by block number)

The operation of a subsonic, Gerdien condenser probe for in situ measurements of the mesosphere and stratosphere is presented. The inclusion of a flashing Lyman α ultraviolet source provides an artificially produced ionization of particular constituents. Detailed theory of operation is presented and the data results from two flights is shown. A great deal of fine structure in mobility is observed due to the presence of various hydrated positive ions. The effect of the Lyman α source in the 35 km region was to dissociate a light hydrate ion rather than produce

DD FORM 1 JAN 73 1473 EDITION OF 1 NOV 65 IS OBSOLETE
S/N 0102-014-6601

SECURITY CLASSIFICATION OF THIS PAGE (When Data Entered)

additional ionization. At the 70 km region, photodissociation of the heaviest ions (probably ice crystals) was also observed.

PSU-IRL-SCI-442
Classification Numbers 1.5.1, 1.9.2, 3.2.2

Scientific Report 442

In Situ Measurements of the Mesosphere and Stratosphere

by

Charles Croskey

January 23, 1976

The research reported in this document has been supported by the U.S. Army Research Office under Grant No. DAHCO4-75-G-0031.

Submitted by:

L. C. Hale, Professor
Electrical Engineering

Approved by:

J. S. Nisbet, Director
Ionosphere Research Laboratory

Ionosphere Research Laboratory

The Pennsylvania State University

University Park, Pennsylvania 16802

ACKNOWLEDGEMENTS

The guidance and encouragement of my adviser, Professor Leslie C. Hale is greatly appreciated. I would also like to thank Mr. Robert Olsen of the Atmospheric Sciences Laboratory at White Sands Missile Range. The assistance of various Personnel of the White Sands Missile Range, NASA Wallops Station, and Poker Flat Research Range is gratefully acknowledged.

This work was supported in part by NASA Grant NGR 39-009-218 and U. S. Army Grant DA AERO DAH CO4-75-G-0031.

Letter on file AF

TABLE OF CONTENTS

LIST OF TABLES

LIST OF FIGURES

ABSTRACT

The operation of a subsonic, Gerdien condenser probe for in situ measurements of the mesosphere and stratosphere is presented. The inclusion of a flashing Lyman α ultraviolet source provides an artificially produced ionization of particular constituents. Detailed theory of operation is presented and the data results from two flights is shown. A great deal of fine structure in mobility is observed due to the presence of various hydrated positive ions. The effect of the Lyman α source in the 35 km region was to dissociate a light hydrate ion rather than produce additional ionization. At the 70 km region, photodissociation of the heaviest ions (probably ice crystals) was also observed.

CHAPTER I

INTRODUCTION

1.1 Nitric Oxide and the Ionospheric D-Region

The formation and composition of the D-region is still only partially understood. This part of the ionosphere is important to shortwave propagation and coupling between the stratosphere and the upper regions of the ionosphere. The ion chemistry involved depends on concentrations and reaction rates which are not completely known. The major ionizable constituent in the 65-90 km region is thought to be the minor constituent, nitric oxide, NO.

D-region ionization is produced by several sources. The major source under undistrubed conditions is thought to be the ionization of NO by solar Lyman α radiation (Nicolet and Aikin, 1960). Under disturbed solar conditions, X-rays become important (Mitra and Rowe, 1972), and at lower altitudes (all altitudes at night) galactic cosmic rays which ionize all species (principally N_2 and O_2) become predominant. The solar Lyman α (1215.7Å) penetrates through a spectral window of molecular oxygen well into the D-region. The crossover between cosmic ray and solar production is typically at 63.5 km (Hale, 1974).

Various theoretical models of the D-region have been formed (Nicolet and Aikin, 1960; Mitra, 1969; Ferguson, 1971). Such gas phase theories predict NO concentrations on the order of 10^7 cm^{-3} or less at 80 km. The few experimental observations have, however, yielded higher values. Barth, 1964, used gamma band resonance fluorescence of the gamma bands of NO to obtain the first in situ measurements (Figure 1.1). Similar measurements made by Meira,

1971, showed more altitude-dependent structure in the ionospheric D-region. Models developed from OGO 4 measurements (Rusch, 1973) show a dip in the profile at 85 km similar to that of Meira. A sunrise measurement (Tisone, 1973) has yielded somewhat smaller results, generally agreeing with that of Barth.

D-region models have been improved (Brasseur and Nicolet, 1973) to include photodissociation of nitric oxide and eddy diffusion, yielding relatively low values of NO, of order 10^7 cm^{-3}. Strobel, 1972, performed calculations which also show low concentrations.

Stratospheric measurements have yielded concentrations in the 10^8 to 10^9 range and higher. Various techniques have been used. Schiff (1974) used the chemiluminescence of NO with ozone. This same technique has been used by Ridley et al. (1973) and Lowenstein et al. (1974). Somewhat different results are obtained by infrared absorption of solar radiation which has been used by Ackerman et al. (1973) and Toth et al. (1973) as well as Fontonelli et al. (1974). Patel et al. (1974) used a balloon-borne spinflip Raman laser to find that the NO concentration at 28 km built up over several hours after sunrise.

One of the few direct NO measurements in the 60 km range has been Pontano and Hale (1970). This experiment used selective photoionization of NO by a flashing UV Lyman α source, which was then observed with a modified blunt probe.

One can also use ionization measurements to compute an NO profile if an observed profile of Lyman α flux is also available (Hale, 1974). This procedure requires that both ion density and electron density profiles are available and requires an estimate of the dis-

sociative electron-ion recombination coefficient, which can then be obtained to fairly good accuracy at the sharp transistion altitude where solar Lyman α production equals the cosmic ray production, since cosmic ray intensities are fairly well known (Neher, 1967). Then one can use a laboratory-measured value of NO photo-ionization cross section with the in situ measurements of the Lyman α flux, electron concentration, and positive ion concentration to determine the apparent NO concentration.

As can be seen from Figure 1.1, the prevailing evidence shows an NO concentration of 5×10^7 cm^{-3} or greater at 80 km. Observed electron concentrations, however, indicate a much lower production rate than such a large NO concentration would allow. As a result, gas phase theories must be modified with transport mechanisms either bringing in NO from above (Brasseur and Nicolet, 1973) or through additional ion loss mechanisms such as water cluster ions (Fehsenfeld and Ferguson, 1969) or collisional attachment of electrons to ice crystals (Chesworth, 1974). Much importance is also placed on NO concentrations in the stratosphere, primarily due to its relationship to the ozone layer. The relation between the production of NO at higher levels and stratospheric NO is not well known.

Not only is the average value of NO important in the ionization of the D-region (and quenching by ozone in the stratosphere) but its day-to-day variations may also explain some of the variability observed in D-region characteristics. For example, the winter anomaly of ionospheric radio wave absorption has been of considerable interest (Bowhill, Mechtly, Sechrist, and Smith, 1967; Sechrist, 1967; Mitchell, 1973). Order of magnitude enhancements of electron densities

in the D-region at mid-latitudes are sporadically observed each winter for a few days at a time. Several explanations have been suggested. One possibility is a change in atmospheric temperature (Shapley and Beynon, 1965; Bossolosco and Elena, 1973). Sechrist (1967) has suggested that a transport of NO either by atmospheric motion or heating could produce a change in the electron production process. Another possibility is a sudden decrease in ice crystal particulates (Chesworth and Hale, 1974). One way to determine the specifics of such interactions is to develop an in situ NO measurement for the mesosphere and upper stratosphere.

1.2 NO Measurements with a Gerdien Condenser

In this work the flashing Lyman α lamp method of Pontano and Hale is incorporated into a Gerdien condenser. The alternate cycles of such a probe permit one to observe the mobility range of the unperturbed medium in comparison to the results of selective ionization produced by a Lyman α source.

Two rocket flights have been completed so far. One was via a Super Arcas from Poker Flat, Alaska, during a post-auroral breakup, high absorption day, March, 1975.

The same general geometry has been used with a more sophisticated telemetry aboard an Astrobee D, launched from White Sands, New Mexico in July, 1975.

Chapter II of this discussion considers the operation of the Gerdien condenser and the photo-ionization technique. Chapter III presents the development of the hardware for this measurement. In Chapter IV the data results and implications are discussed. Chapter

V contains a summary and recommendations for future payload techniques.

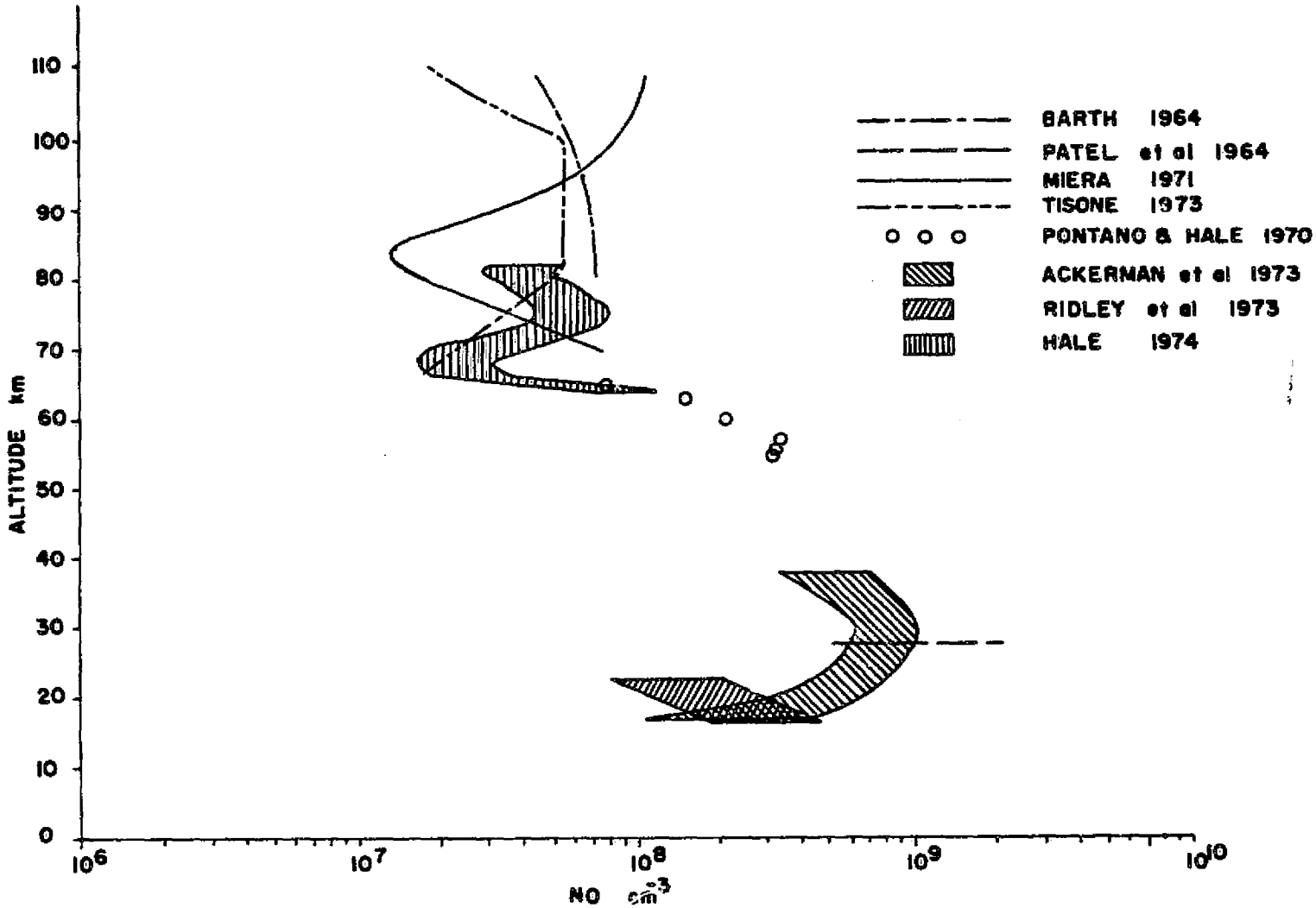

Figure 1.1: Experimental NO Profiles

CHAPTER II

THE FLASHING UV LAMP, GERDIEN CONDENSER

2.1 Gerdien Condenser History

The Gerdien condenser derives its name from its first use by H. Gerdien in 1905. Since then it and its variations have been used for ground-based atmospheric measurements (Israel and Schulz, 1933; Whipple, 1960). It has also been used as a balloon-borne instrument for high altitude measurements (Paltridge, 1965). Rocket-borne measurements have been both subsonic (Pedersen, 1966; Rose, Widdel, and Borchers, 1971) and supersonic (Bourdeau, Whipple, and Clark, 1959; Conley, 1974). Recent mesospheric measurements have shown the presence of two mobility groups between 58 km and 72 km (Rose and Widdel, 1972). These results have been confirmed in a general way by Farrokh (1975). More recent data, for an aerodynamically cleaner Gerdien condenser, shows three or four distinct ion groups (Leiden, 1975).

2.2 Gerdien Condenser V-I Characteristics

The theoretical V-I characteristics of the simple Gerdien condenser geometry shown in Figure 2.1a are well known (Pedersen, 1966). A sweep voltage is applied between the coaxial cylinders and the resulting collector current observed. Figure 2.1b shows the expected V-I characteristic for a single ion mobility gas, while Figure 2.1c shows the result for two types of ions with distinct mobilities.

The geometry used for the payloads under discussion is somewhat different as shown in Figure 2.2. The inclusion of an ultraviolet

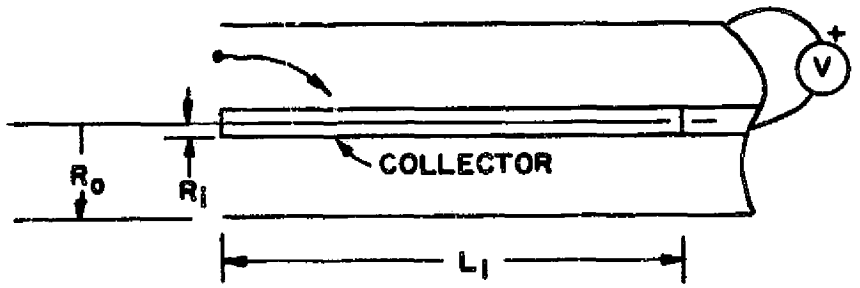

2.1a: Simple Gerdien Condenser

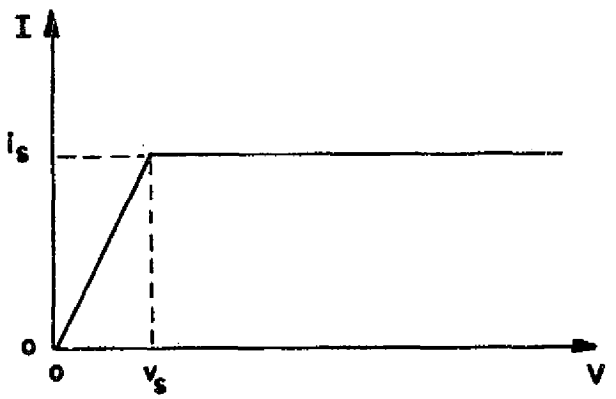

2.1b: Gerdien V-I Characteristic for One Ion Type

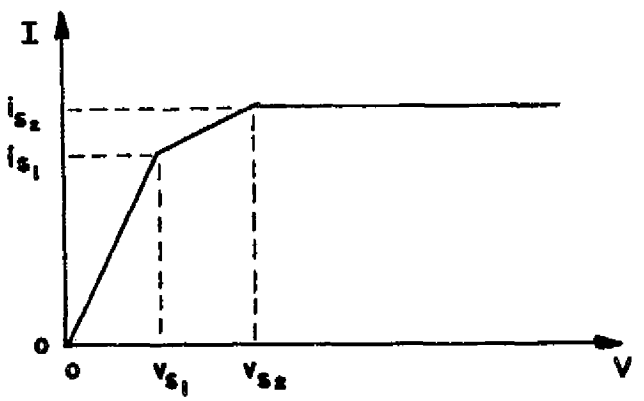

2.1c: Gerdien V-I Characteristic for Two Ion Types

Figure 2.1: The Simple Gerdien Condenser

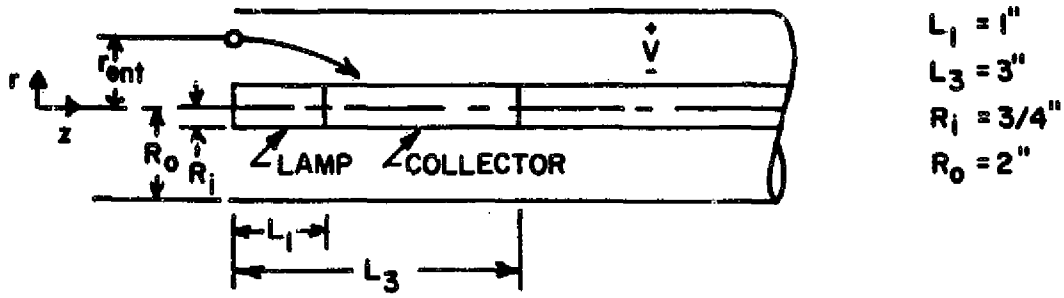

Figure 2.2: Double Condenser with Front Guard Section and Cylindrical Collector

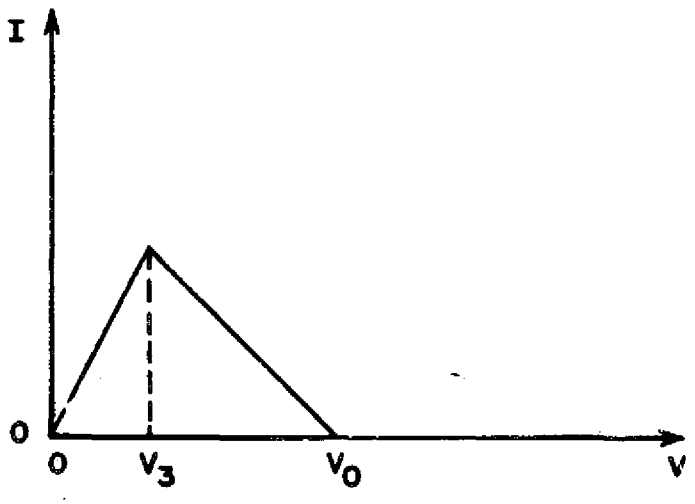

Figure 2.3: Double Condenser V-I Characteristic for One Ion Type

lamp in the center post requires a noseguard section so that self-induced photo-emission will not flow from the collector electrode. The resulting "double condenser" geometry has been analyzed by Blackwood (1920) and Whipple (1960). The relative lengths of the guard section and collector are important, as will be shown later. The expected V-I characteristic can be inferred by considering the net collector current to be a difference between two condenser lengths of L_3 and L_1.

Assuming negligible dynamic flow complications, one can show that a simple Gerdien of collector length L_1 immersed in a single component ionized gas will exhibit a saturation region in the V-I characteristics of Figure 2.1b.

$$i_s = \pi U_z (R_o^2 - R_i^2)\, e\, n \qquad 2.1$$

where U_z is the average flow velocity, e the charge of an electron, and n is the ion density. The voltage necessary to produce this saturation is

$$V_s = \frac{(\ln R_o/R_i)(R_o^2 - R_i^2)}{2L_3\, k}\, U_z \qquad 2.2$$

where k is the mobility of the ion. The linear V-I characteristic is described by a conductance

$$G = \frac{dI}{dV} = \frac{2\pi}{\ln R_o/R_i}\, L_1\, e\, n\, k \qquad 2.3$$

where

$$\sigma = e\, n\, k \qquad 2.4$$

is the conductivity due to that ion.

For the double condenser, the net collector current is the difference between the currents of two condensers of lengths L_3 and L_1. Figure 2.3 shows the result which has a positive conductance region where

$$I = \frac{2\pi}{\ln R_o/R_i} (L_3 - L_1) \, e n k \, V \qquad 2.5$$

and a negative conductance region once "saturation" occurs for distance L_3.

$$I = \pi U_z (R_o^2 - R_i^2) \, e n - \frac{2\pi}{\ln R_o/R_i} L_1 \, e n k \, V \qquad 2.6$$

The voltage needed to produce this saturation is

$$V_3 = \frac{\ln R_o/R_i}{2 L_3 k} U_z (R_o^2 - R_i^2) \qquad 2.7$$

As the applied voltage across the condenser is increased, the ions are swept to the center post more and more quickly until eventually at voltage

$$V_o = \frac{\ln R_o/R_i}{2 L_1 k} U_z (R_o^2 - R_i^2) \qquad 2.8$$

the collector current is zero. Thus the ratio of V_3 to V_o is

$$\frac{V_3}{V_o} = \frac{L_1}{L_3} \qquad 2.9$$

For the geometry used here, the ratio is 3 to 1 so that one may look for such characteristics in the observed data. As will be pointed out later, there are advantages to making this ratio close to unity.

When multiple mobility ions are present, the picture becomes more complicated. Figure 2.4a shows a two-ion type example. The exact shape depends, of course, on the particular mobilities and concentrations. If three ions are present, the result is even more complicated (Figure 2.4b). Letting

$$L_2 = L_3 - L_1 \tag{2.10}$$

the observed conductances are

$$G_1 = \frac{2\pi}{\ln R_o/R_i} (\sigma_1 + \sigma_2 + \sigma_3) L_2$$

$$G_2 = \frac{2\pi}{\ln R_o/R_i} (-\sigma_1 L_1 + (\sigma_2 + \sigma_3) L_2)$$

$$G_3 = \frac{2\pi}{\ln R_o/R_i} (-(\sigma_1 + \sigma_2) L_1 + \sigma_3 L_2)$$

$$G_4 = -\frac{2\pi}{\ln R_o/R_i} (\sigma_1 + \sigma_2 + \sigma_3) L_1$$

$$G_5 = -\frac{2\pi}{\ln R_o/R_i} (\sigma_2 + \sigma_3) L_1$$

$$G_6 = -\frac{2\pi}{\ln R_o/R_i} \sigma_3 L_1 \tag{2.11}$$

By taking the appropriate differences, one can compute the individual σ's. (Since $L_2/L_1 = 2$, this is straightforward.) The mobilities, k_j, are determined by 2.7, and then the concentrations can be found by 2.4. Equation 2.6 can be used with the observed saturation currents as a check, but generally less significant figures are obtained for saturation current values for this geometry with its folded-over V-I characteristic.

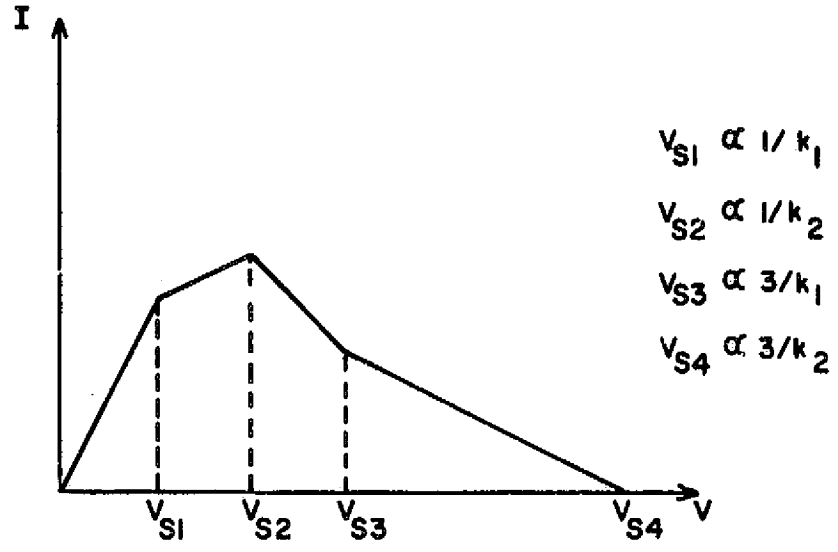

2.4a: Double Condenser V-I Characteristic for Two Ion Types

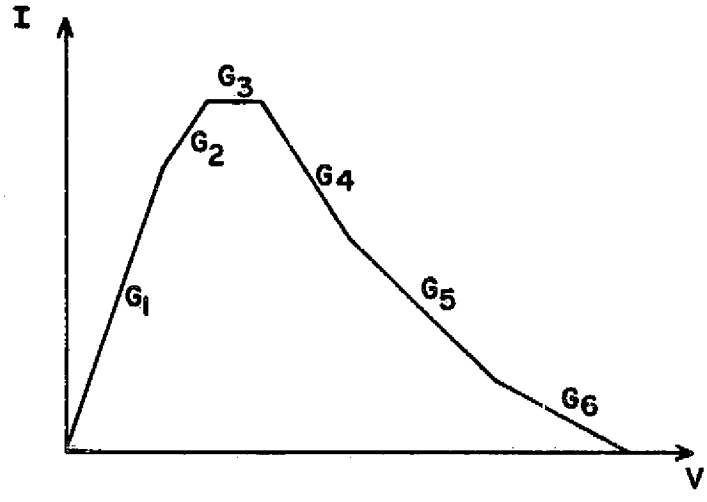

2.4b: Double Condenser V-I Characteristic for Three Ion Types

Figure 2.4: Multiple Ion Types, Double Condenser V-I Characteristics

One can see also that if L_3 is saturated for a small voltage, L_1 will also saturate for a small voltage -- within the experiment range, which further complicates the characteristic. One must be careful of the reverse inflection points due to such effects.

When one talks about a range of mobilities, one can proceed on the basis that a continuous distribution of ionic mobilities might be present rather than distinct groups. The ion concentration, n, then becomes a density function, f(k), the relative frequency of occurrence being dependent on the mobility, k.

The trajectory of an ion entering a radius r_{ent} will be determined by the longititudinal velocity, U_z, and the radial E field set up by the applied potential, V, between the electrodes. Assuming that the space charge is small enough that LaPlace's equation can be used rather than Poisson's equation (Conley, 1974),

$$E_r = - \frac{V}{r \ln R_o/R_i} \qquad 2.12$$

So the velocity in the radial direction is

$$U_r = k_j E_r \qquad 2.13$$

The z and r components of the ion position are related by

$$\frac{dz}{dr} = \frac{U_z}{U_r} \qquad 2.14$$

or

$$dz = \frac{-\ln R_o/R_i}{k_j V} U_z \, r \, dr \qquad 2.15$$

Integrating

$$Z = \int_{o}^{z} dz = -\frac{\ln R_o/R_i}{k_j V} \int_{r_{ent}}^{r} U_z \, r \, dr \qquad 2.16$$

If the ion is farther than distance L_3 down the condenser by the time r reaches R_i, the ion is not collected. Ions entering closer to the center electrode will be caught before ions entering at a larger radius. For a given mobility, k_j, only a fraction of those entering will be caught by the collector. For $r_{ent} < r_j$, the ion is caught; if $r_{ent} > r_j$, the ion is lost. r_j is the critical radius that yields $Z = L_3$ and $r = R_i$ in 2.16.

$$\int_{R_i}^{r_j} U_z \, r \, dr = \frac{k_j V L_3}{\ln R_o/R_i} \qquad 2.17$$

A similar collection mechanism happens for the noseguard section which is of length L_1.

$$\int_{R_i}^{r_j'} U_z \, r \, dr = \frac{k_j V L_1}{\ln R_o/R_i} \qquad 2.18$$

where r_j' is the critical radius for the noseguard. If $r_{ent} < r_j'$, the noseguard catches the ion, etc. The current component to the collector section will be due to ions entering between r_j' and r_j.

$$i_j = e \times f(k_j) \times \text{fraction of ions caught} \qquad 2.19$$

where e is the electron charge and $f(k_j)$ is the aforementioned frequency distribution function, ions cm^{-3} unit mobility^{-1}. Assuming a uniform longitudinal velocity across the face of the condenser,

2.19 becomes

$$i_j = e\,f(k_j)\left[\int_{R_i}^{r_j} U_z\, 2\pi r\, dr - \int_{R_i}^{r'_j} U_z\, 2\pi r\, dr\right] \qquad 2.20$$

Now if U_z is constant down the length of the condenser, 2.17 and 2.18 can be used in 2.20 to yield

$$i_j = e\,f(k_j)\,\frac{2\pi\, k_j}{\ln R_o/R_i}\,(L_3 - L_1)\,V \qquad 2.21$$

If V is large enough, r_j reaches R_o and "saturation" occurs, and then

$$i_j = e\,f(k_j)\int_{R_i}^{R_o} U_z\, 2\pi r\, dr - \frac{2\pi\, k_j}{\ln R_o/R_i}\,L_1\,V \qquad 2.22$$

which is a negative V-I characteristic. Eventually, if V is big enough, all the k_j ions go to the noseguard so that $i_j = 0$.

Equation 2.7 can be used to find the saturation voltage for the k_j ion

$$V_j = \frac{\ln R_o/R_i}{L_3\,k_j}\int_{R_i}^{R_o} U_z\, r\, dr = \frac{\ln R_o/R_i}{2L_3\,k_j}(R_o^2 - R_i^2)\,U_z \qquad 2.23$$

again assuming a constant U_z.

Similarly "saturation" of the noseguard occurs with a voltage

$$V'_j = \frac{\ln R_o/R_i}{2L_1\,k_j}\,(R_o^2 - R_i^2)\,U_z \qquad 2.24$$

These effects can be combined into one equation by letting $\mu(\ )$ be the unit step function. Then,

$$i_j = 2\pi\, e\, f(k_j) \left[\frac{L_2 k_j V}{\ln R_o/R_i} + \left\{ U_z \frac{(R_o^2 - R_i^2)}{2} - \frac{L_3 k_j V}{\ln R_o/R_i} \right\} \mu(V - V_j) \right.$$

$$\left. + \left\{ \frac{L_1 k_j V}{\ln R_o/R_i} - U_z \frac{(R_o^2 - R_i^2)}{2} \right\} \mu(V - V_j') \right] \qquad 2.25$$

Now the total collector current is the sum of each current component due to each mobility k_j.

$$I_T = \int_o^\infty i_j \, dk_j \qquad 2.26$$

Evaluation of Equation 2.26 with 2.25 can be simplified if one realizes that the first step function turns "on" when $V > V_j$

$$V > \frac{\ln R_o/R_i}{2L_3 k_j} (R_o^2 - R_i^2) U_z \qquad 2.27$$

Or, looking at it another way, for a given V, there is a critical value of k, k_c, of k_c for which the step function turns on.

$$k_c = \frac{\ln R_o/R_i}{2L_3 V} (R_o^2 - R_i^2) U_z \qquad 2.28$$

Similarly, the second step function in 2.25 turns on for k_j's $> k_c'$ where

$$k_c' = \frac{\ln R_o/R_i}{2L_1 V} (R_o^2 - R_i^2) U_z \qquad 2.29$$

Equation 2.26 then becomes

$$I_T = 2\pi e \int_o^{k_c} \frac{f(k_j) L_2}{\ln R_o/R_i} V k_j \, dk_j + 2\pi e \int_{k_c}^{k_c'} f(k_j) \left\{ U_z \frac{(R_o^2 - R_i^2)}{2} - \frac{L_1 k_j V}{\ln R_o/R_i} \right\} dk_j \qquad 2.30$$

Also note that by 2.28 and 2.29

$$k_c' = \frac{L_3}{L_1} k_c \qquad 2.31$$

Using 2.31 and 2.28 and then dividing both sides by V, 2.30 becomes

$$\frac{I_T}{V} = \frac{2\pi e L_2}{\ln R_o/R_i} \int_o^{k_c} f(k_j) k_j \, dk_j + \frac{2\pi e L_3 k_c}{\ln R_o/R_i} \int_{k_c}^{\frac{L_3}{L_1} k_c} f(k_j) \, dk_j -$$

$$\frac{2\pi e L_1}{\ln R_o/R_i} \int_{k_c}^{\frac{L_3}{L_1} k_c} f(k_j) \, k_j \, dk_j \qquad 2.32$$

If one now differentiates with respect to k_c, one finds

$$\frac{d(I_T/V)}{dk_c} = \frac{2\pi e L_3}{\ln R_o/R_i} \int_{k_c}^{\frac{L_3}{L_1} k_c} f(k_j) \, dk_j \qquad 2.33$$

Actual data is easier to handle if 2.33 is further reduced by

$$d(I_T/V) = \frac{dI_T}{dV} - \frac{I_T}{V^2} \qquad 2.34$$

and through 2.28

$$dk_c = \frac{\ln R_o/R_i}{2 L_3} (R_o^2 - R_i^2) U_z \left(\frac{-1}{V^2}\right) dV \qquad 2.35$$

to eventually yield

$$\int_{k_c}^{\frac{L_3}{L_1} k_c} f(k_j) \, dk_j = \frac{\left(I_T - V \frac{dI_T}{dV}\right)}{e\pi U_z (R_o^2 - R_i^2)} \qquad 2.36$$

One can now see the importance of the relative lengths of L_3 and L_1. If $L_3 \approx L_1$, the integral can be approximated

$$f(k_c) \approx \left[\frac{L_3}{L_1} - 1\right] \frac{\ln R_o/R_i}{2\pi e L_3} \left[\frac{I_T}{V} - \frac{dI_T}{dV}\right] \qquad 2.37$$

A computerized data analysis is the most reasonable way to handle the derivative.

Note that a U_z term is still present in the k_c term so that the uncertainty of U_z is still a problem. If one makes $L_3 - L_1$ very small, the required electrometer sensitivity and bandwidth increase, so there is a practical limit to the sharpness of the "pointer" that one can obtain. For the payloads presently under discussion, $L_3/L_1 = 3$, so that a relatively broad pointer results. This complicates the data reduction when a continuous range of mobilities (a "smear" in conductivities) occurs (Farrokh, 1975). One can do a similar analysis for the simple single length Gerdien condenser with the result that a second differential of the data is needed.

Similar characteristics can be derived for negative ions except for the presence of electrons. Based on this simple core sample theory, the high mobility electrons would produce a sudden jump in collected current at the applied sweep zero crossing (Pedersen, 1966). In general, however, the data from smaller Gerdiens like that of Farrokh (1975) shows a large negative collected current which is much more angle-of-attack sensitive than the positive ion current. It is thought that this stronger angle dependence is due to a probe voltage with respect to the neutral atmosphere pulling in electrons from a large area, which is in turn

dependent on photo-emission from the outside of the probe produced by solar ultraviolet light. The electron contamination makes negative ion analysis difficult to interpret. By going to a more complex probe geometry, this electron current can be reduced (Rose et al., 1971).

2.3 Selective Photo-Ionization of NO

The first suggestion of selectively ionizing NO with an in situ ultraviolet source was made by R. A. Young in 1963 (Whitten and Poppoff, 1965). Gee (1966) estimated that a source intensity of 10^{14} photons cm^{-2} sec^{-1} would yield an experiment sensitivity on the order of 10^{7} molecules of NO cm^{-3}. Pontano et al. (1970) implemented this approach using a modified "blunt probe." The blunt probe has the advantage of low sensitivity to the angle of attack between the probe and the medium. However, it responds to the average conductivity (Hale et al., 1968). The Gerdien condenser allows one to distinguish between individual ion species, but it has relatively poor resolution in terms of mass numbers. The angle of attack problem with Gerdiens is more severe. One way to stabilize the flow is to fly a ballistic trajectory (Conley, 1974), but the attendant supersonic shock wave may perturb the environment significantly. Recent improvements in parachute design have stabilized the flow sufficiently to now make subsonic measurements feasible.

Pontano's UV lamp was based on microwave discharge in a Krypton-filled microwave cavity. Additional work with such lamps (Siddiqui, 1974) has shown that HF radio waves may also be used to produce the discharge. Generally, such RF sources are more stable and easier to build with solid state devices. Lamps constructed in

this way, utilizing a modified Artech ion chamber as the source, have much longer shelf lives than those used by Pontano.

The Lyman α lamp is turned on for alternate sweeps so that the perturbed medium can be compared to the unperturbed case. The lamp is turned on approximately one second before the sweep commences so that conditions have stabilized before the measurement begins. The net additional ion production due to the lamp depends on the lamp intensity, the attenuation of the Lyman α radiation by atmospheric gasses and the geometry of the system.

The radiation is generated primarily near the end of the center electrode in the lamp chamber so a point source is assumed (Figure 2.5a). r_o is the distance to the magnesium fluoride window. The intensity will decrease with increasing r for two reasons. The first is the normal $1/r^2$ dependence for a point source.

$$n_{vac} = n_o \frac{r_o^2}{r^2} \qquad 2.38$$

would be the expected intensity in a vaccuum where n_o is the measured lamp intensity at r_o. The Lyman α will also be attenuated due to molecular absorption by gasses in the neutral atmosphere. O_2 is the primary absorber of Lyman α in this altitude region (Gee, 1966) so that the differential change in flux passing through a differential distance dr is

$$dn = - n\, n(O_2)\, \sigma_{O_2}\, dr \qquad 2.39$$

where $n(O_2)$ is the O_2 concentration and σ_{O_2} is the absorption cross section of O_2 for Lyman α. Solving 2.39 and remembering that the

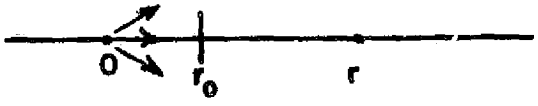

2.5a: Location of the Window with respect to the Point Source

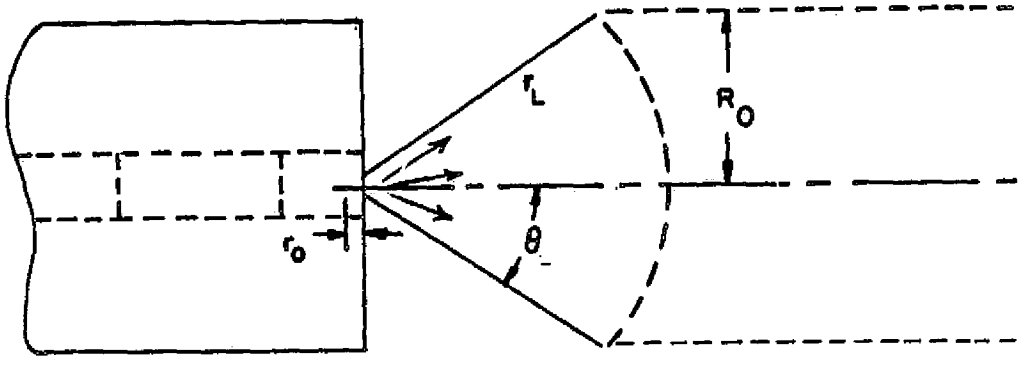

2.5b: Production Volume in which Lyman α Ionization Is Measured

Figure 2.5: Geometry of the Lyman α Radiation from the Probe

intensity is n_o at r_o, one finds

$$n = n_o e^{-n(O_2)\,\sigma_{O_2}\,(r - r_o)} \qquad 2.40$$

Inserting the $1/r^2$ dependence of 2.38, one obtains

$$n = n_o \frac{r_o^2}{r^2} e^{-n(O_2)\,\sigma_{O_2}\,(r - r_o)} \qquad 2.41$$

For the lamps used, r_o is approximately .9 cm, so that at a radius of r = 10.0 cm, the intensity is less than 1% of its initial value. $n(O_2)$ can be estimated by the COSPAR International Reference Atmosphere (1972) as less than 3.7×10^{17} cm^{-3} which is the sum of all constituents at 30 km. $n(O_2)$ decreases with increasing height. Also σ_{O_2} is on the order of 10^{-20} cm^2 (Watanabe, 1958). Therefore, the exponent coefficient is on the order of 4×10^{-3} cm^{-1} so that for $(r - r_o)$ much less than 10^2 cm, a Taylor series expansion for the exponential is possible.

$$n = n_o \frac{r_o^2}{r^2} \left(1 - n(O_2)\,\sigma_{O_2}\,(r - r_o)\right) \qquad 2.42$$

Looking at 2.42, one can see that for r's less than 10 cm the absorption due to O_2 will not be important. Then for all practical purposes

$$n \approx n_o \frac{r_o^2}{r^2} \qquad 2.43$$

Now this Lyman α produces ion electron pairs at a rate dependent on the photoionization cross section of NO, σ_{NO},

$$\frac{dN_{pair}}{dt} = Q = n(NO)\,\sigma_{NO}\,n_o \frac{r_o^2}{r^2} \qquad 2.44$$

where n(NO) is the nitric oxide concentration.

The radiation from the lamp shines forward from the payload (Figure 2.5b) with a beam width of approximately 70^{o}. If there were no fringing fields at the end of the condenser, it would take a straight core sample of the perturbed medium. The total production in this volume is

$$\int Q\, dVol = \iiint n(NO)\, \sigma_{NO}\, n_o\, \frac{r_o^2}{r^2}\, r^2 \sin\theta\, d\phi\, d\theta\, dr \qquad 2.45$$

$$\int Q\, dVol = 2\pi\, n(NO)\, \sigma_{NO}\, n_o\, r_o^2 \iint \sin\theta\, d\theta\, dr \qquad 2.46$$

Let θ_L be the maximum angle from zenith at which the lamp shines (one half the beam width). Let r_L be the corresponding radius which intersects the core surface (Figure 2.5b). The integral then consists of two parts, a spherical conic section out to r_L and a cylindrical section beyond.

$$\int Q\, dVol = 2\pi\, n(NO)\, \sigma_{NO}\, n_o\, r_o^2 \left[(1 - \cos\theta_L)(r_L - r_o) + \int_{r_L}^{\infty} \int_{o}^{\theta_r} \sin\theta\, d\theta\, dr \right] \qquad 2.47$$

where $\theta_r = \sin^{-1} R_o/r$. Then

$$\int Q\, dVol = 2\pi\, n(NO)\, \sigma_{n_o}\, r_o^2 \left[(1 - \cos\theta_L)(r_L - r_o) + \int_{r_L}^{\infty} \left(1 - \frac{\sqrt{r^2 - R_o^2}}{r}\right) dr \right] \qquad 2.48$$

$$\int Q \, dVol = 2\pi \, n(NO) \, \sigma_{NO} \, n_o \, r_o^2 \left[(1 - \cos\theta)(r_L - r_o) + R_o \theta_L + \sqrt{r_L^2 - R_o^2} - r_L \right] \qquad 2.49$$

Since the probe is moving with velocity U_z, at any given time the perturbed medium at the input consists of material ionized at all radii in the volume. The net production of ion-electron pairs per cm^3 is then

$$P = \frac{2\pi \, n(NO) \, \sigma_{NO} \, n_o^2 \, r_o^2}{\pi R_o^2 \, U_z} \left[(1 - \cos\theta_L)(r_L - r_o) + R_o \theta_L + \sqrt{r_L^2 - R_o^2} - r_L \right] \qquad 2.50$$

Here $r_o \approx .9$ cm, $R_o = 5.08$ cm, $\theta_L = 35^o$ so that 2.50 becomes

$$P = .186 \, n(NO) \, \sigma_{NO} \, n_o / U_z \qquad 2.51$$

neglecting any losses due to recombination or attachment.

2.4 Possible Ion Interactions Before Collection

The newly formed ion electron pairs may chemically combine before collection. Certainly some of the electrons will combine with neutral atoms to form negative ions. Both Gee (1966) and Pontano (1970) considered this problem starting with the following continuity equations:

$$\frac{dN^+}{dt} = Q - \alpha_d \, N^+ N^e - \alpha_i \, N^+ N^- \qquad 2.52$$

$$\frac{dN^e}{dt} = Q + \gamma N^- - A N^e - \alpha_d N^e N^+ \qquad 2.53$$

$$\frac{dN^-}{dt} = A N^e - \alpha_i N^+ N^- - \gamma N^- \qquad 2.54$$

where

N^+ = positive ion density

N^e = electron density

N^- = negative ion density

Q = total ion production rate

α_d = dissociation recombination coefficient

γ = negative ion loss coefficient

α_i = ion-ion mutual neutralization coefficient

A = electron attachment coefficient

The ion production rate Q is due to many sources, such as cosmic rays, solar X-rays, and solar Lyman α, as well as the production rate due to the lamp, Q_{lamp}.

Let

$$Q = Q_{norm} + Q_{lamp} \qquad 2.55$$

where Q_{norm} is the non-perturbed production rate.

The production of ion electron pairs by 2.50 may be estimated with $\sigma_{NO} = 2.2 \times 10^{-18}$ cm^2 (Watanabe, 1954) and assuming a lamp Lyman α flux density of 10^{14} photons sec^{-1} cm^{-2}

$$P \approx .2 \times 10^{-7}\, n(NO) \qquad 2.56$$

for a probe velocity of 2×10^3 cm/sec. Then an NO concentration

of 10^{10} cm^{-3} yields $P \approx 200$ cm^{-3} which is large enough to detect at 30 km.

Now the positive ion electron pairs may disappear before they are collected. The ionization produced by the lamp is collected very rapidly. Ninety-nine percent of the ionization is expected within an r on the order of 9 cm, and the length of the collector L_3 is 7.62 cm so that the ion may travel $\approx$ 19 cm at the most before it is collected. Dividing by the probe velocity (in the 100 m/sec to 20 m/sec range) yields a collection time on the order of 2 to 10 msec. This Δt is small enough that the differentials of 2.52, 2.53, 2.54 can be replaced by finite differences.

α_d may be expected to be on the order of 6×10^{-6} cm^3 sec^{-1} and α_i is approximately 3×10^{-8} cm^3 sec^{-1} (Hale, 1974). γ is 10^{-3} or less, depending on the altitude (Cole and Pierce, 1965). The attachment coefficient, A, is the most important quantity and varies with altitude, being on the order of one at 60 km and 10^4 at 30 km (Mitchell, 1973). Below 40 km nearly all the produced electrons will attach to neutrals forming negative ions. Thus,

$$N^- \approx N^+ \approx P \qquad 2.57.$$

Above this height not all the electrons will have time to attach, so

$$N^+ \approx P \qquad 2.58$$

$$N^e \approx P - A N^e \Delta t \qquad 2.59$$

$$N^- \approx A N^e \Delta t \qquad 2.60$$

The effects of the Lyman α source on the possible presence of tiny ice crystals should also be considered. Photo-detachment of

electrons would produce electrons and heavy positive ions. Photo-dissociation of the ice crystals is also a possibility.

2.5 Probe Potential With Respect to the Neutral Atmosphere

The V-I characteristics discussed in Section 2.2 assume that the probe return electrode is held at the potential of the medium. When one is floating freely on a parachute, this may not be so easy to accomplish. If a metallic body is immersed in a plasma, it will take on a negative charge due to the higher mobility of electrons compared to positive ions. But if a large enough area of the payload is exposed to sunlight, the photo-emission induced will drive the probe positive. Similar effects have been considered for the blunt probe (Hale, et al., 1966).

The determination of the probe potential is simplified by the use of an asymmetric probe (Figure 2.2). The outer cylinder of the Gerdien condenser is also a "sunshield" which prevents photo-emission from the collector surface and also shields most of the guard rings from sunlight. The area of the rear guard section exposed to sunlight is small enough, compared to that of the sunlit return electrode, that photo-emission from the guard section can be ignored. The energy of Lyman α photons (10.2 eV) is great enough to generate electrons from the surface of all known metals. The photo-induced electron current which leaves the probe drives the probe positive. As the probe potential becomes positive, the photo electron current decreases.

$$I_{PH} = A_{PH} J_o e^{-\frac{e\phi_r}{V_{PH}}} \qquad 2.61$$

where A_{PH} is the exposed return electrode area (approximately one-fourth of the return electrode area, A_r). J_o is a zero field photo emission and V_{PH} is an average coming from the integral of the photo electron energy spectrum and ϕ_r is the potential of the probe with respect to the medium. Typical values (Bourdeau and Whipple, 1965) are $J_o \approx 6 \times 10^{-10}$ amp cm^{-2} at 70 km, $J_o \approx 2 \times 10^{-10}$ amp cm^{-2} at 50 km and $V_{PH} \approx .3$ volts.

The total current balance of the probe is also affected by the collected ion current. When the collector is receiving positive ions, negative ions are being collected by the return electrode. For a given sweep voltage not all ions are collected, so at any given time a net charge could be collected. One approach is to add an extra set of collector rings at the flow exhaust which have a large enough applied potential to make sure that every ion is collected (Rose et al, 1971). If, however, the photo current of 2.61 is large enough, this will not be necessary. As the probe potential becomes positive, electrons and negative ions will be drawn towards the probe. This current balance the photo current of 2.61.

$$I_{return} = A_n (N^e k^e + N^- k^-) E_r \qquad 2.62$$

where k^e is the effective electron mobility, k^- is the negative ion mobility, and E_r is the field from the return electrode, approximately ϕ_r / L_t, where L_t is the total length of the return cylinder. For the probe dimensions involved, the photo current of 2.61, balanced by 2.62, is large compared to the collected ion current, so that as the collected ion current changes, only a small adjustment in ϕ_r is required. In this way a low impedance connection between

the probe and medium occurs.

The positive probe potential (a few volts or less), which induces a current flow of highly mobile electrons to balance the photo-emission, brings some of these electrons into the core sample measured by the Gerdien, producing the aforementioned spurious, highly angle-of-attack sensitive, large negative currents. The positive and negative ions being more immobile do not have enough time to alter the makeup of the core sample.

If such a probe is used at night, the situation becomes more complicated. Late into the evening there may be scattered sunlight from above, but generally the photo-emission is expected to be zero. The time-varying charge collection of the Gerdien portion of the probe becomes more of a worry. If the probe potential does shift, we should expect a current to the return electrode of

$$I_{return} \approx A_r \, e \, k^{\pm} N^{\pm} \phi_r / L_t \qquad 2.63$$

One can see a large return electrode diameter is important.

At night $N^+ \approx N^-$. If ϕ_r is positive, negative ions will be attracted, etc. Now when positive ions are collected on the center electrode, negative ions are collected by the outer cylinder. Since it has a finite length, similar V-I characteristics can be derived for it. The ratio of mobilities k^-/k^+ is expected to be 1 to 1.2. So the collected currents are expected to be nearly identical. The difference in collected current

$$\Delta I \approx .2 \, \frac{2\pi L}{\ln R_o R_i} \, e \, N^+ k^+ V \qquad 2.64$$

Combining 2.64 with 2.63

$$\phi_r \approx .2\ L\ V/(R_o \ln R_o/R_i) \qquad 2.65$$

So for typical dimensions $\phi_r/V = .36$, this may indeed be a problem. The impedance connection to the medium is not particularly low. For a more detailed calculation one should be more precise than the approximation of 2.63. An iterative data reduction will probably be necessary. Find an approximate mobility ratio; use 2.65 to re-evaluate the potentials, etc., similar to the procedure used for nighttime blunt probes (Hale, 1967).

2.6 Fringing Fields

So far the discussion has assumed that the E field is given by 2.10. At the entrance to the condenser, fringing fields will occur, and the effect on the V-I characteristic may be noticeable (Knoll et al, 1964; Pedersen, 1966). Several schemes may be used to reduce this effect. A double outer cylinder can be used with the sweep applied between them (Conley, 1974), but this also produced some fringing. Even more complex structures (Rose et al, 1971) can be used, which generally need to be empirically optimized with wind tunnel measurements. If the center electrode is made recessed as in Farrokh (1975) fairly flat saturation characteristics are observed. The linearity of the V-I characteristic in "saturation" can be used as an indication of the severity of this problem.

2.7 Flow Dynamics

The actual flow velocity inside the condenser may not be the simple descent velocity. The aerodynamics involved are complicated.

Fortunately, the mean free path of an atmospheric molecule is small enough compared to the probe diameter so that the flow is a continuous flow below 70 km. Molecular collisions are the dominant process and some attempt at the flow dynamics can be made (Farrokh, 1975). The boundary layer which results grows in size down the length of the cylinder. The reduced velocity within the boundary layer will make the collection of the ions easier, but the faster moving ions down the center core are more difficult to collect. The two effects somewhat cancel, probably making saturation easier. A non-linear "S" shaped curve would be expected to be added to the linear V-I characteristic. The flatness of the observed V-I characteristics will give an indication of the severity of this problem. The smaller Gerdien of the type used by Farrokh has not shown any such observable characteristics.

If the flow is supersonic, the attendant shock wave makes the flow even more complicated (Conley, 1974) and the temperature jump produced by the shock wave may change the chemistry of the core sample. While a parachute system insures subsonic measurements in the lower mesosphere, there is insufficient drag at high altitudes to slow the payload very much. Depending on the altitudes of the payload deployment, the probe may become almost supersonic before atmospheric drag slows it down. In addition, at deployment the probe has a horizontal velocity component from the launch. Once the parachute starts to function, this component is reduced as the parachute "catches the wind" and thereafter follows with the wind. There can be much uncertainty in the flow velocity above this region unless one uses a much larger class of payload which includes a flow

meter to measure the actual flow velocity (Rose et al, 1974). Considering these uncertainties, the best approach is to use the vertical descent velocity as deduced by ground-based radar, accepting more uncertainties in the results at the high end.

CHAPTER III

PAYLOAD DESCRIPTION

3.1 Super Arcas Payload

The Super Arcas payload is a flashing UV, Gerdien probe, which has evolved in a number of stages. This payload shows its lineage from the blunt probe (Mitchell, 1973). A block diagram of the probe is shown in Figure 3.1. An internally-generated sweep waveform is applied between the collector and the outer return electrode. A high gain feedback electrometer maintains the collector at the guard potential and transforms the ion current to an output voltage. An automatic range switching amplifier amplifies the electrometer by a gain of either one or twenty before it is applied to the telemetry VCO. Auxiliary circuits are used to sense the zero crossings of the sweep and electrometer (to help define the "contact" potential of the payload with respect to the medium). This zero crossing information is superimposed on the telemetry as positive and negative going glitches. The telemetry is the same as used in the blunt probe, i.e., a 1680 MHz pulse modulation compatible with the standard MRN temperature systems. The RCA pencil triode is pulsed off for 30 μsec by the VCO at a repetition rate linearly related to the VCO input. A 2000 Hertz maximum repetition rate was used, so the received video is tape recorded at the site for playback later through a tachometer. A flip-flop is used to turn on and off the Lyman α lamp on alternate sweeps. The UV lamp consists of a 175 MHz solid state oscillator which drives a modified Arnech ion chamber. Cancellation of the dV/dt current produced by the sweep generator is accomplished by inverting the

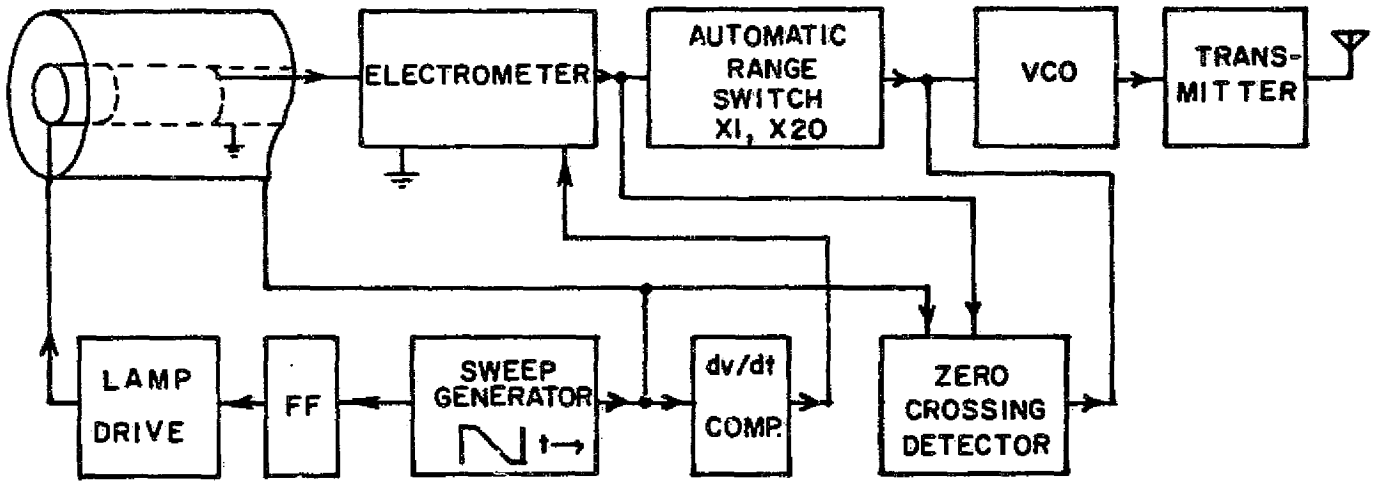

Figure 3.1: Lyman α, Gerdien Condenser Probe

sweep and applying it through a similar capacitance to the electrometer input.

The electrometer circuit is shown in Figure 3.2a. Large meg ohm value resistors are used for the feedback resistor and calibration resistor. While such high value resistors are necessary to obtain the desired sensitivity, they behave somewhat like a delay line due to distributed capacitance and reduce the expected electrometer response time.

The frequency compensation network, β, is used to improve the frequency response. Consider the circuit of Figure 3.2b which includes the shunt and stray capacitances. I_{in} is the ion input current. By Kirchoff's current law,

$$I_{in} + s\,C_{in}\,V_{in} + \frac{\beta V_o + V_{in}}{Z_f} = 0 \qquad 3.1$$

or

$$I_{in} + s\,C_{in}\,V_{in} + \frac{(\beta V_o + V_{in})}{Z_f}\,(1 + s\,\tau_F) = 0 \qquad 3.2$$

where $\tau_F = R_F\,C_F$.

Rearranging

$$R_F I_{in} + (1 + s\,\tau_{in})V_{in} + \beta V_o (1 + s\,\tau_F) = 0 \qquad 3.3$$

where

$$\tau_{in} = (C_{in} + C_F)R_F$$

Now

$$V_o = \frac{A_o}{1 + s\,\tau_A}\,V_{in} \qquad 3.4$$

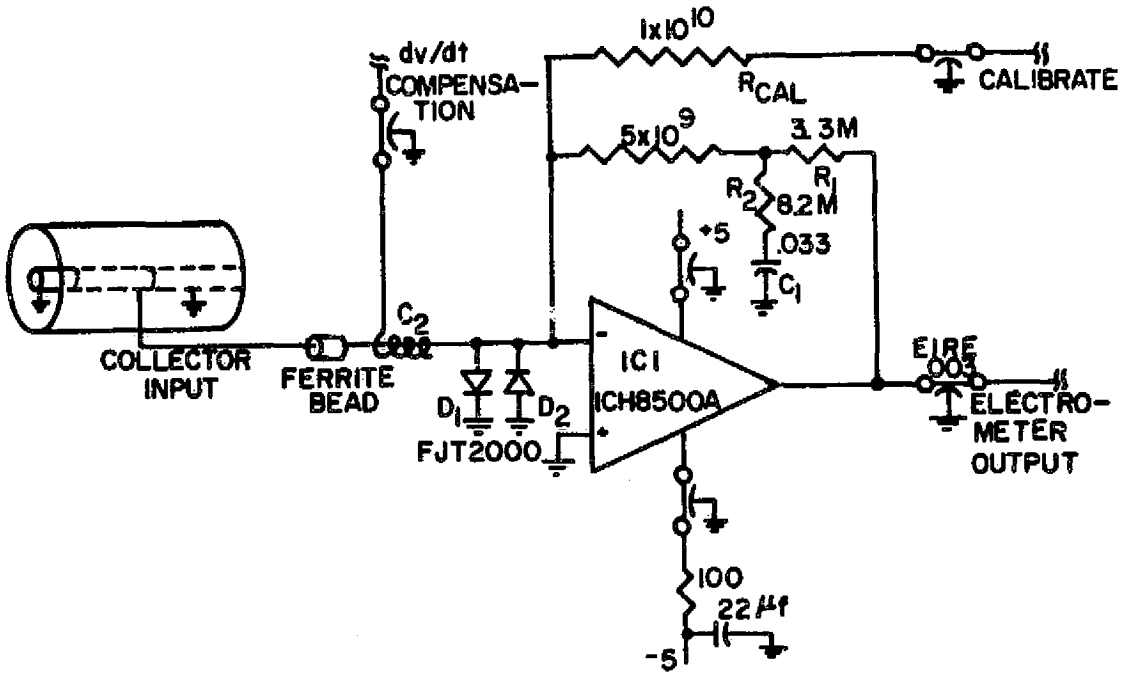

3.2a: Electrometer Used in Super Arcas Payload

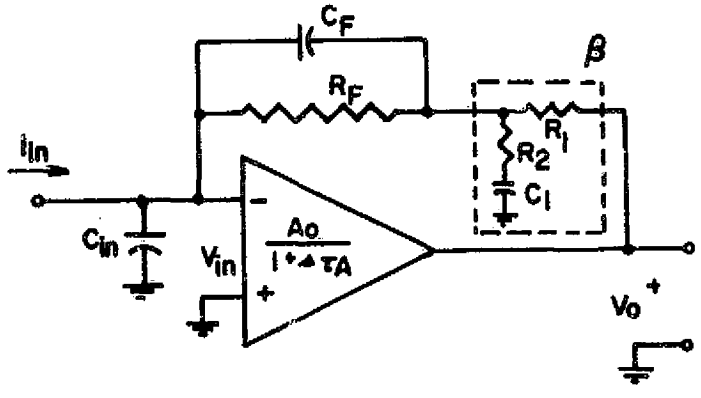

3.2b: Electrometer Equivalent Circuit

Figure 3.2: Electrometer Circuits

where A_o is the DC open loop gain of the electrometer IC1 and τ_A is its time constant.

For the lightly loaded compensation network, the voltage transfer function is

$$\beta = \frac{1 + s\tau_2}{1 + s\tau_{12}} \qquad 3.5$$

where $\tau_2 = R_2 C_1$ and $\tau_{12} = (R_1 + R_2) C_1$.

Then 3.3 becomes

$$V_o = \frac{-R_F A_o I_{in}}{(1 + s\tau_{in})(1 + s\tau_A) + A_o \frac{1 + s\tau_2}{1 + s\tau_{12}} (1 + s\tau_F)} \qquad 3.6$$

Now, if we pick $\tau_{12} = \tau_F$,

$$V_o = \frac{-I_{in} R_F A_o / \tau_{in} \tau_A}{s^2 + s \frac{\tau_{in} + \tau_A + A_o \tau_2}{\tau_{in} \tau_A} + \frac{A_o + 1}{\tau_{in} \tau_A}} \qquad 3.7$$

The purpose of R_2 now becomes apparent. The system is usually lightly damped when one chooses $\tau_{12} = \tau_F$. The inclusion of R_2 permits one to add damping through τ_2 and obtain a reasonable rise time with small overshoot.

Unfortunately, the distributed RC delay line characteristic of the large meg ohm resistors increases the order of the system even more, and less than optimum response times are usually obtained.

Some laboratory success has been obtained with a driven resistive shield around the feedback resistor. A 5-watt, porcelain, wire-wound resistor is about the right size. The end next to the

electrometer is grounded, and the other end is driven with the potential from the β network. Unfortunately, the placement of the shield resistor along the length of the high value resistor is critical.

The MOSFET input stages of the electrometer are protected from static high voltage breakdown by diodes D1 and D2. The calibration resistor R_{cal} is grounded during the flight. During a preflight ground calibration, this resistor is connected to the sweep, so R_{cal} becomes a known "R_{ion}." The dV/dt compensation is applied through C_2, a "gimmick" capacitor.

The electrometer output is range-switched by IC2 (Figure 3.3). Comparators IC3 and IC4 determine the range of the input signal and set the gain appropriately. Comparator trip points are set so that for a typical positive conductance, the transitions are symmetrical. Electrometer and sweep zero crossings, sensed by comparators IC5 and IC6, generate alternate polarity spikes which are summed into the telemetry channel by IC7.

The telemetry system of Figure 3.4 comes directly from the blunt probe. It produces 10 volt negative going pulses which key off the coaxial cavity pencil triode oscillator at a repetition rate linearly related to the VCO input. The antenna is a $\lambda/4$ cavity-backed slot antenna wrapped around a drawn aluminum can which also houses the electronics (Cuffin, 1965). Since a metal extended nose cone was needed, the slot antenna was below the end of the cylindrical extension during the flight upleg. No data is recorded during the upleg, but enough signal to maintain track is needed, so an additional quarter wave skirted monopole was fastened into the tip of the nose cone. A short piece of coaxial cable connected this auxiliary antenna

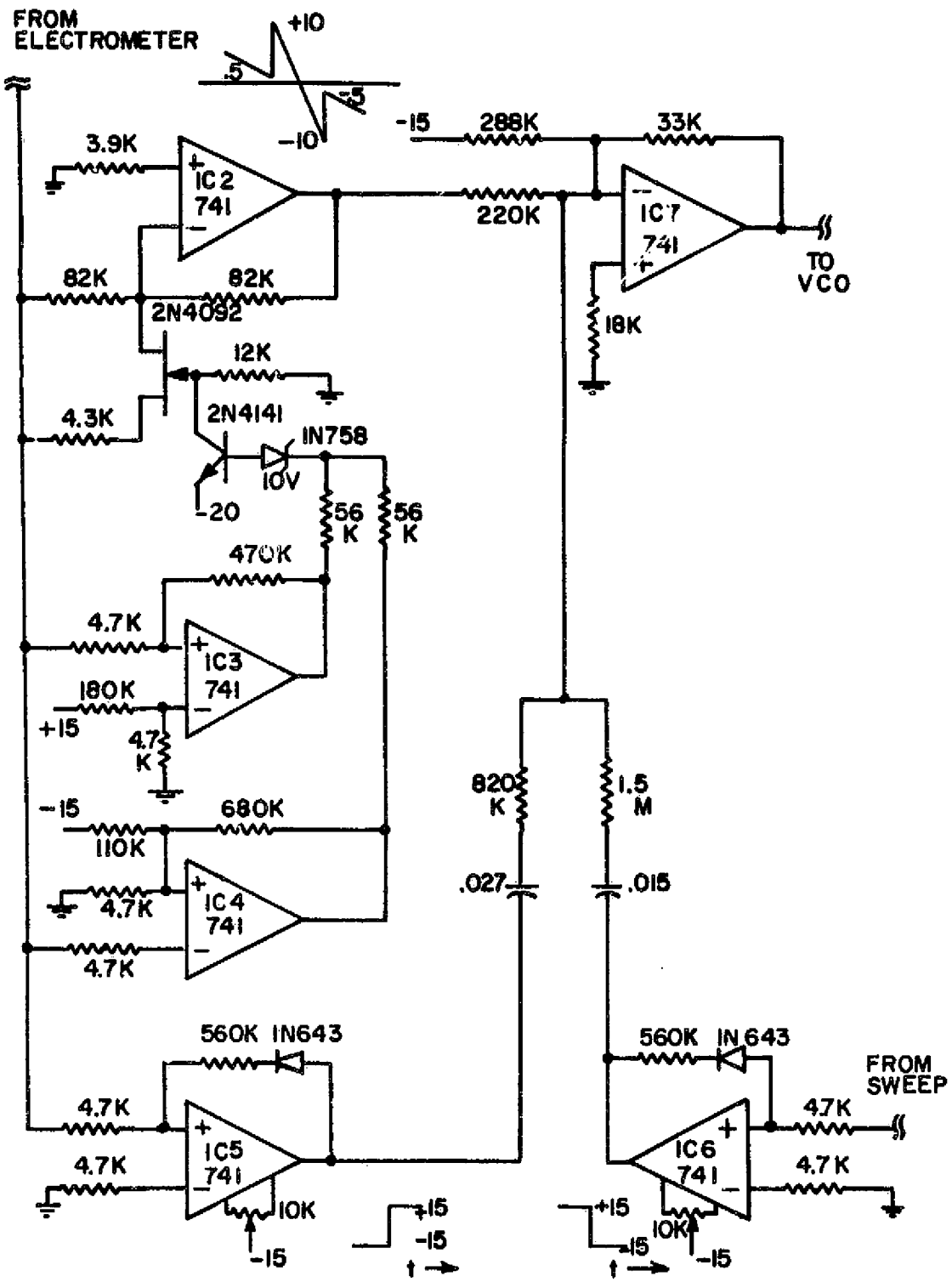

Figure 3.3: Range Switcher and Zero Crossing Detectors

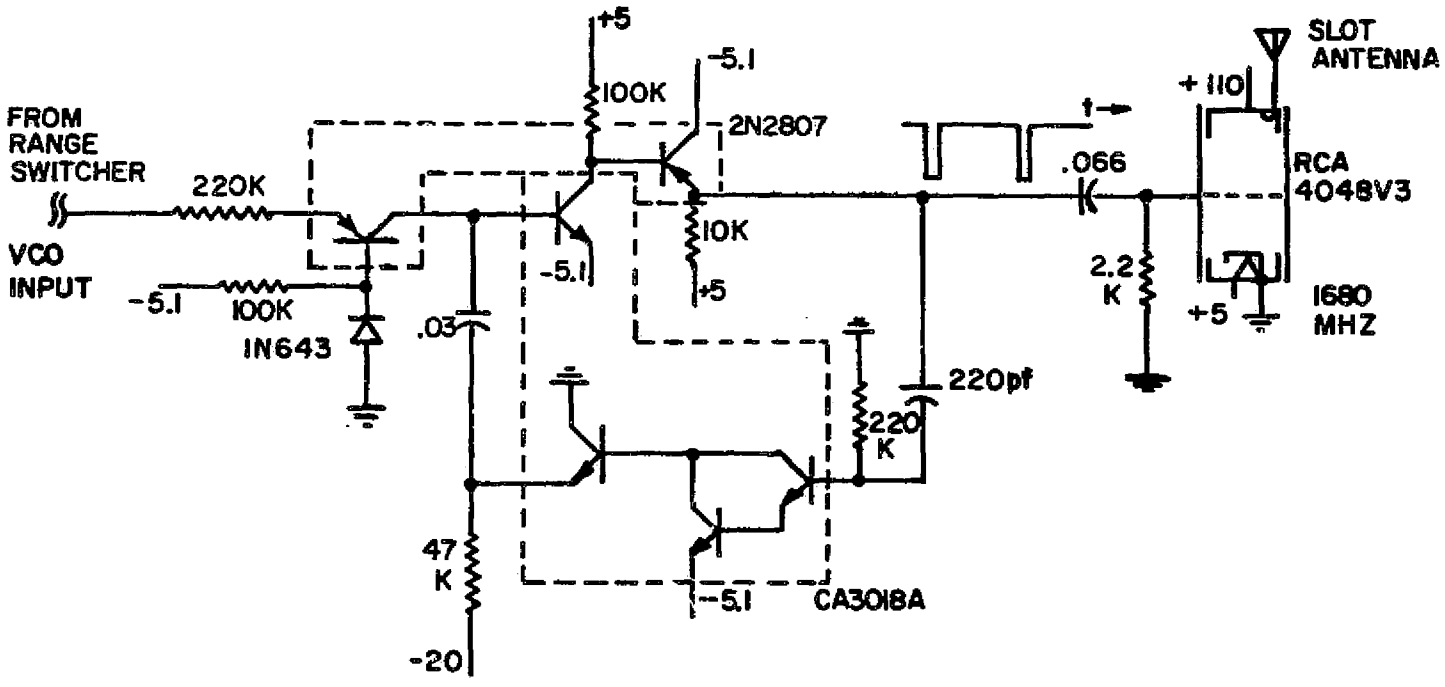

Figure 3.4: VCO and 1680 MHz Transmitter

to the slot antenna feedpoint via a spring clip. Upon payload deployment, the auxiliary antenna pulled away with the nose cone. The antenna mismatch which occurs on the upleg does not degrade the signal strength below what is needed for telemetry track.

The sweep generator of Figure 3.5 utilizes the existing blunt probe approach, with the addition of scaling to the desired +10 volt value provided by IC8. Transistors Q_1 and Q_2 form a free-running multivibrator which resets the sweep wave form. Transistor Q_3 is a current sink which linearly discharges sweep capacitor C3. IC9 inverts the sweep for the intended dV/dt cancellation. The output of the sweep multivibrator is used to trigger the flipflop, IC10. Transistor Q_4 provides signal conditioning and current gain for the trigger of the flipflop. The function of lamp predriver transistor Q_5 is interrupted by redundant, normally open baroswitches, which close at the 50,000-foot level. This baroswitch control reduces the lamp usage time before launch.

The Lyman α lmap of Figure 3.6a utilizes a modified Artech ion chamber which is driven by a 175 MHz source. The internal gas pressure is either 300 μT of Krypton of 1 Torr of hydrogen (hydrogen was used in these payloads). A magnesium fluoride window transmits the UV to the environment. Such a lamp has high spectral purity (Gee, 1966). The shelf life of such a lamp is relatively long (Hale, 1975).

Lamp calibration is performed using an Artech ion chamber filled with NO as shown in Figure 3.6b. The lamp output is then found by

$$n_o = \frac{I_{chamb}}{\eta e A_w} \quad \text{photons cm}^{-2} \text{ sec}^{-1} \qquad 3.8$$

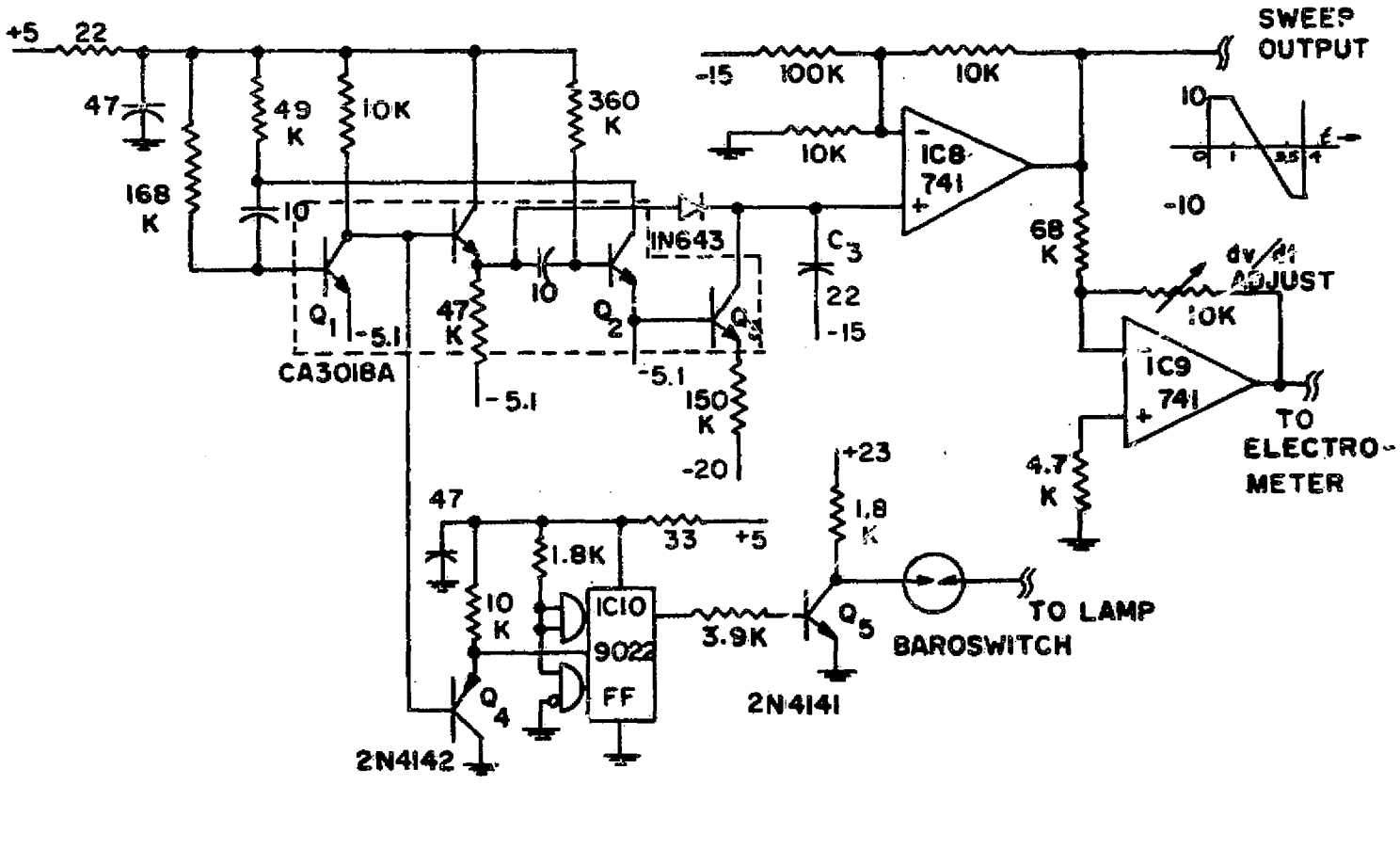

Figure 3.5: Sweep Generator and Lamp Driver

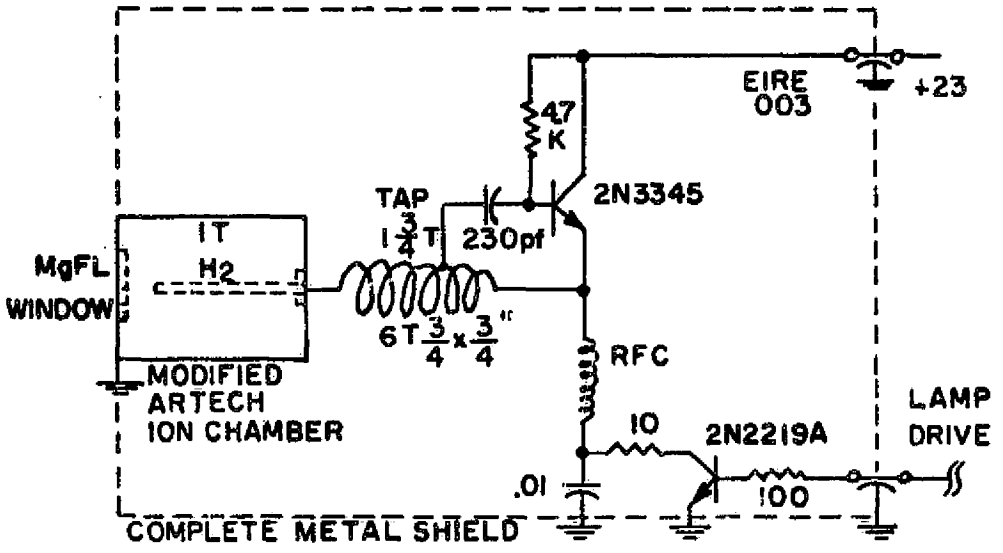

3.6a: Lyman α Source

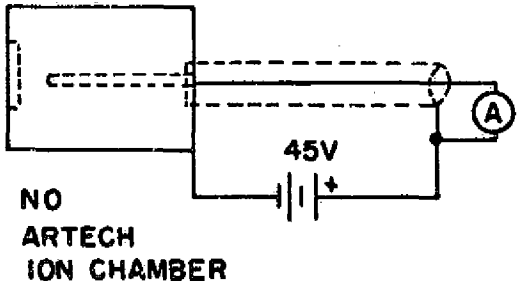

3.6b: Lamp Calibration with NO Chamber

Figure 3.6: UV Lamp and Calibrator

where I_{chamb} is the measured current, η is the conversion efficiency (approximately 50%) and A_w is the window area. The lamp calibrator is held against the lamp for the calibration. A dry hydrogen bath can be used to reduce losses due to absorption by air.

The lamp needs over 20 volts to oscillate vigorously and draws currents in the range of 175 mA. The charge capacity of available nickel cadmium batteries can be more fully used if the power supply inverter also operates from this same supply. The power supply shown in Figure 3.7 supplies the 110 volts at 30 mA needed for the transmitter tube, and the various plus and minus intermediate supplies needed. The inverter is of the "pseudo saturating" type (Buttler, 1972). The inclusion of the saturating inductor, L_1, limits current spiking and thereby reduces the RFI generated as well as increases the efficiency. Coil L_1 is wound on a core identical to the inverter core, with enough turns so that as the inverter core, T_1, starts into saturation, L_1 saturates first. As the emitter current tries to increase, the induced voltage across L_1 reduces the drive to the transistors to a low value. The measured efficiency was 81%, and a reduction of current spiking by a factor of 30 was observed. The negative low voltage supply is developed through damper diodes D3 and D4 rather than an extra inverter winding to also suppress dV/dt spikes at the collectors of the inverter transistors. Zener diodes then develop the other desired low voltage supplies.

Two microswitches are used to interrupt the battery supply. A nylon plunger inserted through a hole in the side of the nosecone depresses these switches, keeping the payload off. Then after the

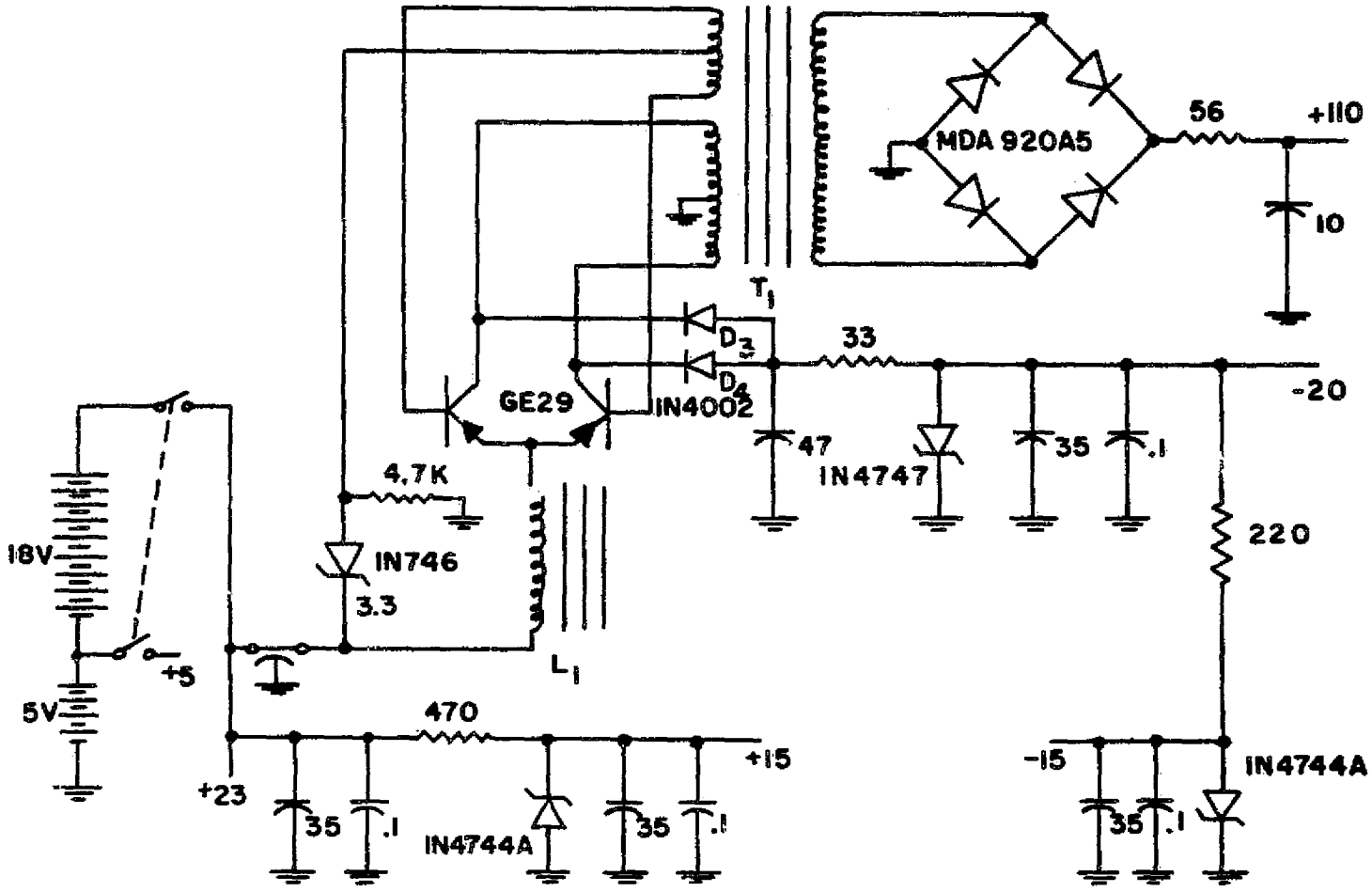

Figure 3.7: Power Supply for Super Arcas Payload

launch tube has raised, just before launch, this pin can be pulled by a nylon rope, activating the payload. Figure 3.8 shows the completed payload.

3.2 Astrobee-D Payload

A more sophisticated payload was developed for the July, 1975, launch. Simultaneous transmission of multiple sensitivities was made possible with the use of a full FM-FM telemetry system. The electrometer of Figure 3.9 and lamp of Figure 3.10 are similar to those of the Super Arcas payload.

An improved sweep generator (Figure 3.11) which was developed for a synoptic Super Loki system blunt probe uses MOSFET, Q_6 with IC11 to form a constant current sink. Another section of IC11 is used as a comparator to turn off the current sink at the end of the desired sweep. This produces a "hard limit" on the negative end of the sweep wave form rather than the soft limit of earlier designs. A third section of IC11 produces the rectangular waveform needed to reset the sweep. The fourth section inverts the sweep for the needed dV/dt correction. IC12 provides a buffered output to drive the outer skin of the payload, the return electrode. IC13 divides the sweep rate by two to produce the lamp flash rate.

The scaling amplifiers of Figure 3.12 provide additional gains of four and twenty. The voltage dividers at the outputs scale the information to the 0 to 5 volt range needed by the VCO's. The shunt capacitances limit the rise times to the values required by IRIG standards. The sweep is also monitored by IC14 upon which are superimposed glitches corresponding to the electrometer zero crossing.

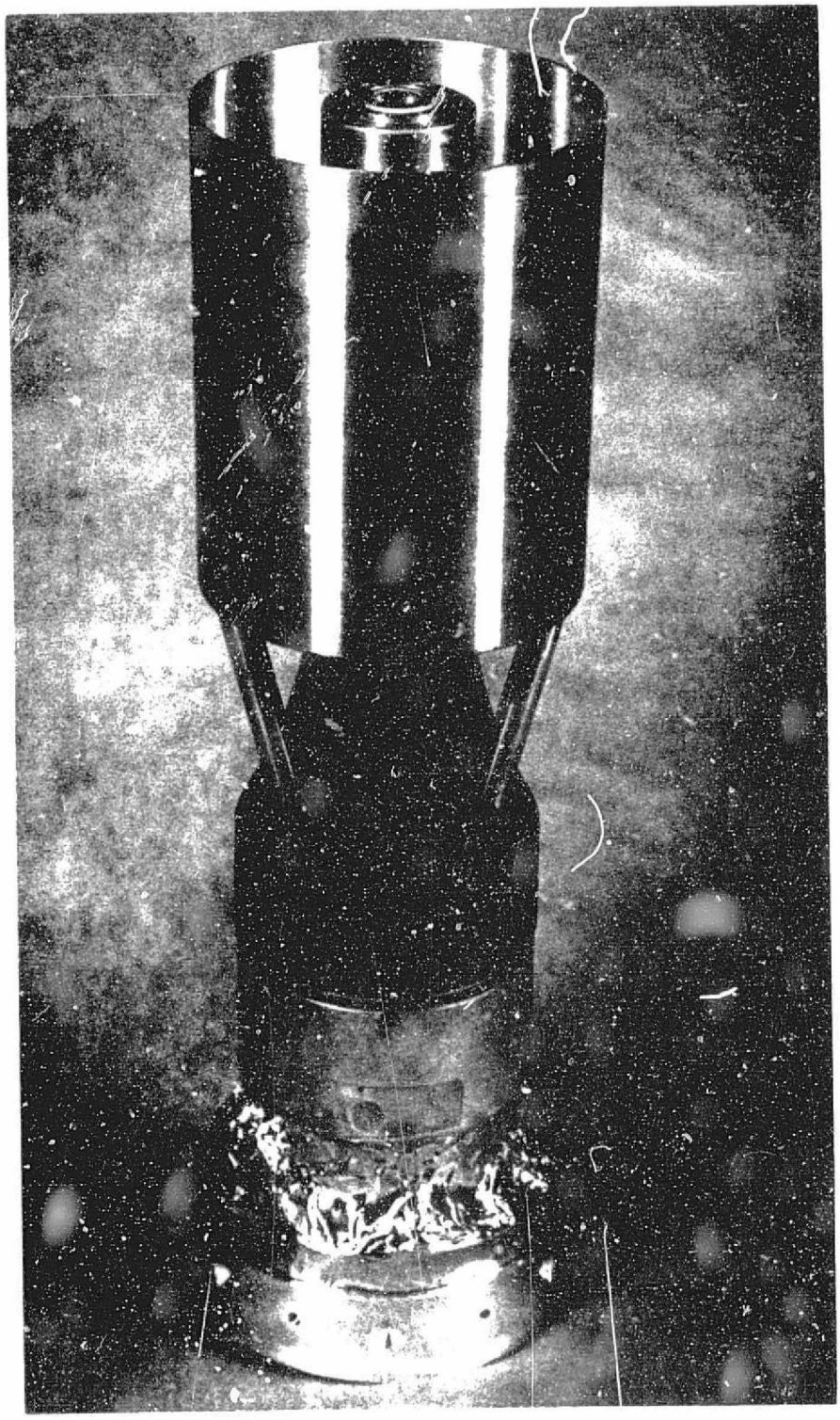

Figure 3.8: Super Arcas Payload

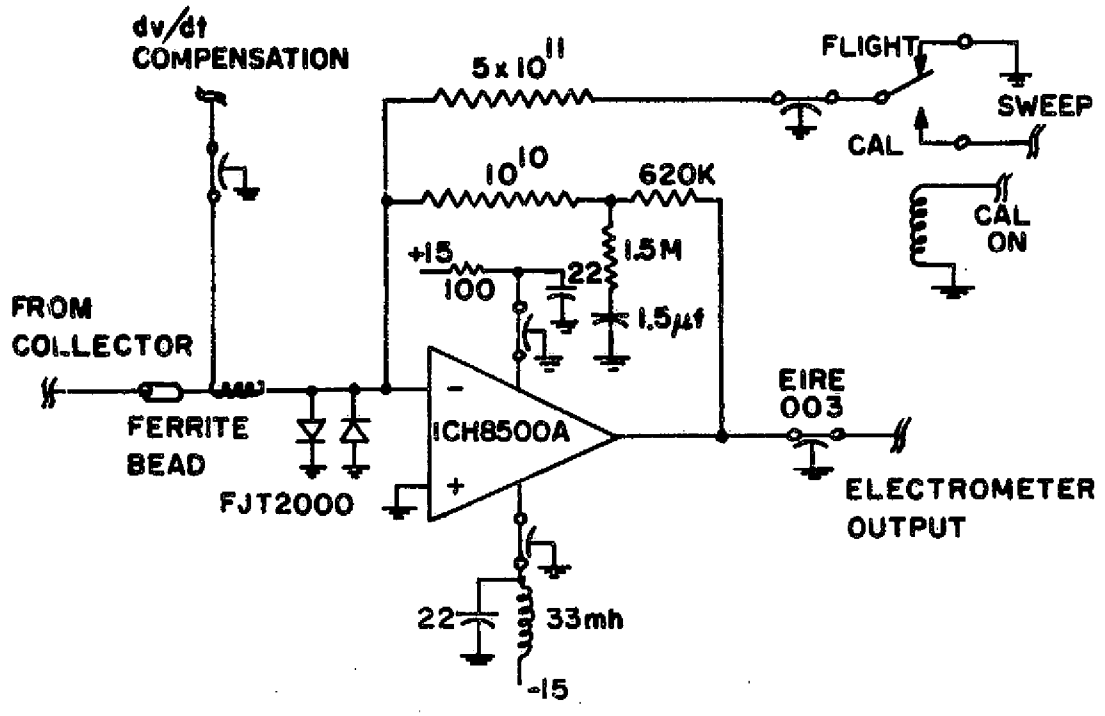

Figure 3.9: Electrometer for Astrobee D Payload

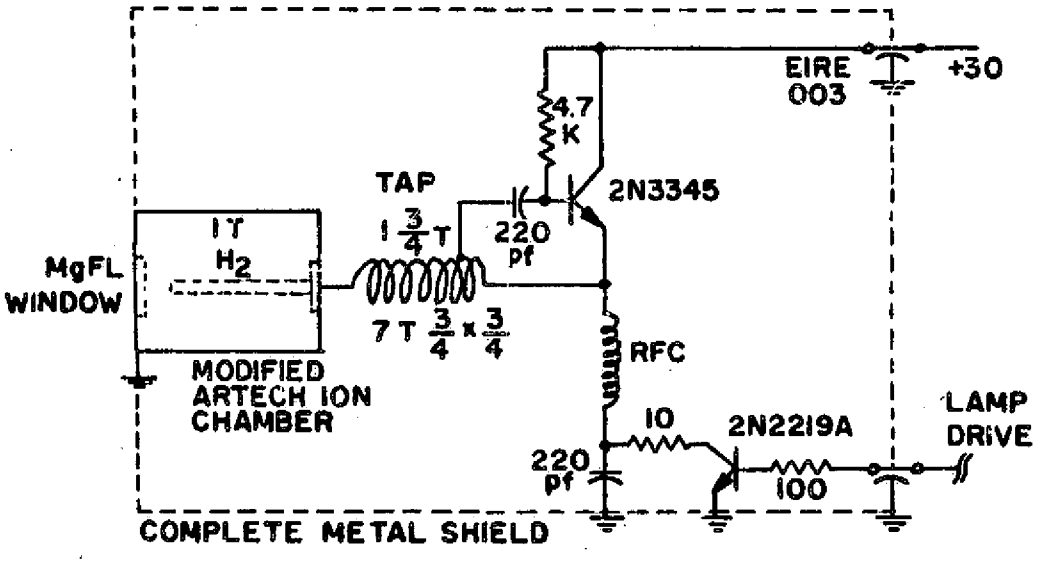

Figure 3.10: Lyman α Lamp for Astrobee D Payload

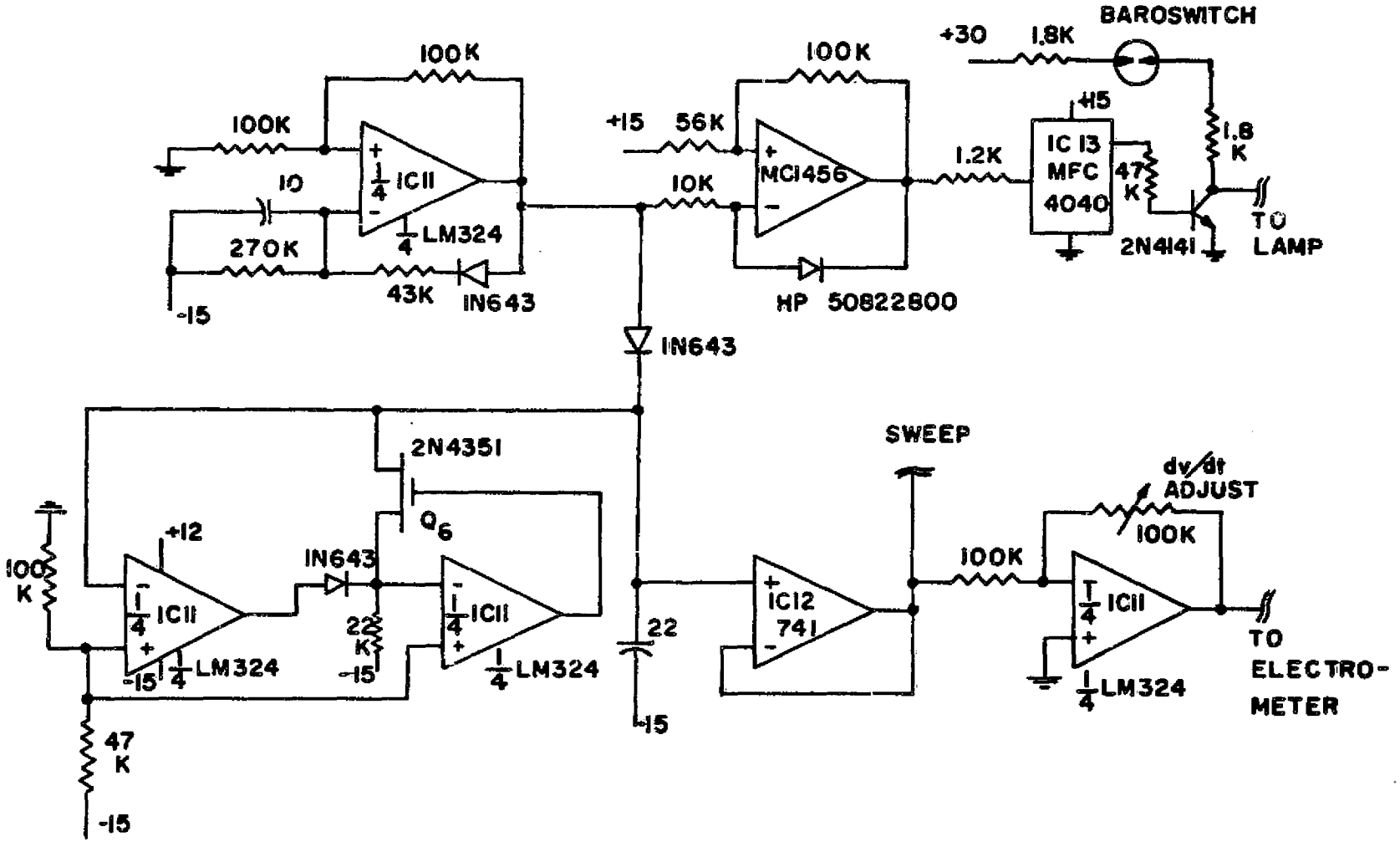

Figure 3.11: Sweep Generator and Lamp Driver

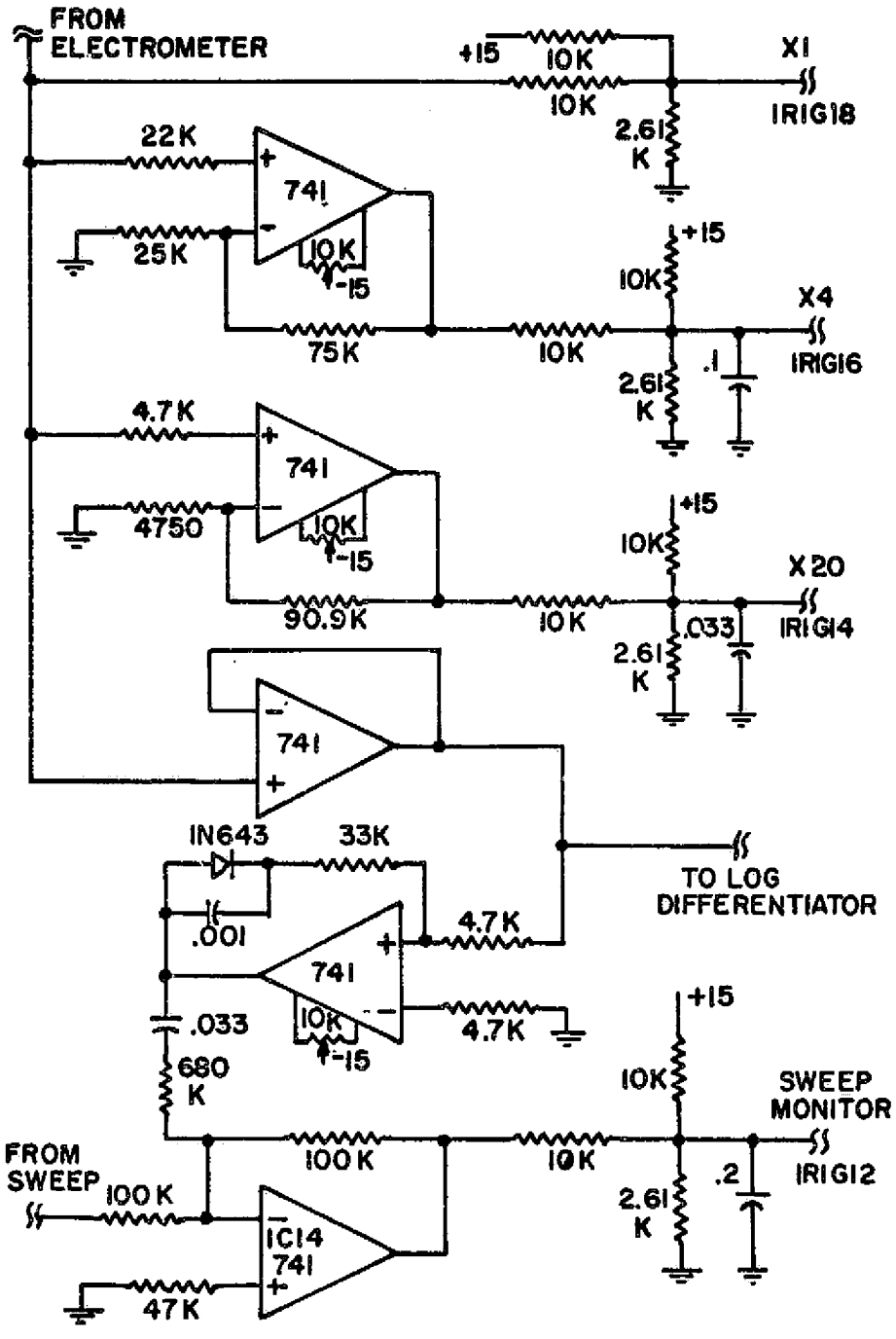

Figure 3.12. Range Amplifiers and Sweep Monitor

Since extra telemetry channels were available, the logarithmic differentiator of Figure 3.13 was included. If the VI characteristics are indeed straight line segments, the differentiator portion will find the slopes, which are then compressed logarithmically before being telemetered to ground. The negative resistance regions of the V-I characteristics produced by this "double" Gerdien geometry cannot be handled by this circuit, but the opportunity of a test flight was taken since this approach might be useful for blunt probe work.

The differentiation is performed by C_4. Its current is used as the input to a logarithm circuit comprised of IC15 and IC16. Transistor Q_7 (one quarter of IC16) provides the logarithmic function since its collector current is proportional to its base emitter voltage. R_3 limits the gain at high frequencies. The temperature coefficients of the transistor must be carefully cancelled if an accurate logarithm is to be formed. A matched transistor, Q_8, and IC17 operate on a constant reference current. One usually then takes the difference between the logarithms, and the transistor emitter saturation current values cancel, but one is left with a direct temperature term multiplying the result. What is unusual here is the use of additional matched transistors Q_9 and Q_{10} to perform the subtraction. By keeping the signal inputs within the linear range of the differential pair and biasing them with a constant current, I_o, the differential gain becomes proportional to T^{-1}. The transistors are on the same chip so the T's cancel, leaving a temperature independent logarithmic gain coefficient. Oven tests over a 0^o to 70^0 range show a residual .02%/^{o}C gain change for this circuit.

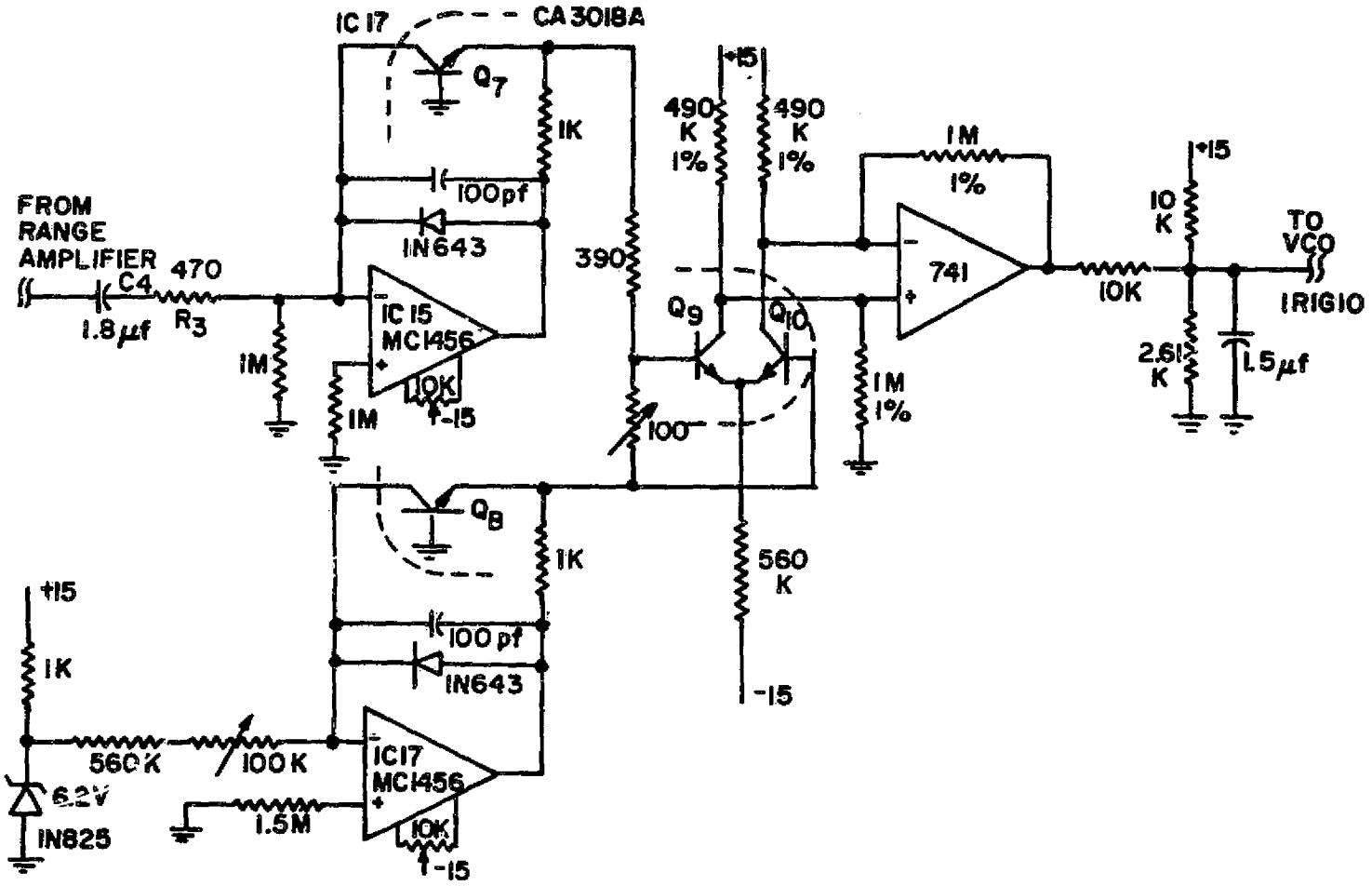

Figure 3.13: Logarithmic Differentiator

Figure 3.14 shows the power supplies used to power this portion of the payload. Damper diodes D5, D6 are used to generate the negative supply.

The silver cell batteries, umbilical control functions, VCO's and S-band transmitter are contained in a telemetry package supplied by NASA, Wallops Island, Va.

The crystal-controlled S-band (2251.5 MHz) transmitter delivers about 2 watts into a 50 ohm load. The development of a suitable antenna is constrained by several factors. Monopoles or dipoles with their sharp points should generally be avoided because of the possibility of corona discharge or point contact rectification when placed in a plasma. Wrap-around printed circuit antennas are a possibility, but they would have to go around the telemetry section, which is covered by part of the metal nose cone extension. The slot antenna used for the blunt probe at 1680 MHz (Cuffin, 1965) has the advantages of an aerodynamical clean profile, no sharp points, and a relatively null-free pattern as the payload rotates on the parachute. The 1-1/2-inch diameter of the center post in this payload is the proper diameter for an S-band slot antenna.

The antenna structure shown in Figure 3.15 was developed by starting from the relative dimensions of the 1680 MHz antenna. The $\lambda/4$ cavity permits mechanical support for the slot while providing a high impedance at the slot. The length of the slot wrapped around the post can be adjusted with a varying width shorting bar at the back to tune the resonant frequency of the antenna. The antenna impedance was measured with a standing wave meter over a range of frequencies around the desired center frequency. The length of cavity and width

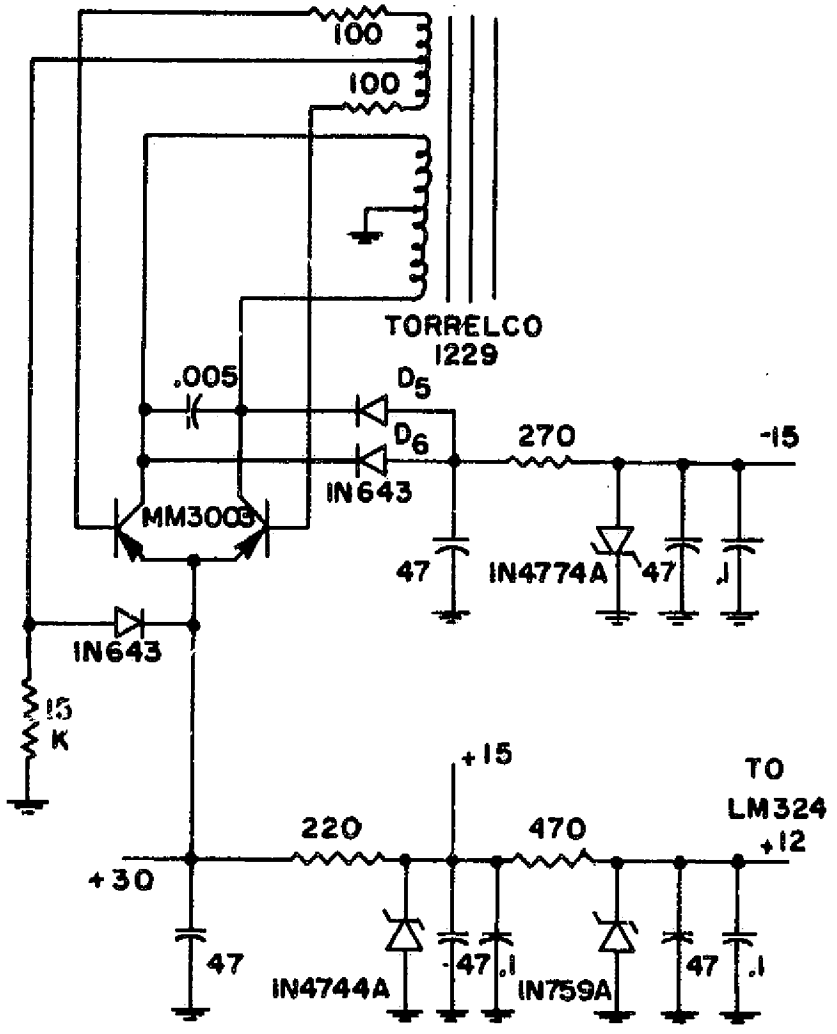

Figure 3.14: Power Supply for Astrobee D Payload

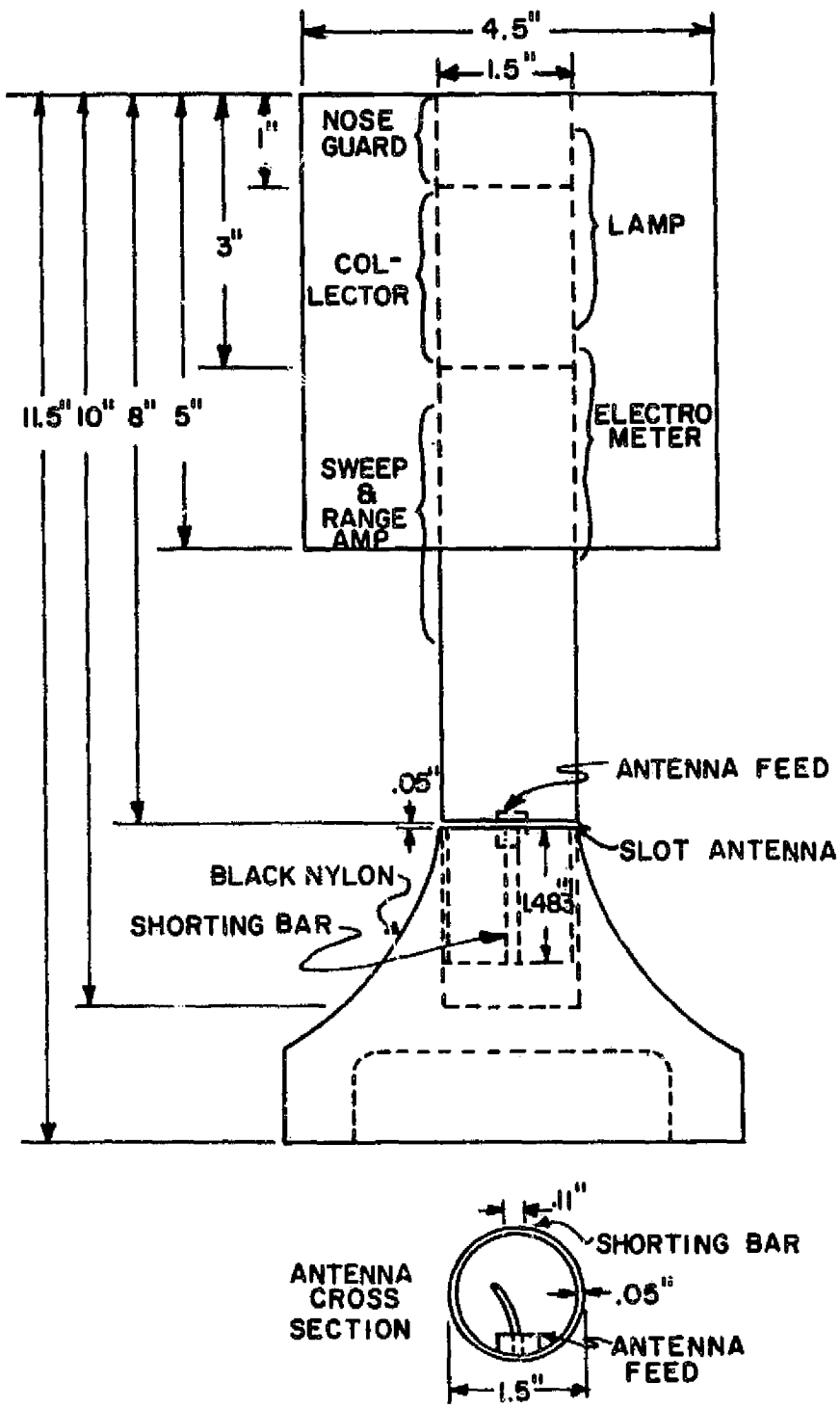

Figure 3.15: Payload and Antenna Structure

of the shorting bar were adjusted independently in an attempt to optimize the antenna impedance, eventually yielding the dimensions shown in the figure. After a while it became apparent that the intrinsic impedance of the antenna was slightly greater than 100 ohms, so a section of 72 ohm cable, an odd number of quarter wavelengths (10-1/4), was used between the antenna and the transmitter. Using the well-known quarter wave transformer expression, one obtains an input impedance of

$$Z_{in} = Z_o^2 / Z_L \qquad 3.9$$

The final observed VSWR is shown in Figure 3.16 which has acceptable bandwidth and VSWR. The two most critical parameters of this design are finding the exact electrical length of the $\lambda/4$ transformer and the design of the antenna feed structure. Several different feed point structures were tried, but at these frequencies any discontinuity produced by threaded sections is major. The best results have been obtained by clamping the shield of the feed cable to the inner wall of the antenna (the center post) and extending the center conductor out to the outer wall where it is soldered to a small tab of adhesive backed copper foil fastened to the outer wall.

The radiation pattern of the antenna was measured with a dummy payload mockup in an anechoic chamber. The effect of the flare from the 1-1/2-inch post to the 5-inch telemetry package was studied. It was found that a metallic flare section brought the main lobe towards the side of the payload. Considering the expected "look angles" at apogee, better performance is expected with the nylon flare section. Pattern tests were conducted for the final payload in a large anechoic

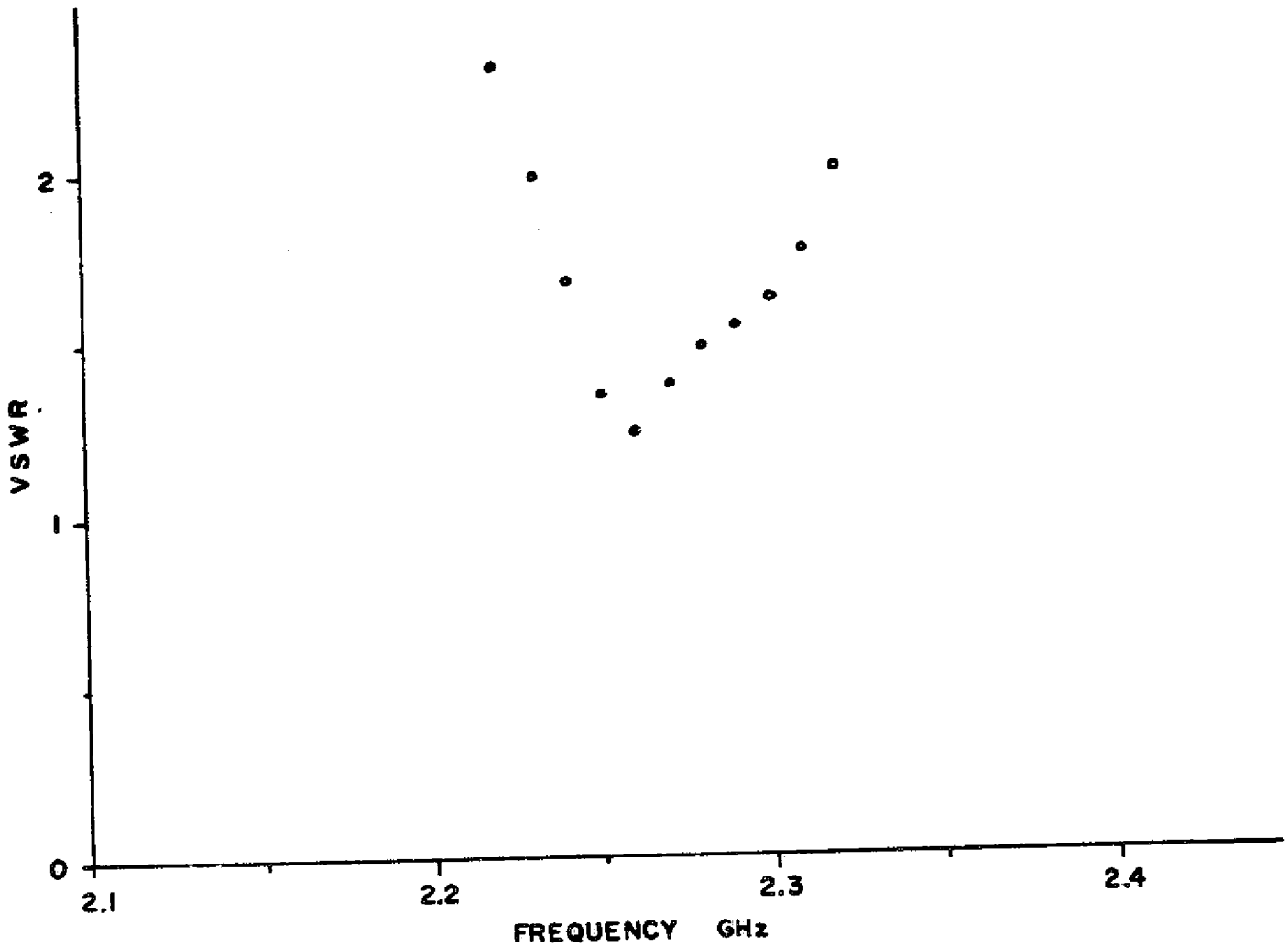

Figure 3.16: S Band Slot Antenna VSWR

chamber at Langley, Va. Figure 3.17 shows a representative "cut" down the length of the payload. As expected, the radiation from a horizontal slot is primarily vertically polarized. The residual horizontal cross polarization arises from small asymmetries in the structure and feed point. As desired, there is a major lobe for look angles in the 20° to 40° range. Figure 3.18 shows the polar plot for a 20° look angle. The shorting bar opposite to the feed point may be expected to produce a null, but as can be seen, the null is not severe at all. Figure 3.19 shows the completed payload.

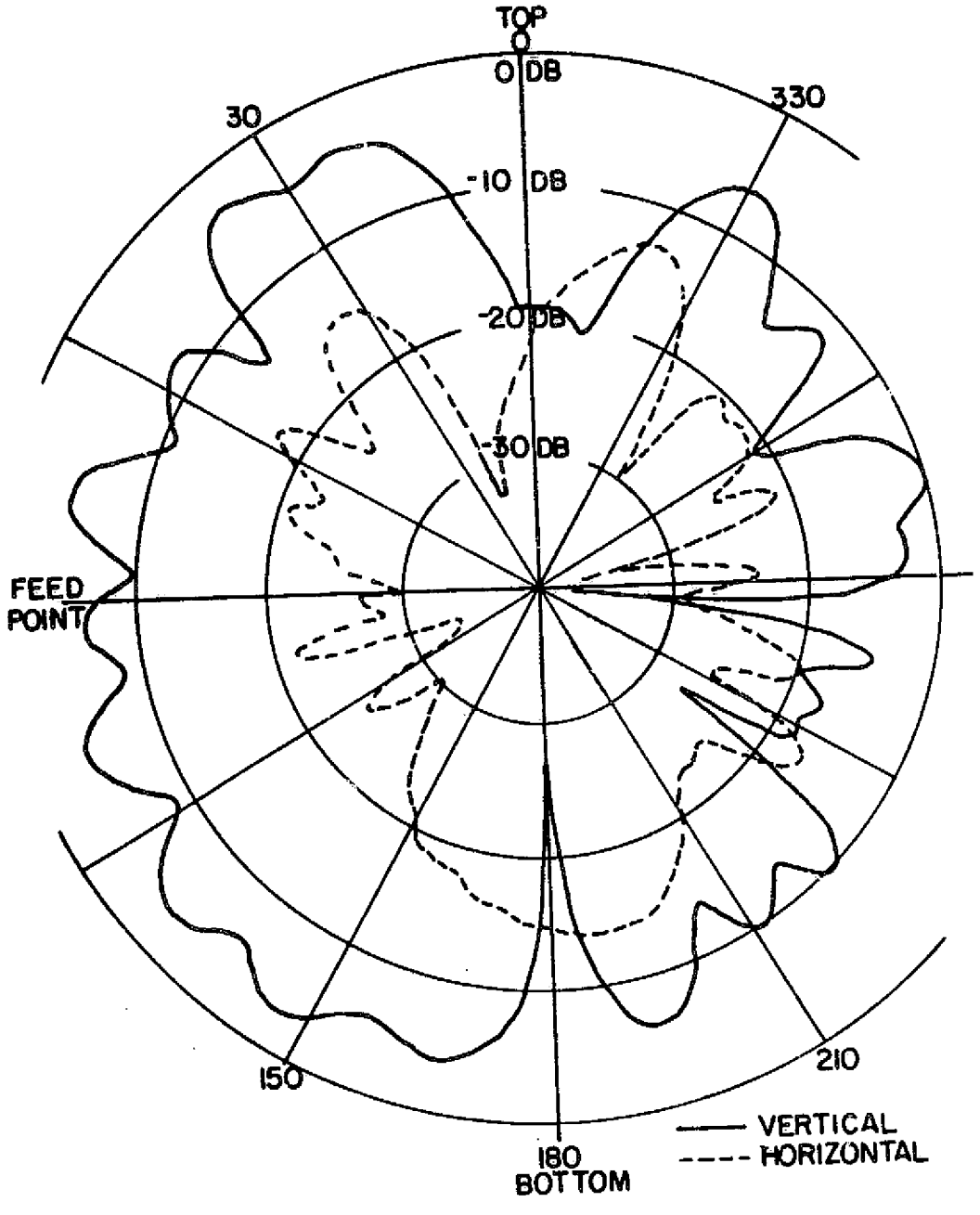

Figure 3.17: Azimuthal Pattern for S Band Antenna, Relative DB Power

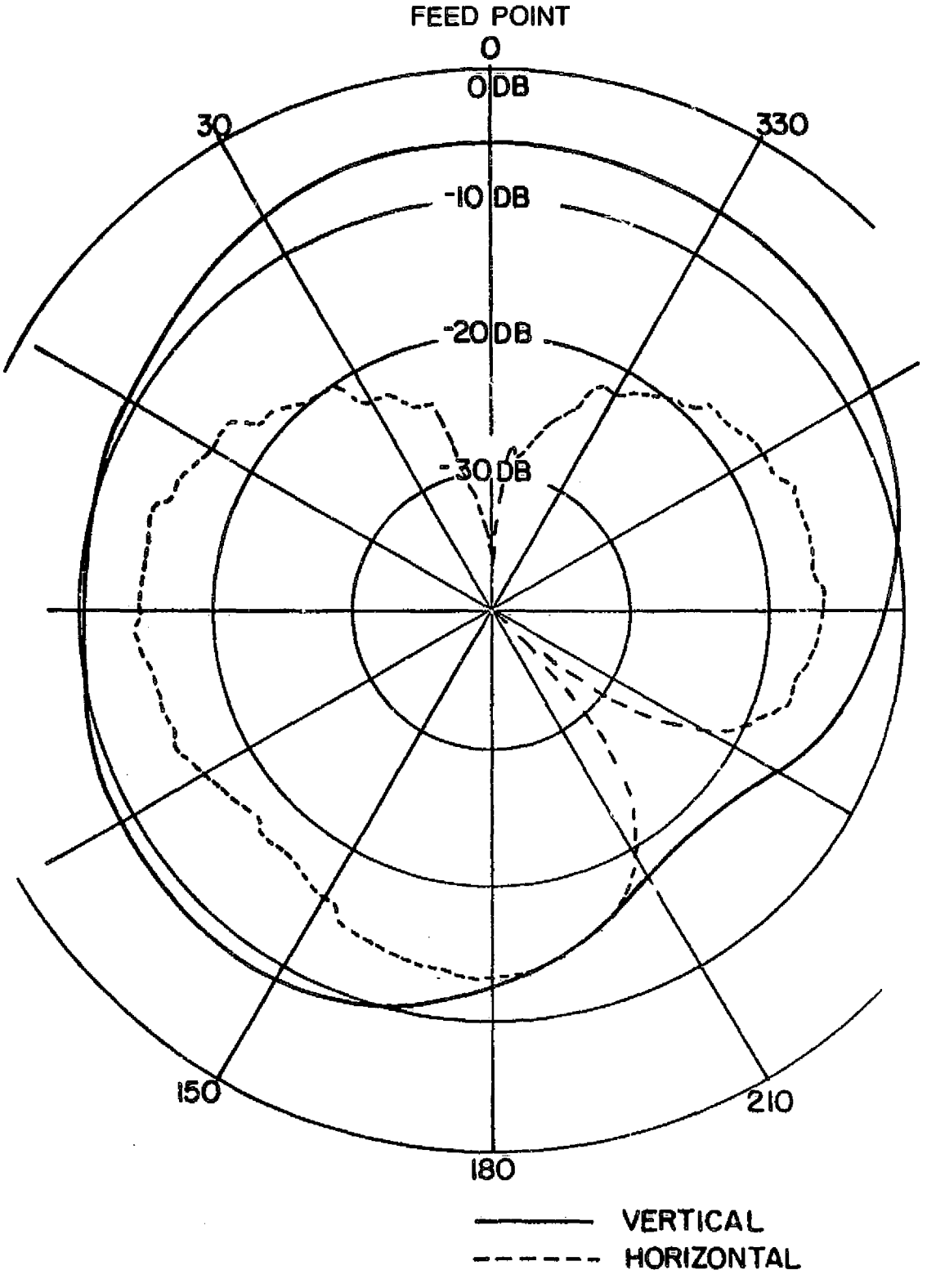

Figure 3.18: Polar Plot for 20° Look Angle, Relative DB Power

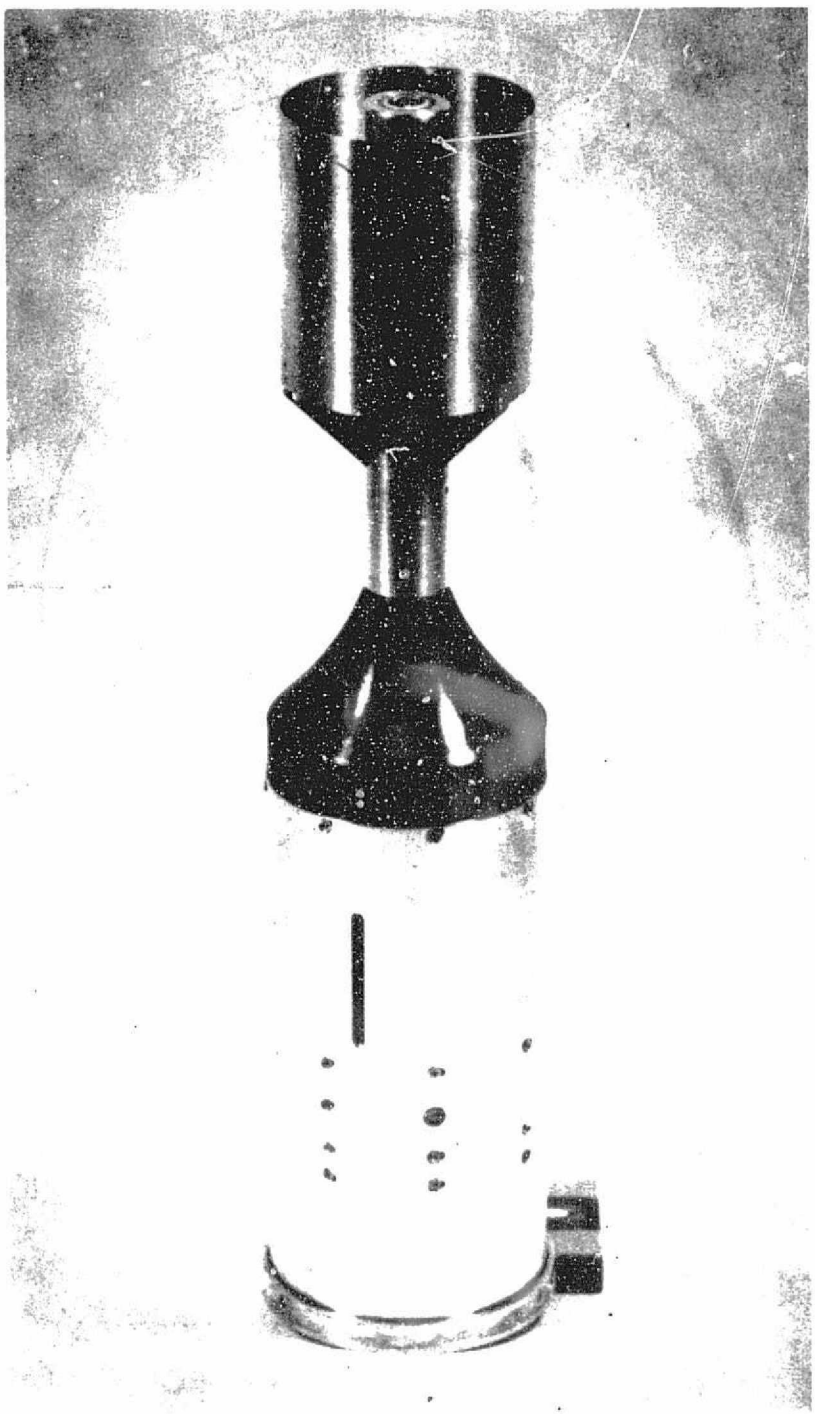

Figure 3.19: Astrobee D Payload

CHAPTER IV

FLIGHT HISTORY AND DATA

4.1 Super Arcas Payload Flight History

The payload described in Section 3.1 was flown on a Super Arcas from Poker Flat, Alaska, on March 10, 1975, one day after an auroral "breakup" condition. Increased radio wave absorption is usually noted after such an energetic breakup. Frequently the increased absorption due to electrons in the D-region will continue into the next day. A riometer which measures received galactic noise at 30 MHz was used as a convenient real time monitor of the absorption. On the day of the launch, this increased absorption lasted well into the late afternoon; the 0224 GMT launch resulted in an 82.6° solar zenith angle.

The altitude versus time as deduced from ground-based radar is shown in Figure 4.1. The corresponding velocity versus altitude plot is shown in Figure 4.2. Telemetry was not obtained until T + 180 seconds, and as can be seen from Figure 4.2, by then the probe had reached its maximum velocity, which was nearly supersonic. As a result the data for the next few kilometers will be biased due to flow complications.

4.2 Super Arcas Payload Data

4.2.1 Payload Calibration

A hydrogen-filled lamp was used for both payloads. Lamp calibration was performed with the circuit of Figure 3.6b. The lamp output sags during each sweep interval (Figure 4.3), but recovers before the next lamp on cycle. The lamp output degrades slowly throughout the flight due to increased transmission losses in the

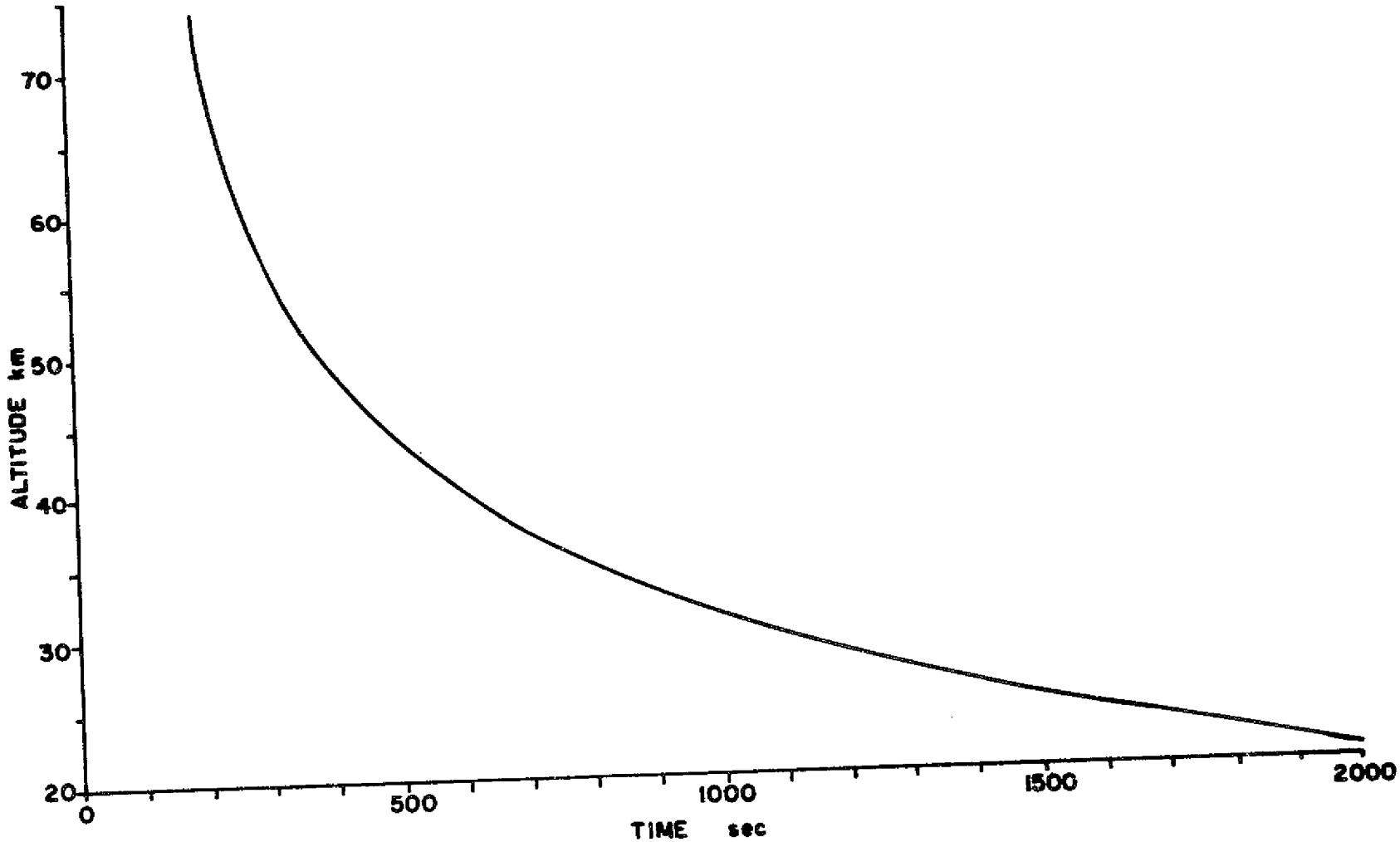

Figure 4.1: Altitude vs. Time for Super Arcas Payload

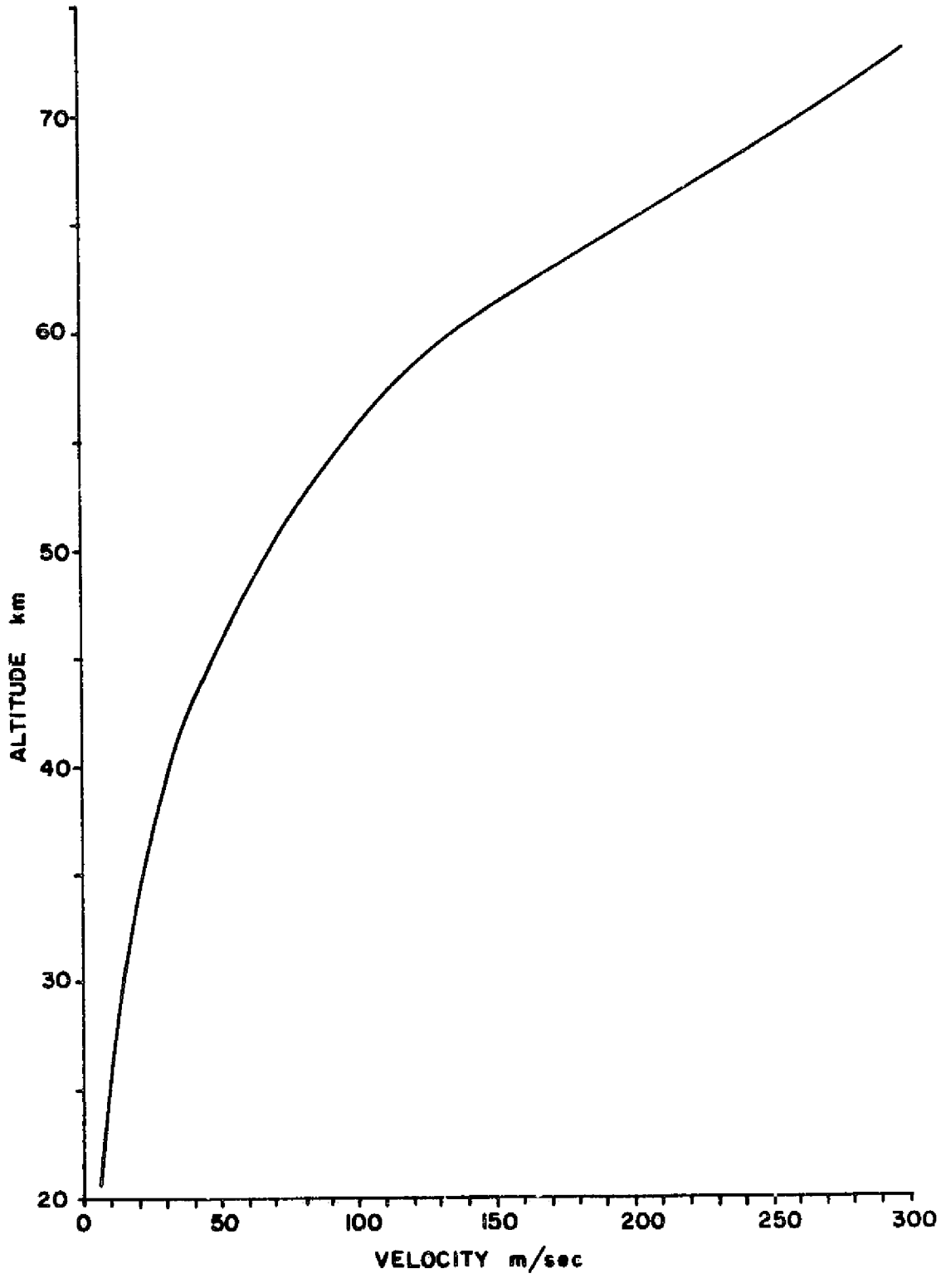

Figure 4.2: Altitude vs. Velocity for Super Arcas Payload

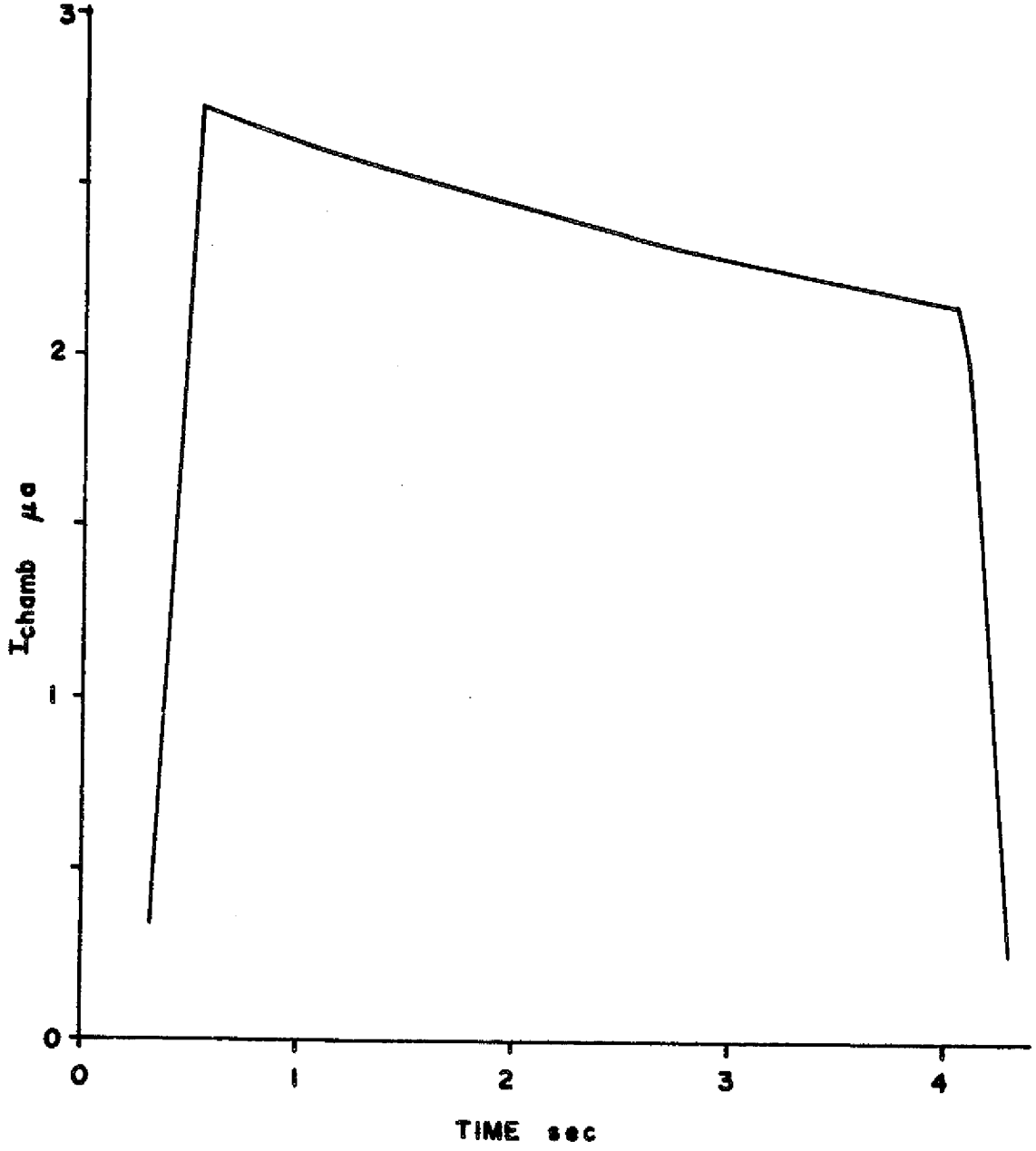

Figure 4.3: UV Lamp Output vs. Time

window with use. When a dry hydrogen bath was used around the lamp and ion chamber, no noticeable change in output was observed. Using Equation 3.8 and a chamber efficiency of 63%, the lamp intensity at the window was $n_o \approx 1.9 \times 10^{13}$ photons cm^{-2} sec^{-1}.

Calibration of the electrometer was performed just before launch by using R_{cal} (Figure 3.2a) as a known resistor and recording the system response. A post-flight playback of the calibration showed a slight curvature, departing from the expected straight line response. Closer inspection of such characteristics as the residual dV/dt current jump revealed that there was probably an incomplete pole zero cancellation in the electrometer. It is not known whether this was due to a component failure or drift. By carefully observing the calibration behavior, an estimate of the pole zero locations was made and a compensating pole zero pair was inserted in the data playback channel. Minor adjustment of the critical frequencies yielded flat calibration curves. The gain changes of the automatic range switcher were compensated for before the pole zero correction by switching the gain of an amplifier in the playback channel.

Unfortunately, the pole zero corrector stretches the sweep zero crossing glitch into the negative ion collection region. Another problem occurs during data dropouts--the pole zero corrector takes a significant portion of the sweep period to recover. Thus some data is lost at low altitudes, where telemetry dropouts are more common.

4.2.2 Observed V-I Characteristics

The range of mobilities observed is smaller than had been expected (Rose and Widdel, 1972). Figure 4.4 shows some represen-

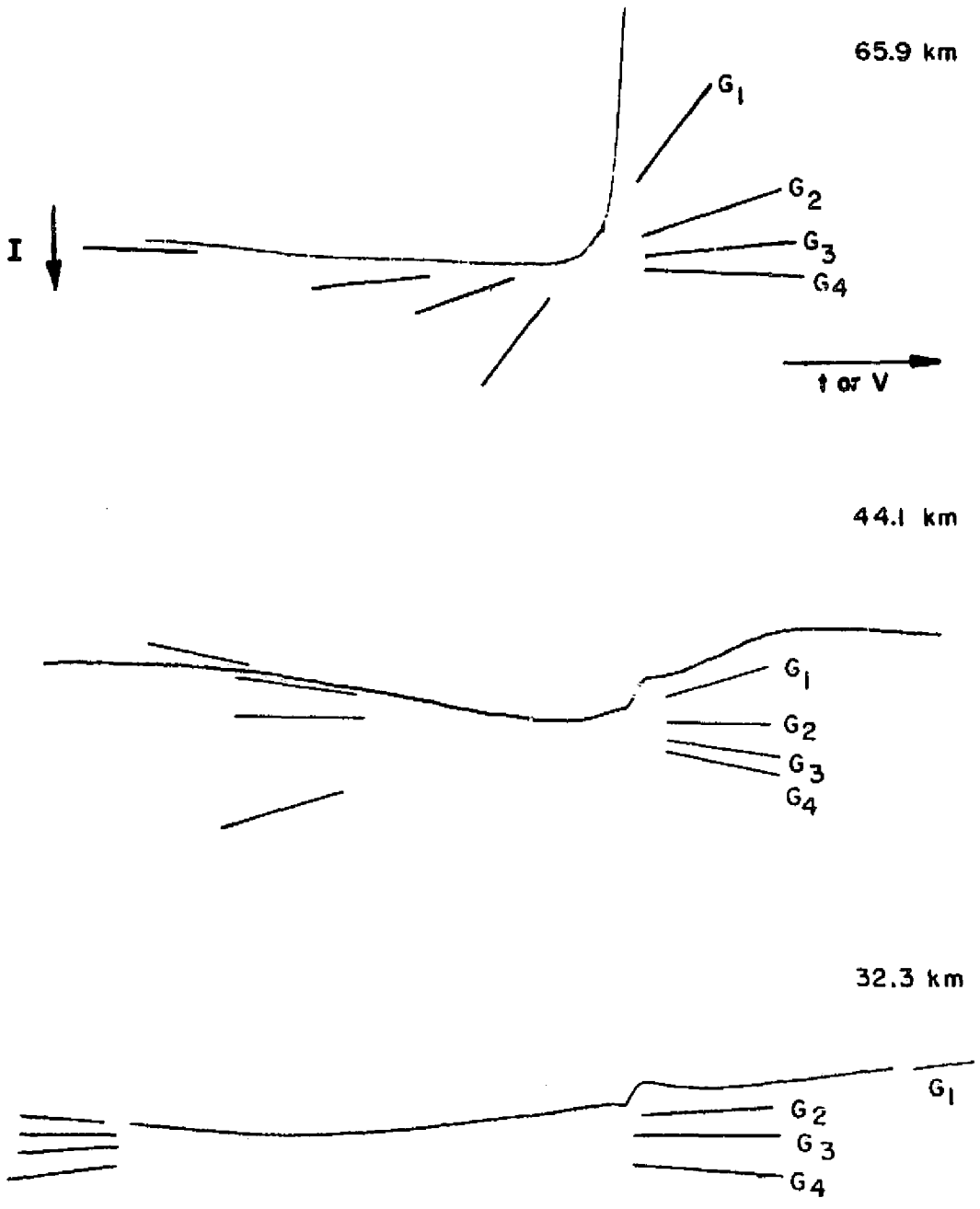

Figure 4.4: Observed V-I Characteristics

tative data traces at various altitudes. The measured conductances are denoted by G_1, G_2, etc. The sweep zero crossing glitch has been smeared as expected. While the changes in conductance are not major, several distinct linear regions can be seen. Care must be taken when determining the conductances to be sure that valid data is obtained. Some traces are not as clean as those of Figure 4.4.

If a pure curve was present in the data, the human eye in fitting a straight line tangent to the curve may in fact be performing a piecewise differentiation. However, data playbacks at different expansion factors yield similar results, which would not be the case for a pure curve.

4.2.3 Lamp-Induced Conductivity Changes

Changes in the largest conductance, G_1, were observed as the lamp was switched on and off for a large altitude range. Since a complete full data sweep is not needed to determine the initial conductance, the dropouts do not create a serious problem. However, the pole zero correction has a long recovery time and telemetry dropouts reduce the available data base. A comparison of the uncompensated data for alternate lamp cycles can be made, however, if one just considers the percent change from the unperturbed conductivity. Figure 4.5 shows the observed uncompensated conductance for the lamp off, Figure 4.6 the conductance for the lamp on. The best fit curves of Figures 4.5 and 4.6 are repeated for comparison in Figure 4.7. As can be seen, the lamp on conductivity is consistently higher, particularly in the 25 to 38 km region. The percent conductivity change of Figure 4.7 has been tabulated in Table 4.1. This conductivity deviation is from a lamp off conductivity presented in Figure 4.8, which was derived

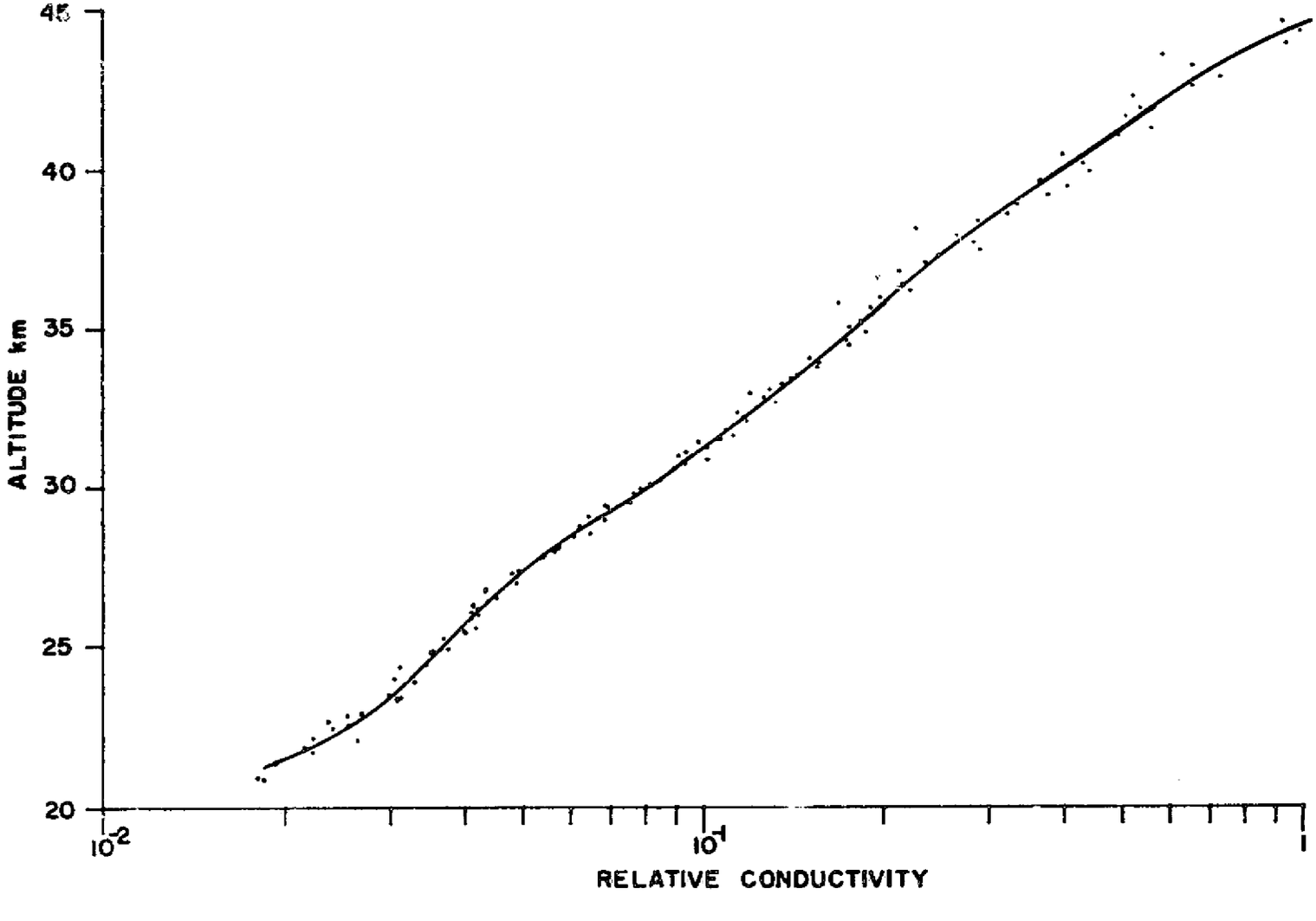

Figure 4.5: Relative Conductivity, Lamp Off

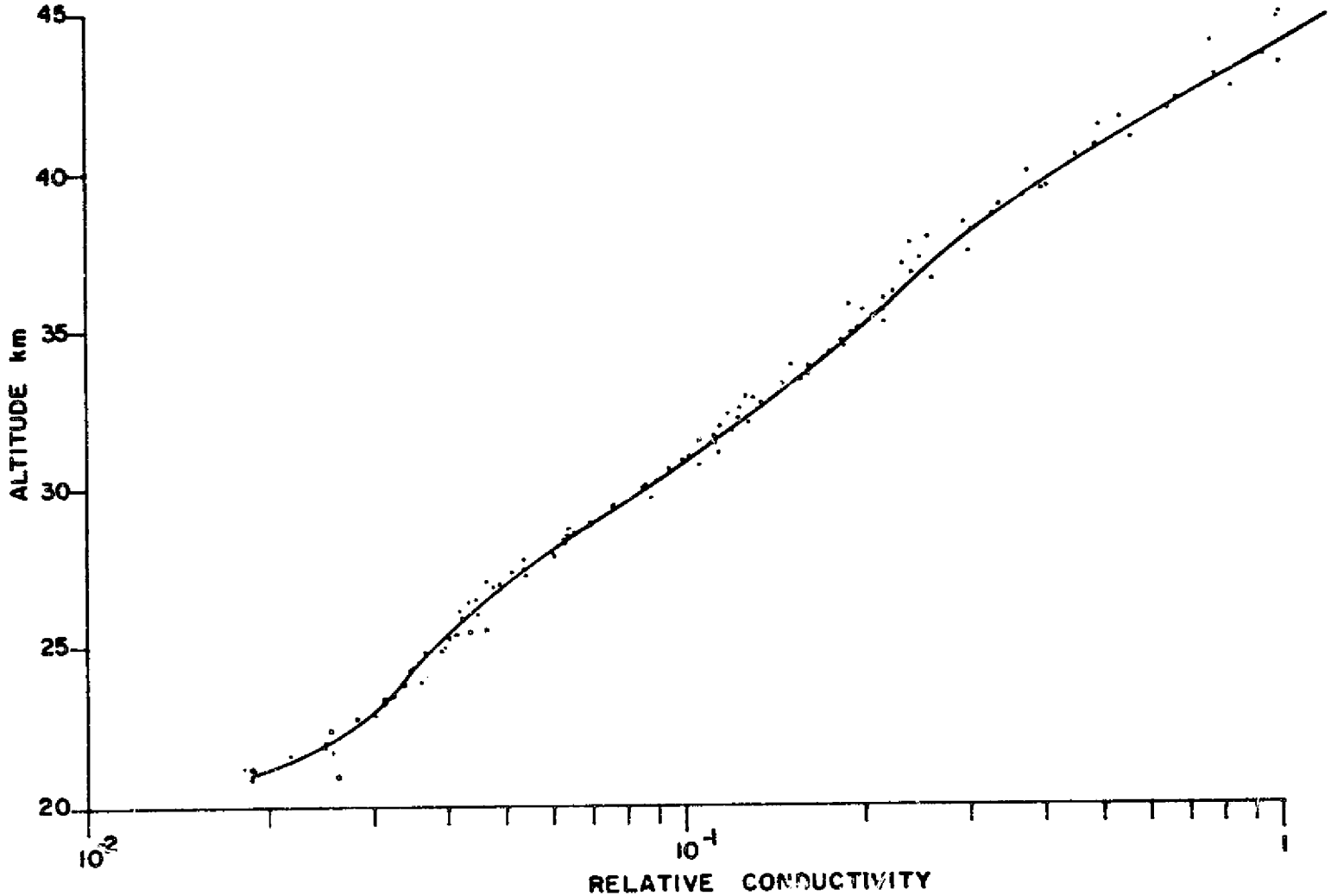

Figure 4.6: Relative Conductivity, Lamp On

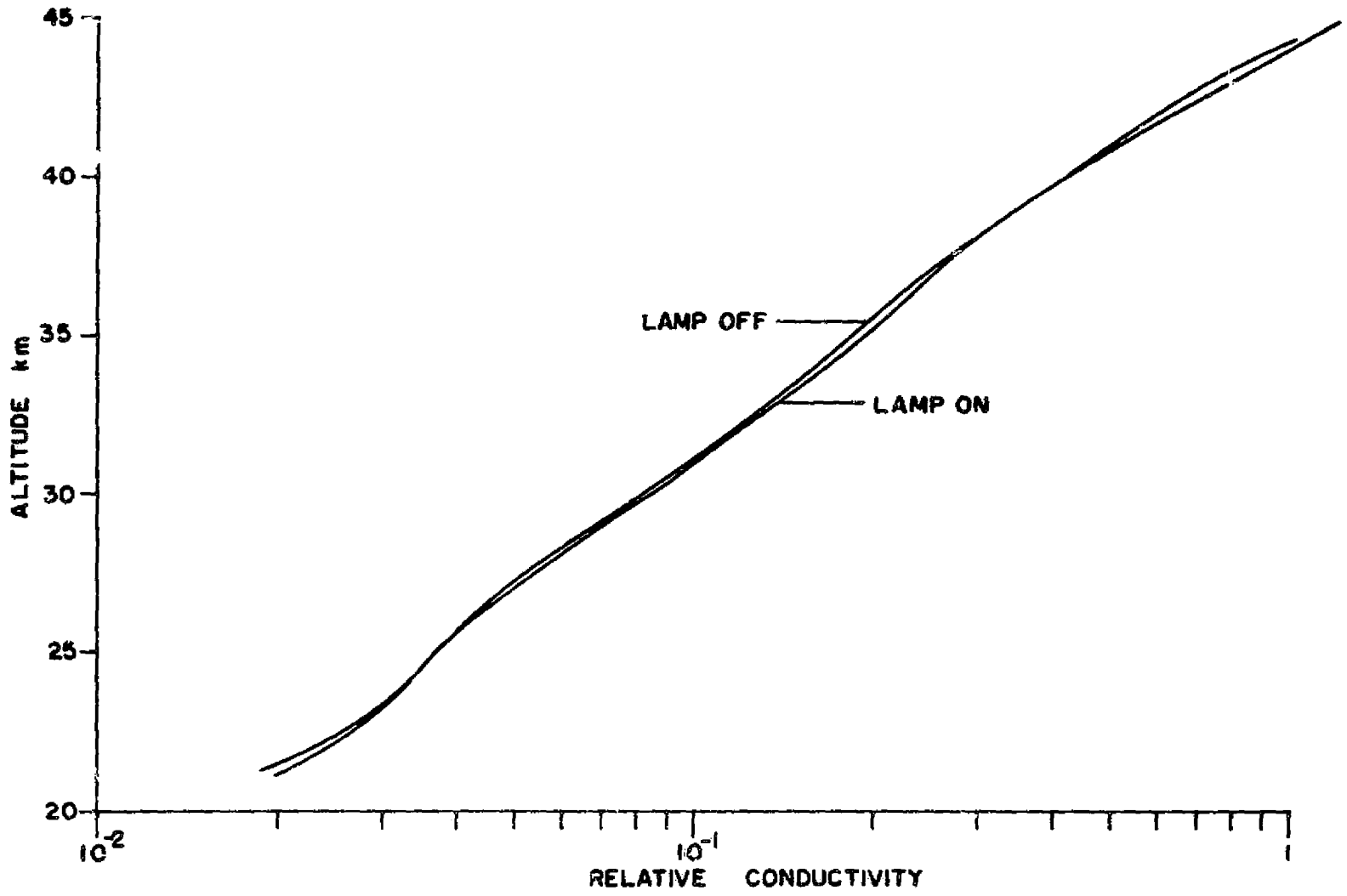

Figure 4.7: Comparison of Lamp On, Lamp Off Conductivities

Table 4.1: Lamp-Induced Percent Change in Conductivity

Altitude km	Percent change conductivity
25.5	0
26.	1.9
26.5	3.1
27.	4.4
27.5	3.7
28.	3.7
28.5	3.1
29.	3.1
29.5	3.7
30.	3.1
30.5	3.1
31.	2.5
31.5	3.7
32.	4.4
32.5	5.0
33.	4.4
33.5	5.0
34.	5.0
34.5	5.0
35.	6.3
35.5	5.7
36.	4.4
36.5	3.1
37.	3.1
37.5	1.8
38.	0

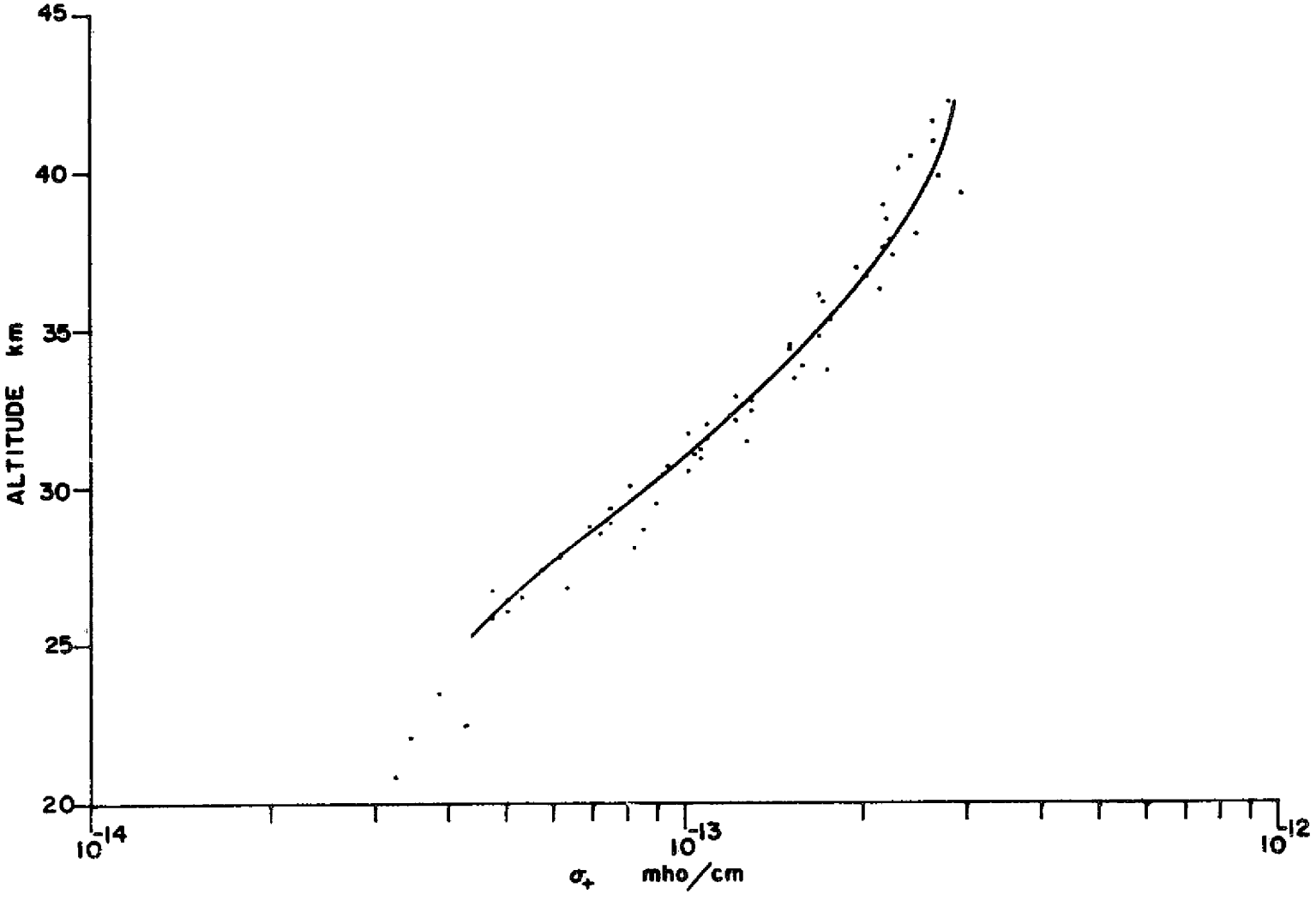

Figure 4.8: Positive Ion Conductivity, Lamp Off

from the compensated data playback. It should be remembered that this conductivity is via Equation 2.4, related to both the ion concentration and mobility.

4.2.4 Observed Mobilities and Concentrations

Figures 4.9 through 4.11 show the mobilities observed when the lamp was off. The most striking feature is the large quantity of fine structure. These mobilities have been found using Equation 2.7 and the observed sweep voltages at which the breakpoints occur. The family groupings indicated have been determined by studying the relative concentrations and assigning questionable points to the most consistent family. The most distinct groups are in the 40 to 55 km region. Below this region the saturation breakpoints are more difficult to determine; above 55 km the altitude sampling rate is low (due to high probe velocity) so that trends are harder to find. Also at the higher altitudes the flow dynamics are more complicated, reducing data accuracy.

As has been discussed in Chapter II, the payload dimensions (collector length) determine the resolution and mobility range of the instrument. There may be additional families of higher or lower mobilities which have not been measured. This is particularly true at the high altitudes where the probe velocity is larger. For the given 10 volt sweep, the heavy group of ions observed by Rose and Widdel (1972) could not be observed by the instrument.

In this altitude region the cosmic ray ionization is thought to lead to various hydrated ions of the form $(H_3O^+) \cdot (H_2O)_n$. For a first approximation, one may expect mobility to be proportional to the square root of the mass of the ion (Farrokh, 1975). Table 4.2

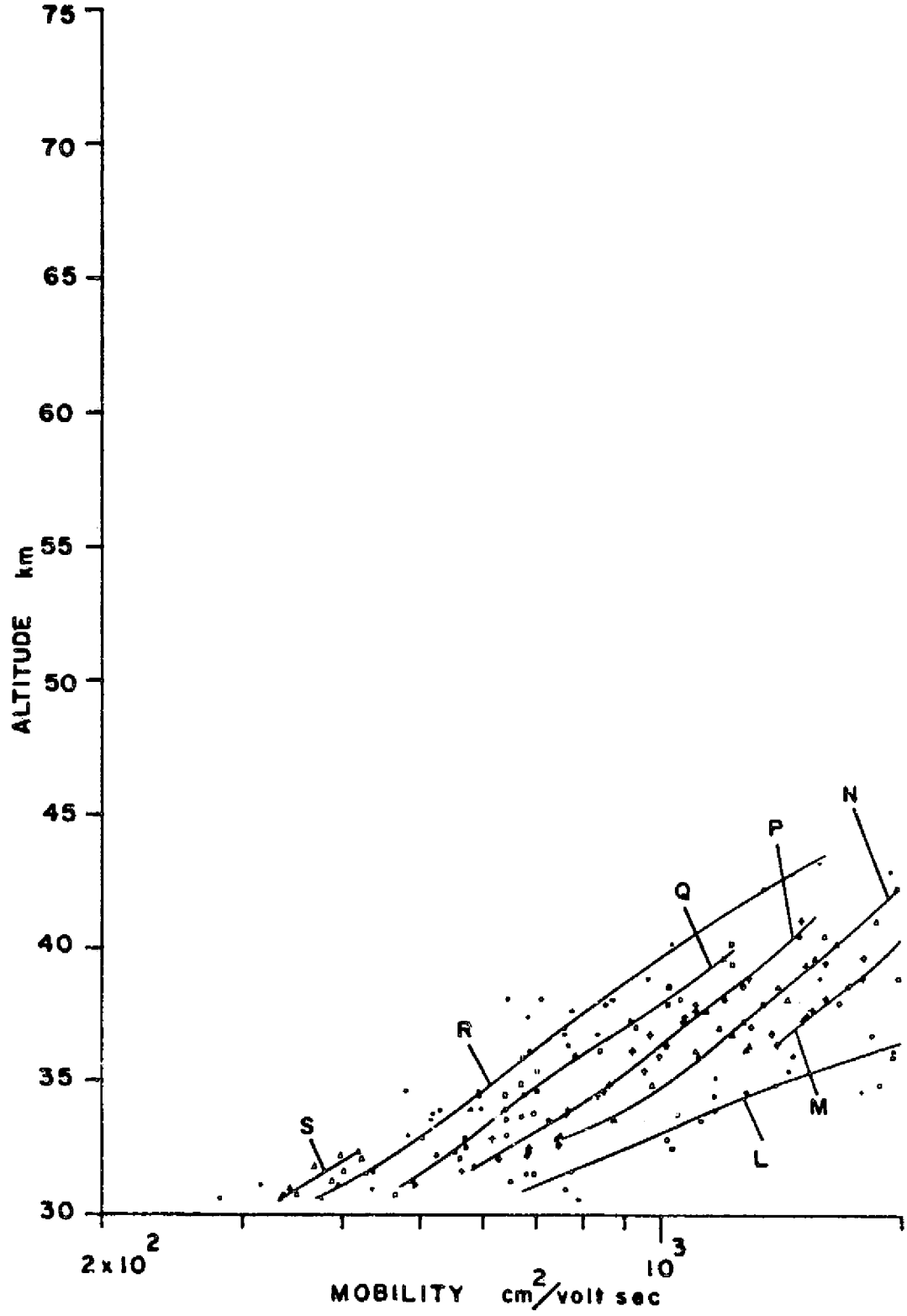

Figure 4.9: Observed Mobilities. Lamp Off

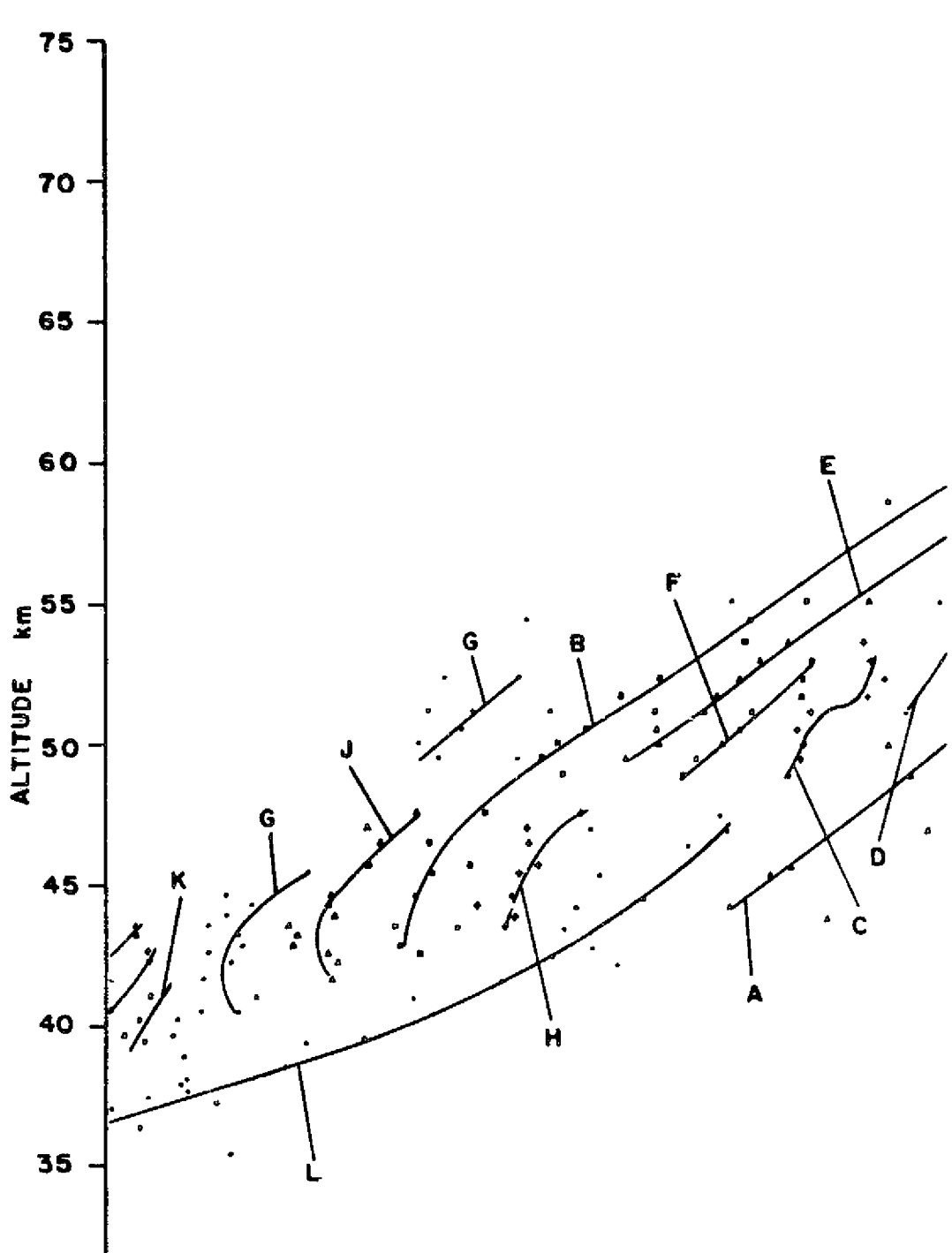

Figure 4.10: Observed Mobilities, Lamp Off

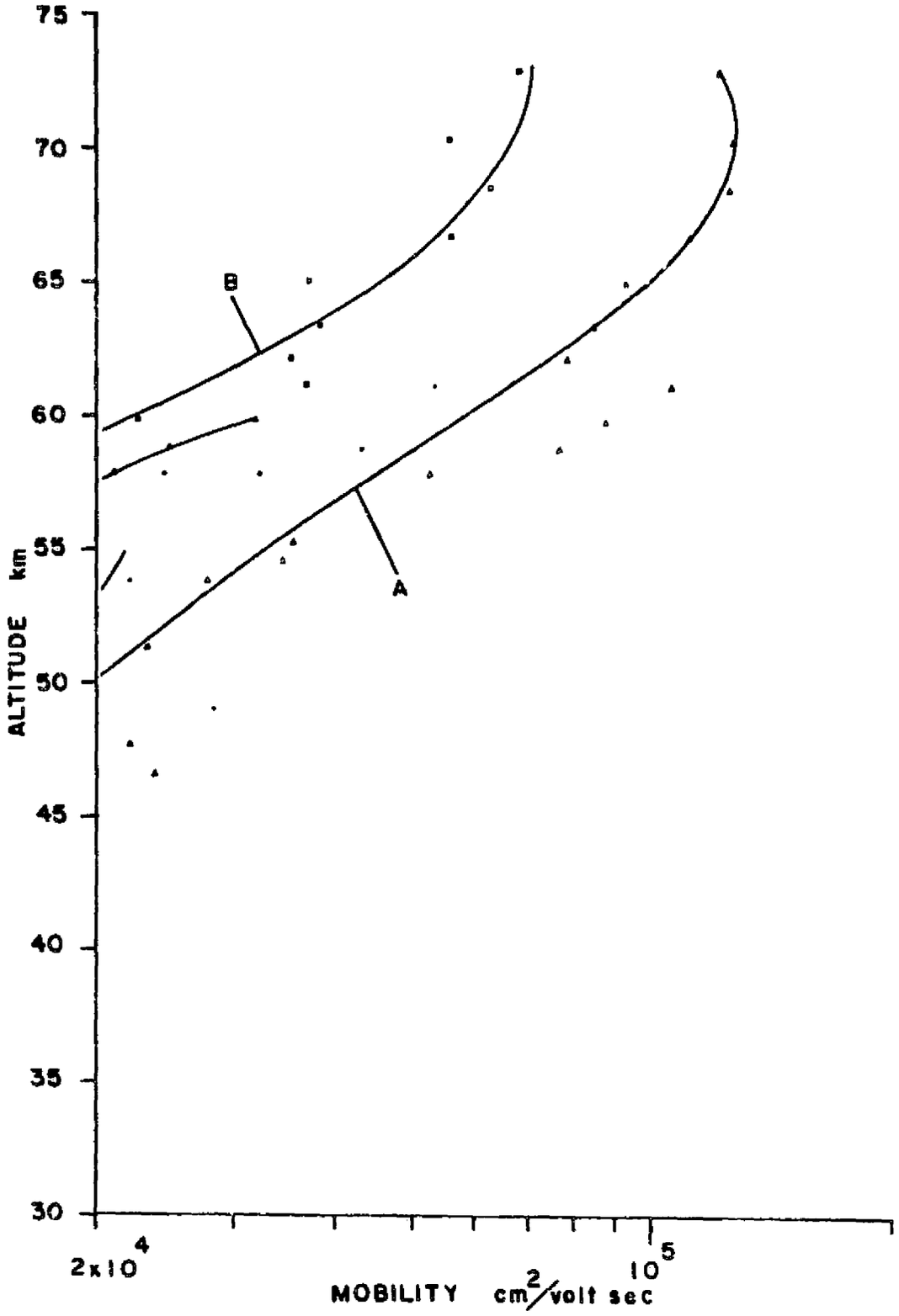

Figure 4.11: Observed Mobilities. Lamp Off

Table 4.2: Hydrated Ion Weights and Mobilities

Ion	AMU	Ratio of Mobilities
H_3O^+	19	
		1.4
$H_3O^+ \cdot (H_2O)_1$	37	
		1.22
$H_3O^+ \cdot (H_2O)_2$	55	
		1.15
$H_3O^+ \cdot (H_2O)_3$	73	
		1.12
$H_3O^+ \cdot (H_2O)_4$	91	
		1.09
$H_3O^+ \cdot (H_2O)_5$	109	
		1.08
$H_3O^+ \cdot (H_2O)_6$	127	
		1.07
$H_3O^+ \cdot (H_2O)_7$	145	

lists the atomic weights for the expected range of hydrated ions. Also included in Table 4.2 is the ratio of expected mobilities between each hydrate type. Comparing these mobility ratios to Figure 4.9, the observed mobility families fall in the general range. The data spread for each family is too large, however, to make an immediate distinction as to the particular hydrate ion family.

The mobilities observed when the lamp was on are presented in Figures 4.12 through 4.14. Generally the mobility families are very similar, as expected, except for the lightest, high mobility ion. Ion family LL is of a higher mobility than ion family L. While the expected ionization by the lamp should produce light ions, the unperturbed family L should remain. Instead ion family L seems to disappear, suggesting that ionization of nitric oxide is not taking place. A comparison of the best fit curves to the mobility data is presented in Figure 4.15.

Further information is presented by the relative concentrations of each family type. Figures 4.16 through 4.23 present the observed concentrations for the lamp off. Figures 4.24 through 4.31 present the observed concentrations when the lamp is on. These concentrations have been determined by using the observed conductivities and mobilities and Equation 2.4. In general, there is more scatter in this data than the mobility data. Generally when the concentration of a mobility data point that is far from its family average mobility is recalculated with the average mobility, less scatter of the concentration data results. There are also occasional mobility data points which do not fit any family and must be attributed to noise. In general, the remaining conductivity data from that same sweep

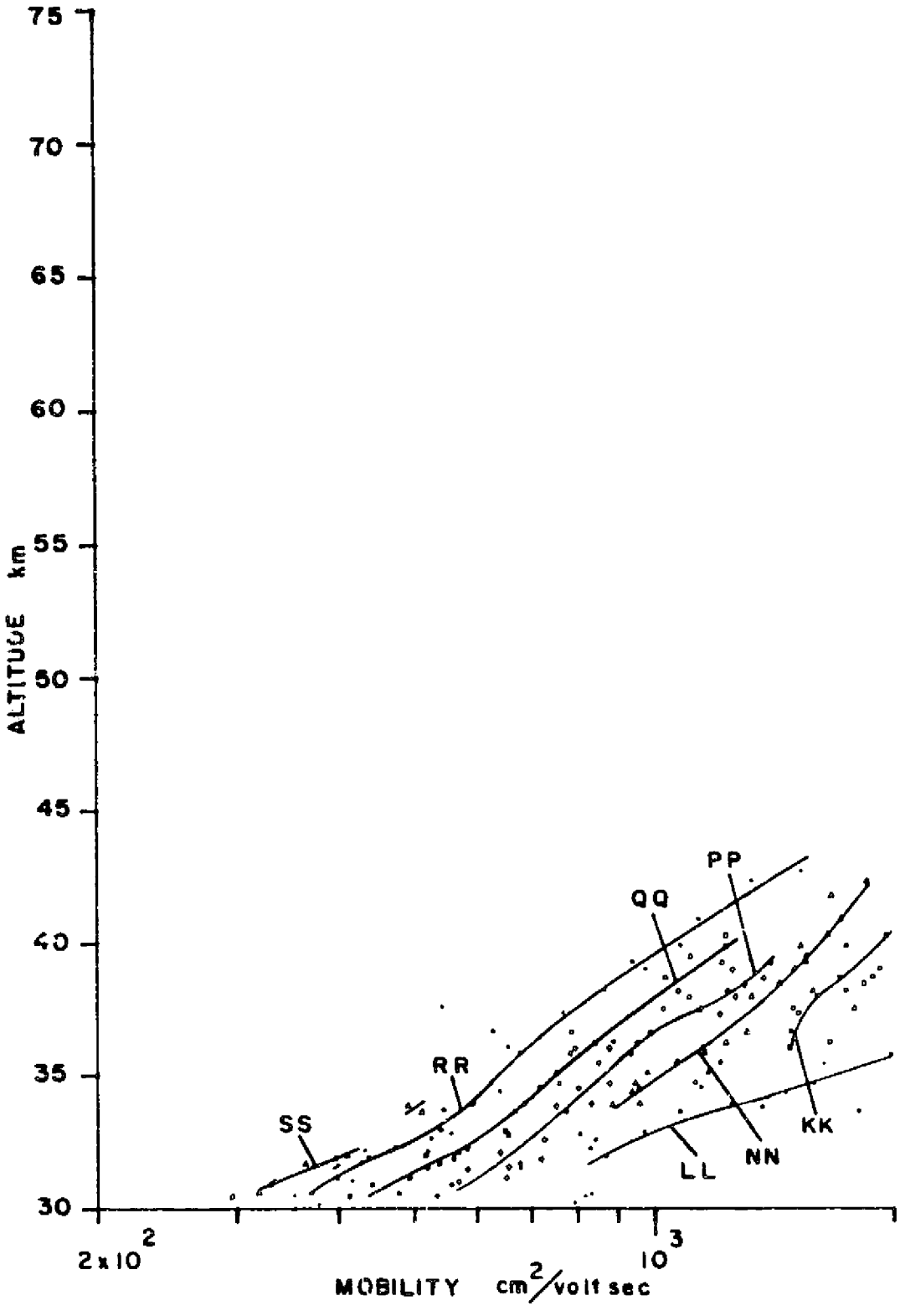

Figure 4.12: Observed Mobilities. Lamp On

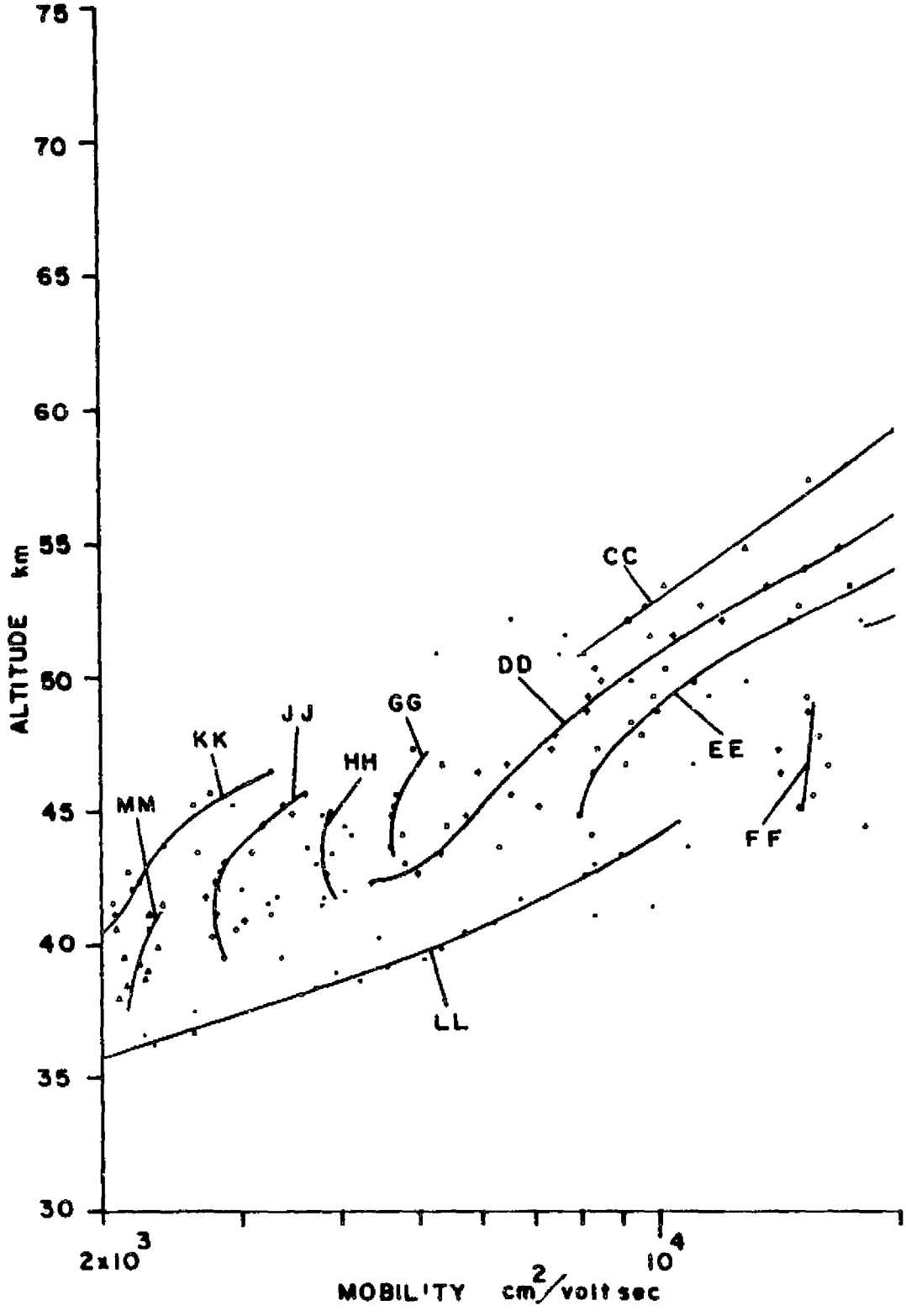

Figure 4.13: Observed Mobilities. Lamp On

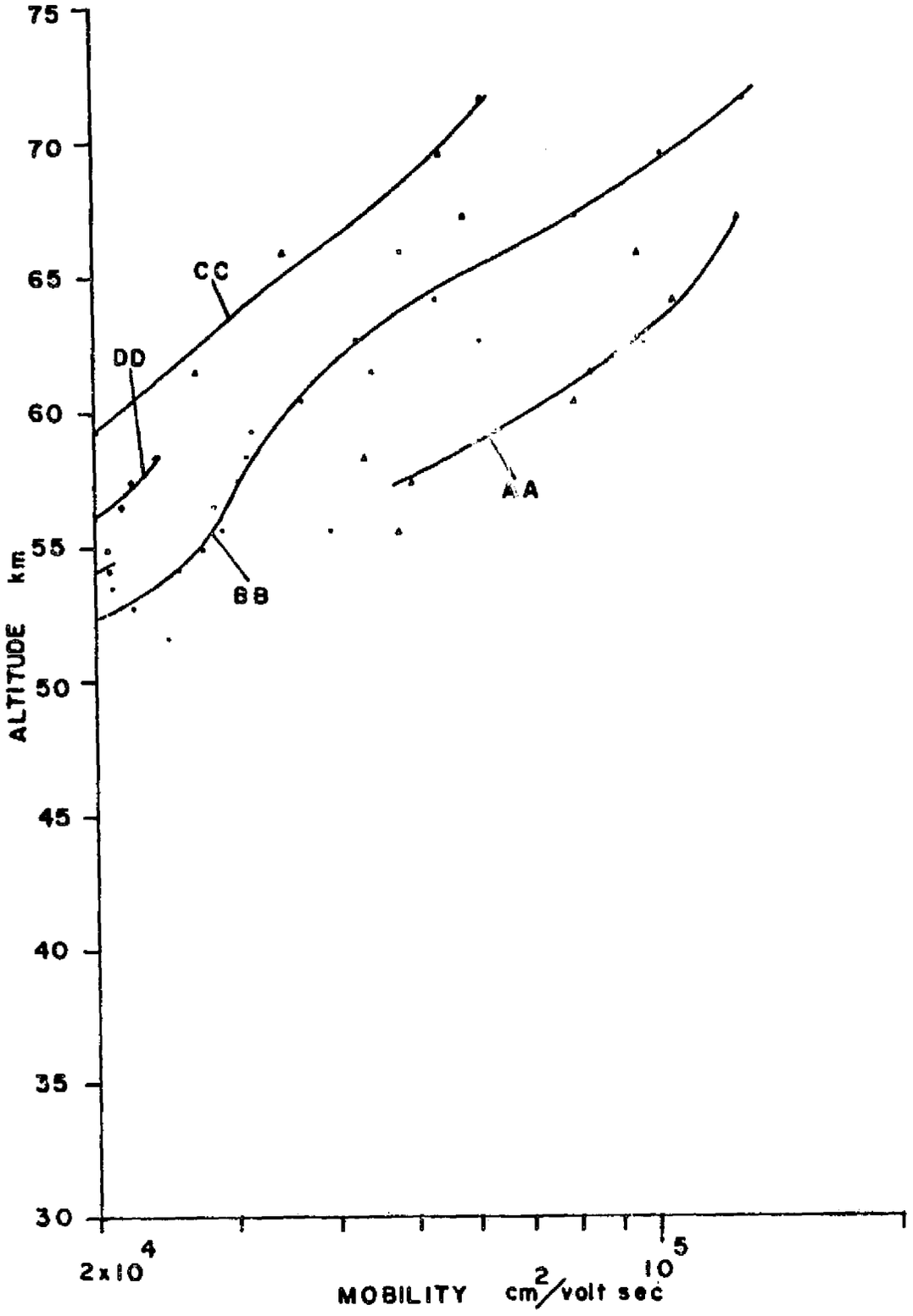

Figure 4.14: Observed Mobilities, Lamp On

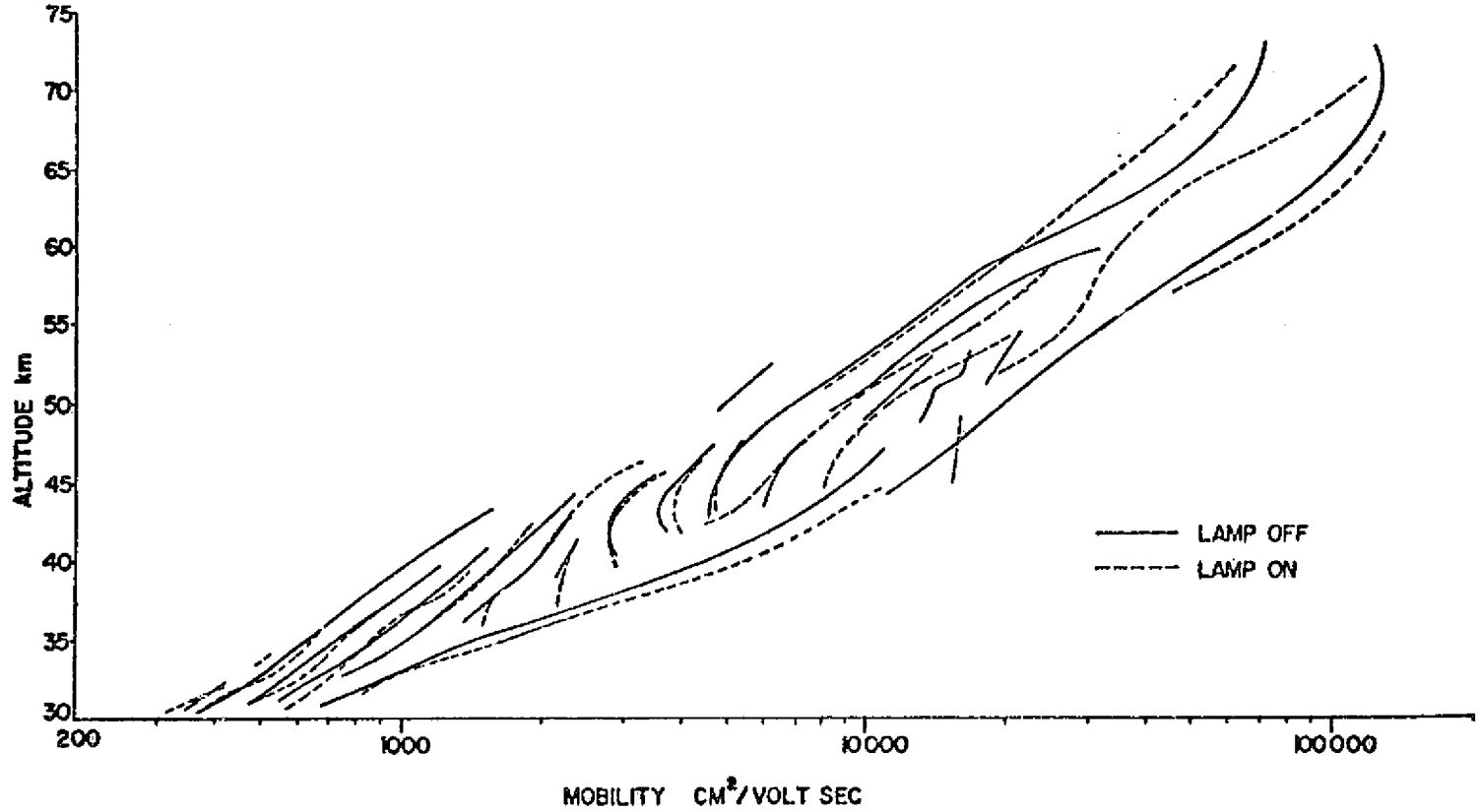

Figure 4.15: Comparison of Mobilities

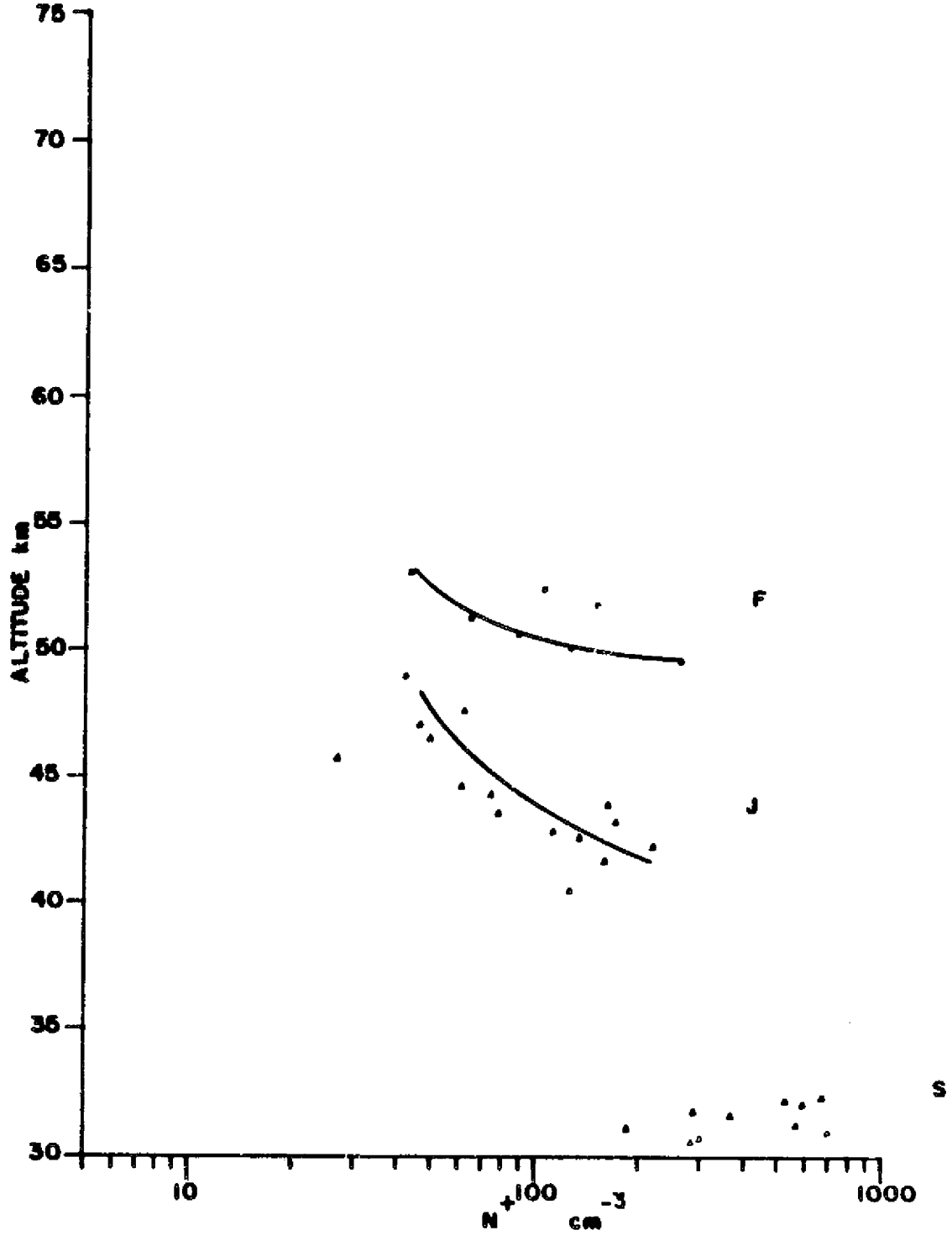

Figure 4.16: Observed Concentrations Families S, J, F

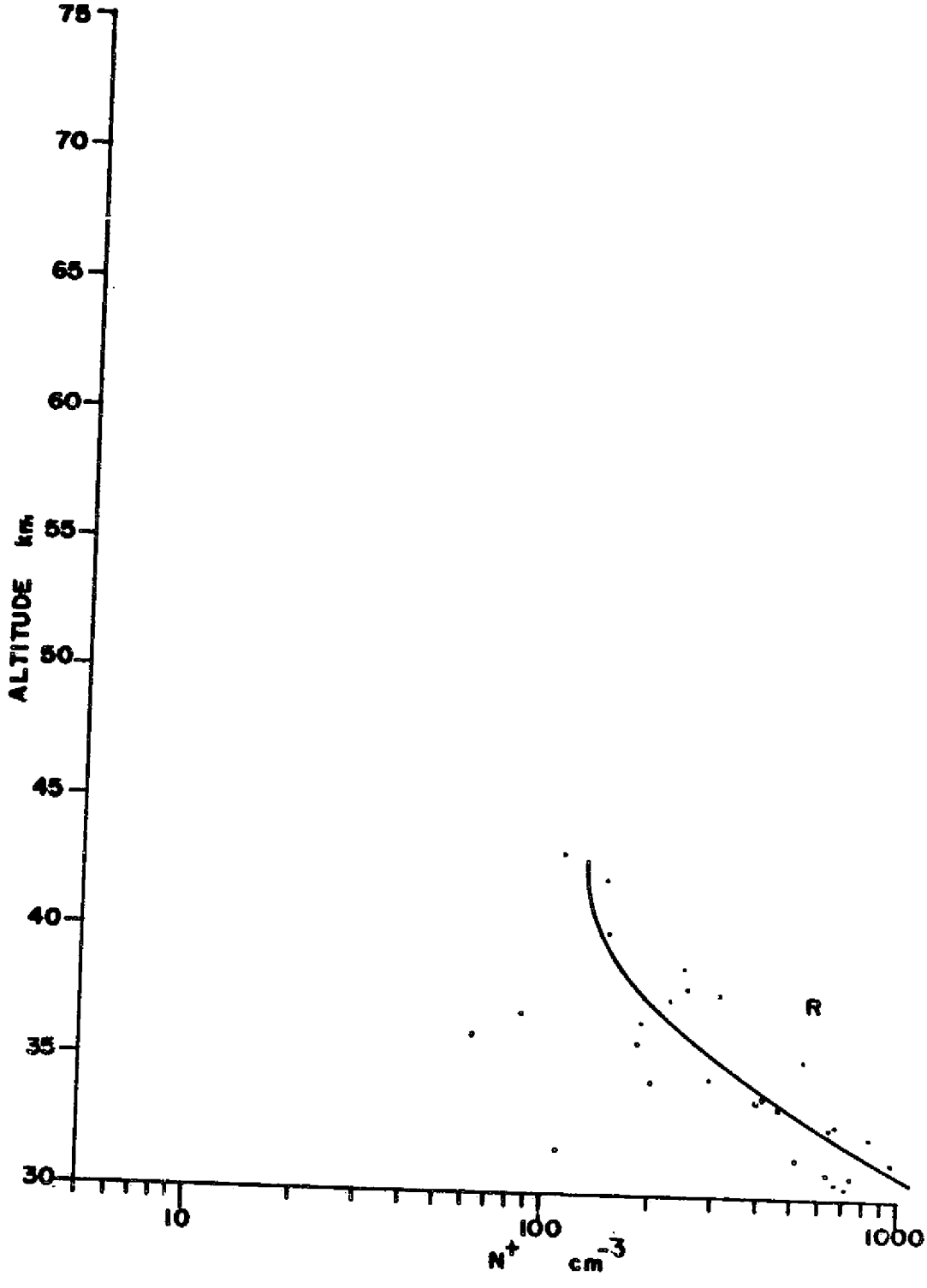

Figure 4.17: Observed Concentration Family R

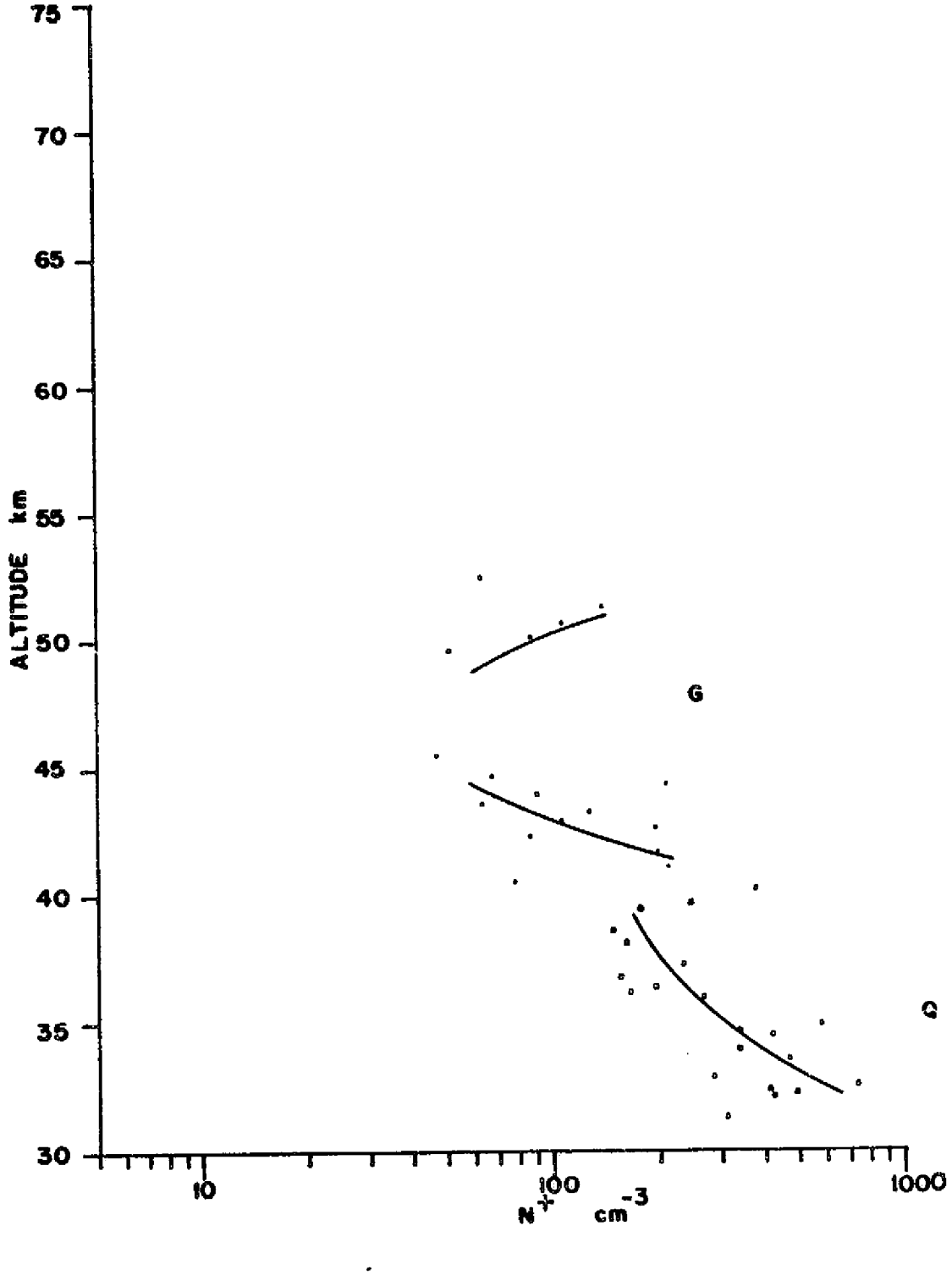

Figure 4.18: Observed Concentrations Families Q and G

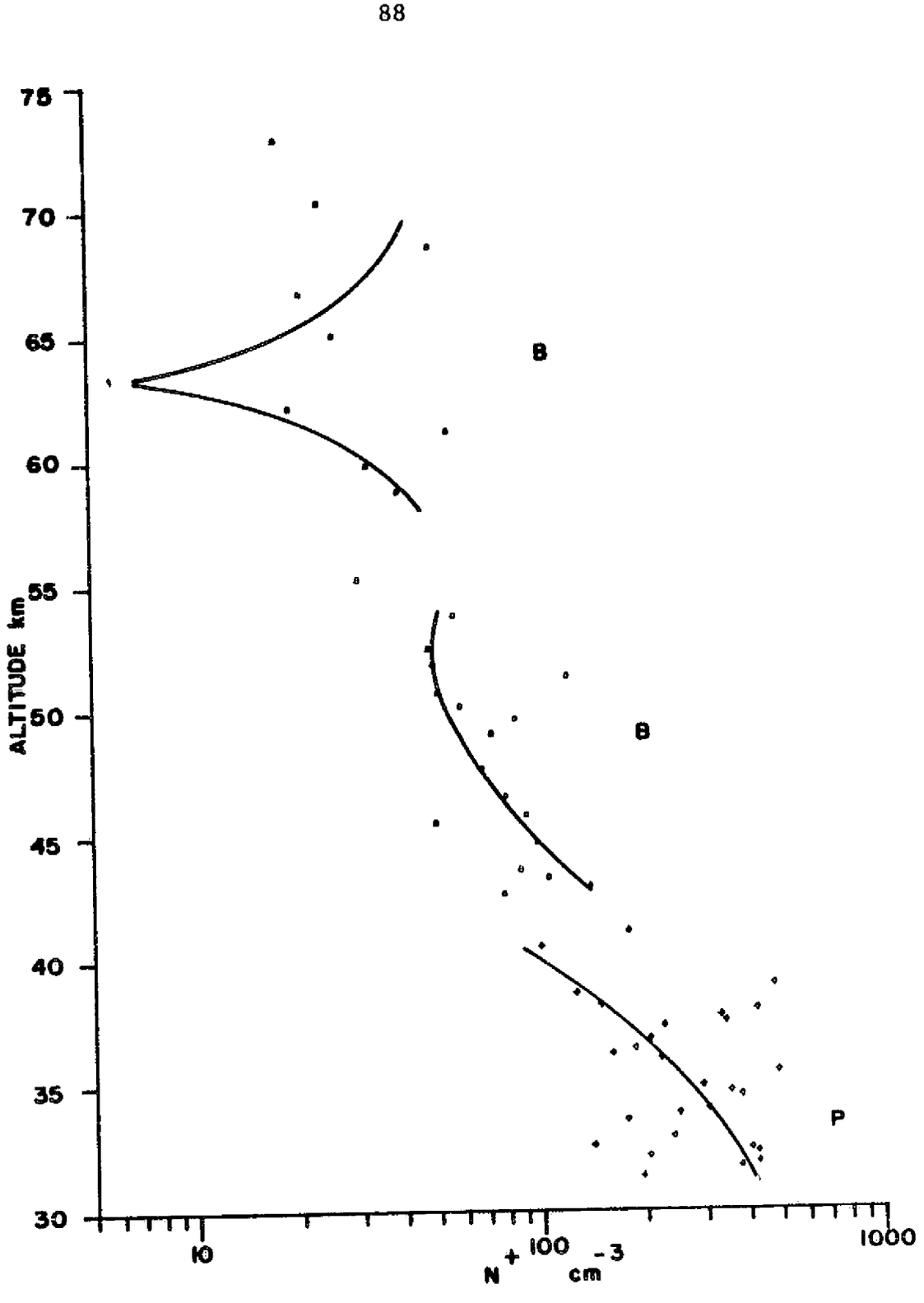

Figure 4.19: Observed Concentrations Families P and B

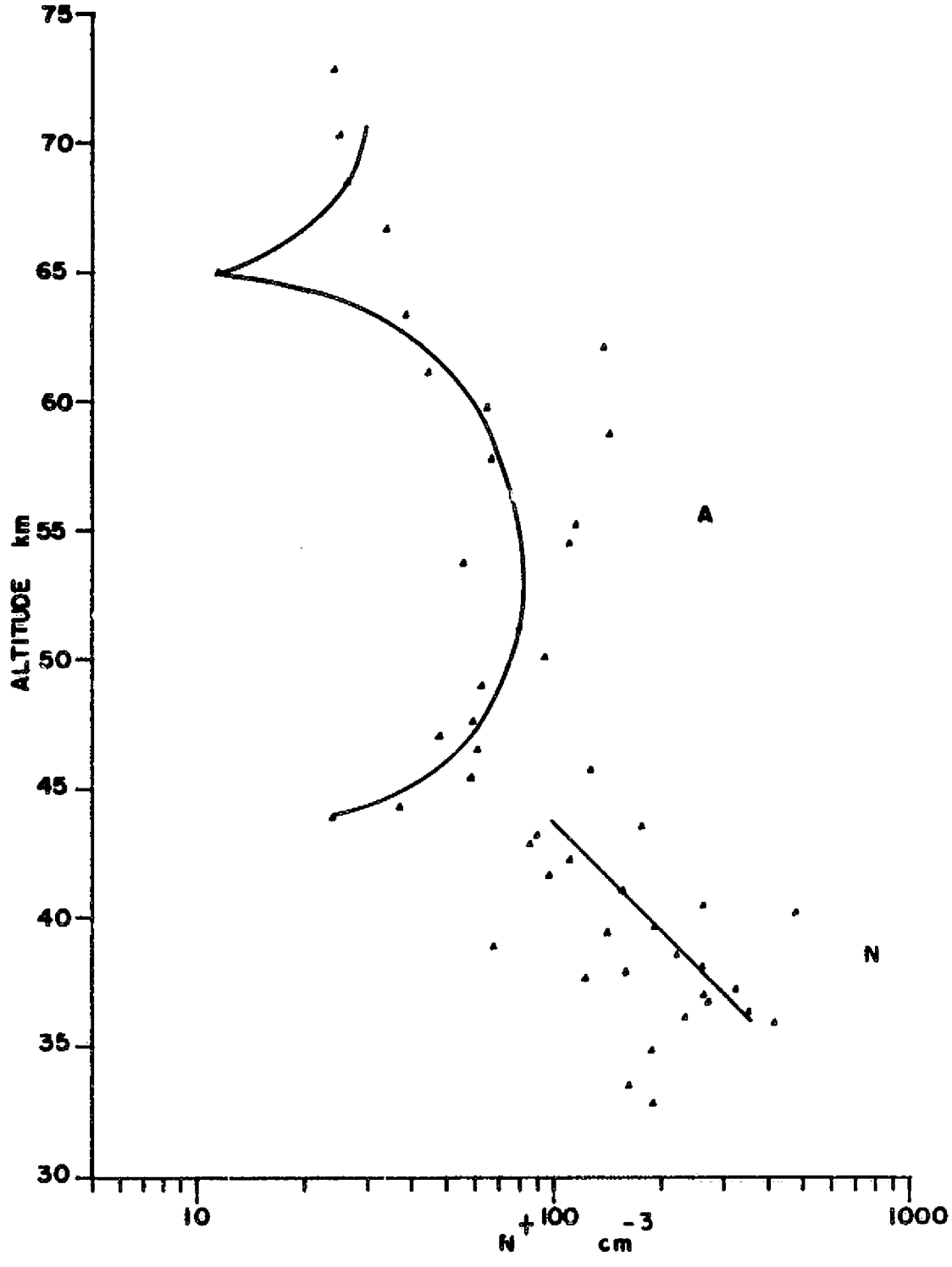

Figure 4.20: Observed Concentrations Families N and A

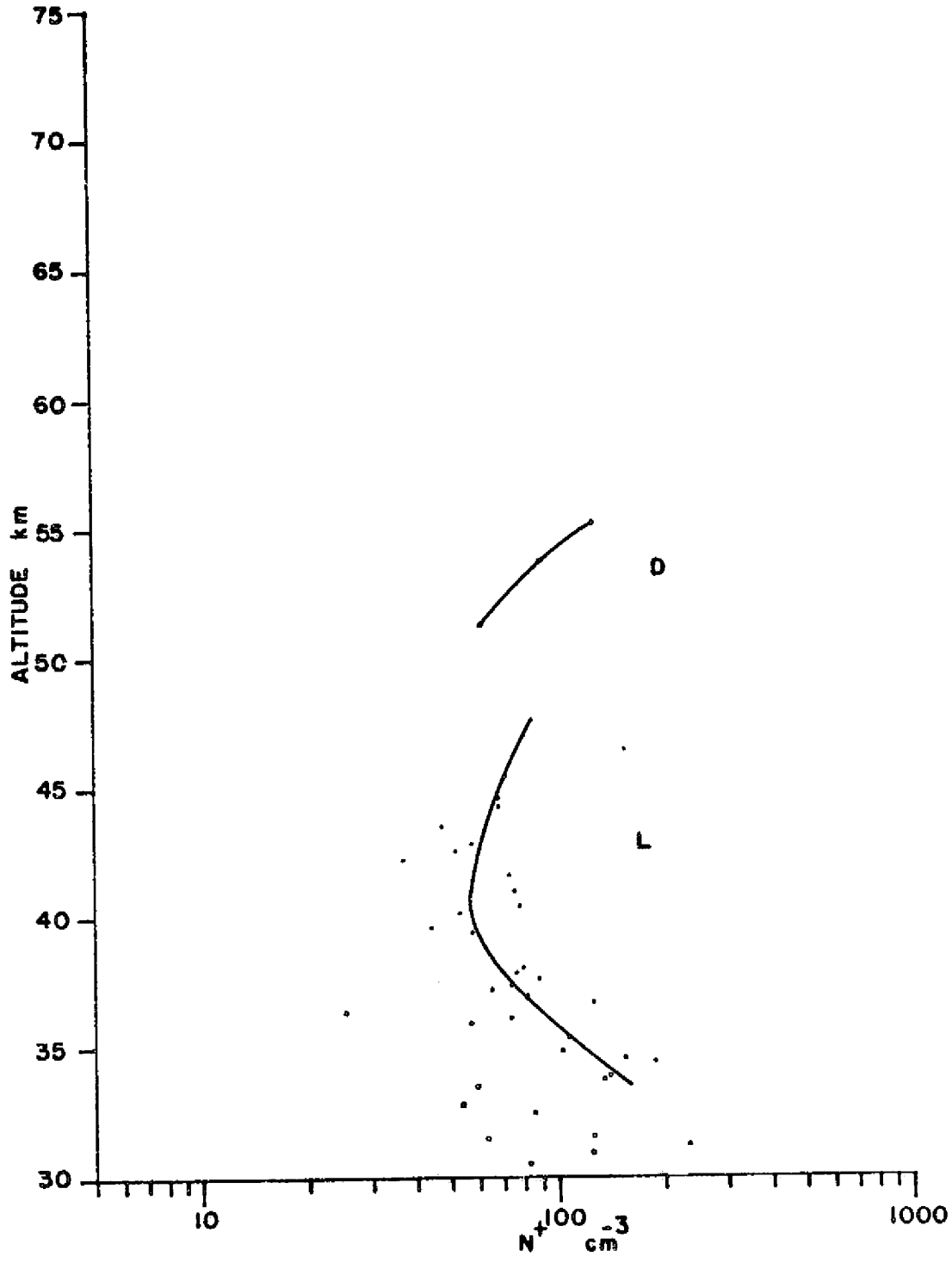

Figure 4.21: Observed Concentrations Families L and D

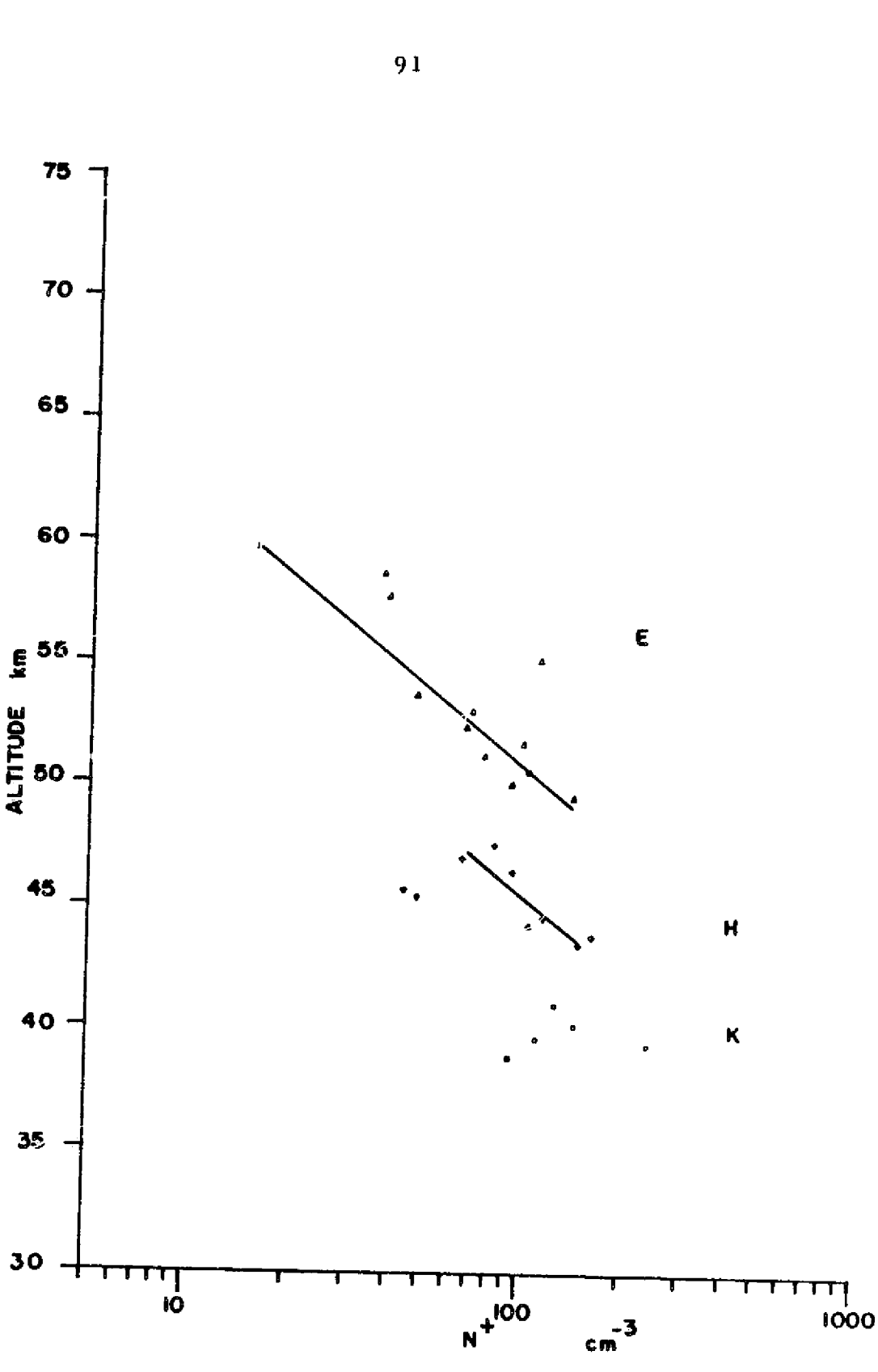

Figure 4.22: Observed Concentrations Families K, E, and H

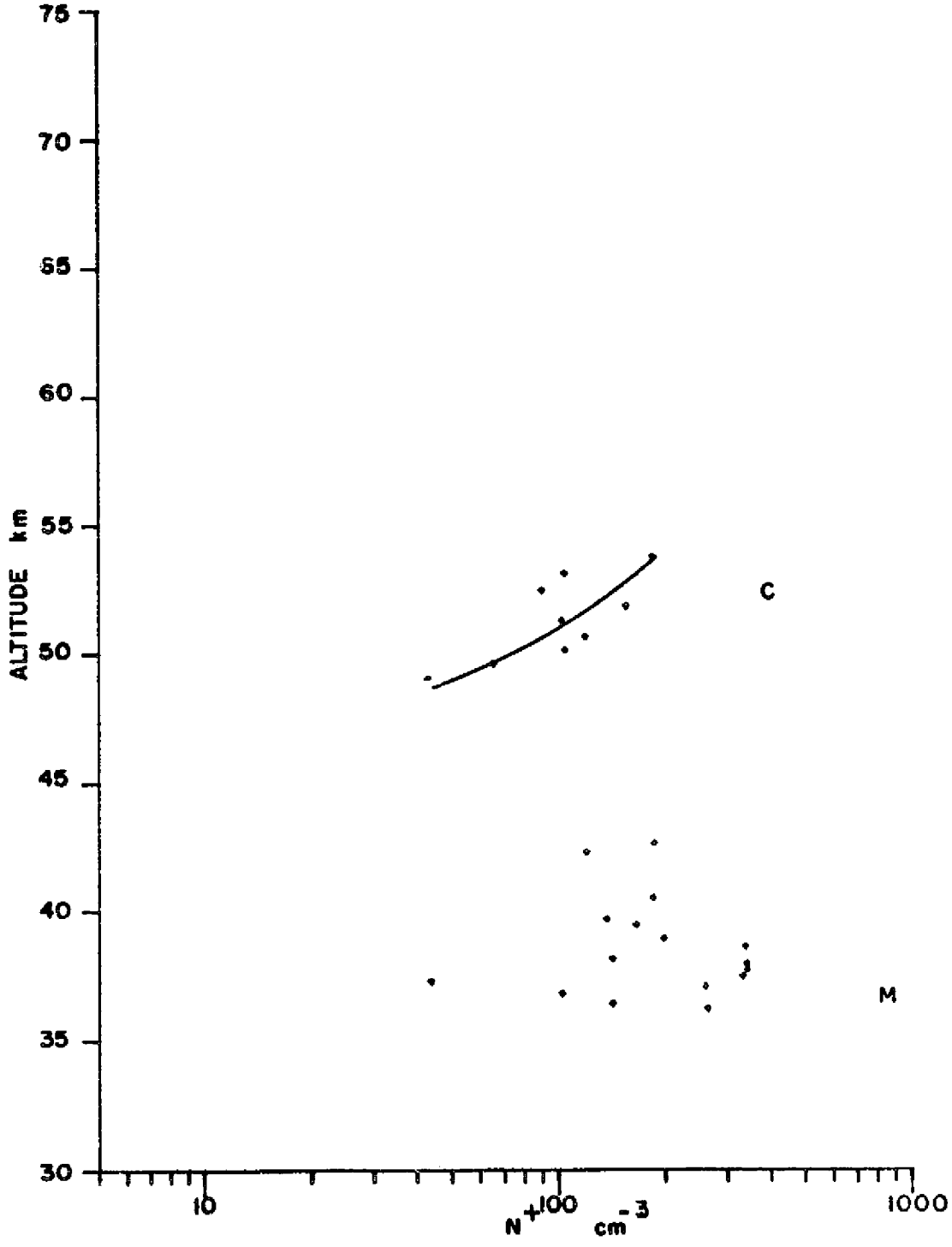

Figure 4.23: Observed Concentrations Families M and C

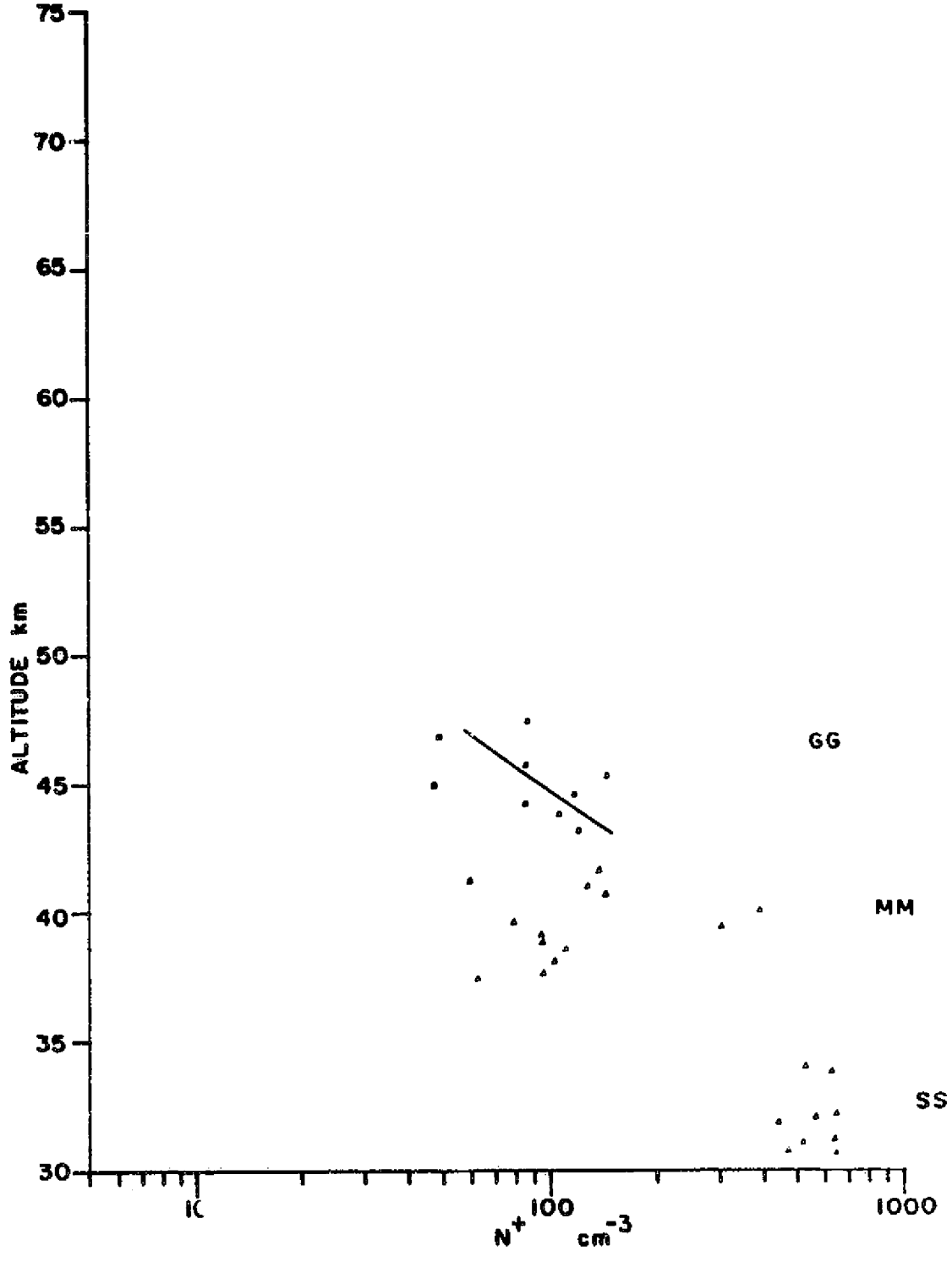

Figure 4.24: Observed Concentrations Families MM, SS, and GG

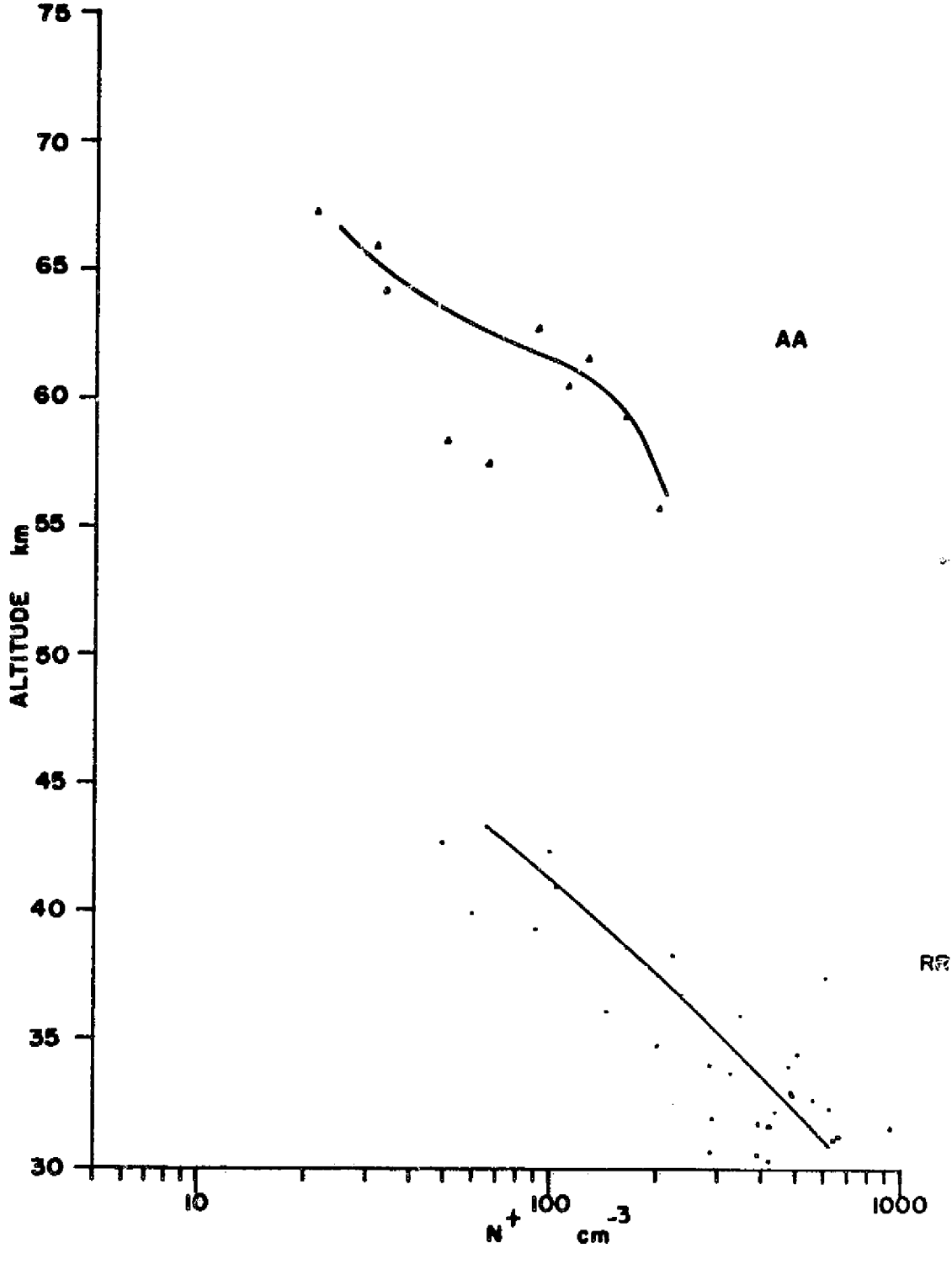

Figure 4.25: Observed Concentrations Families RR and AA

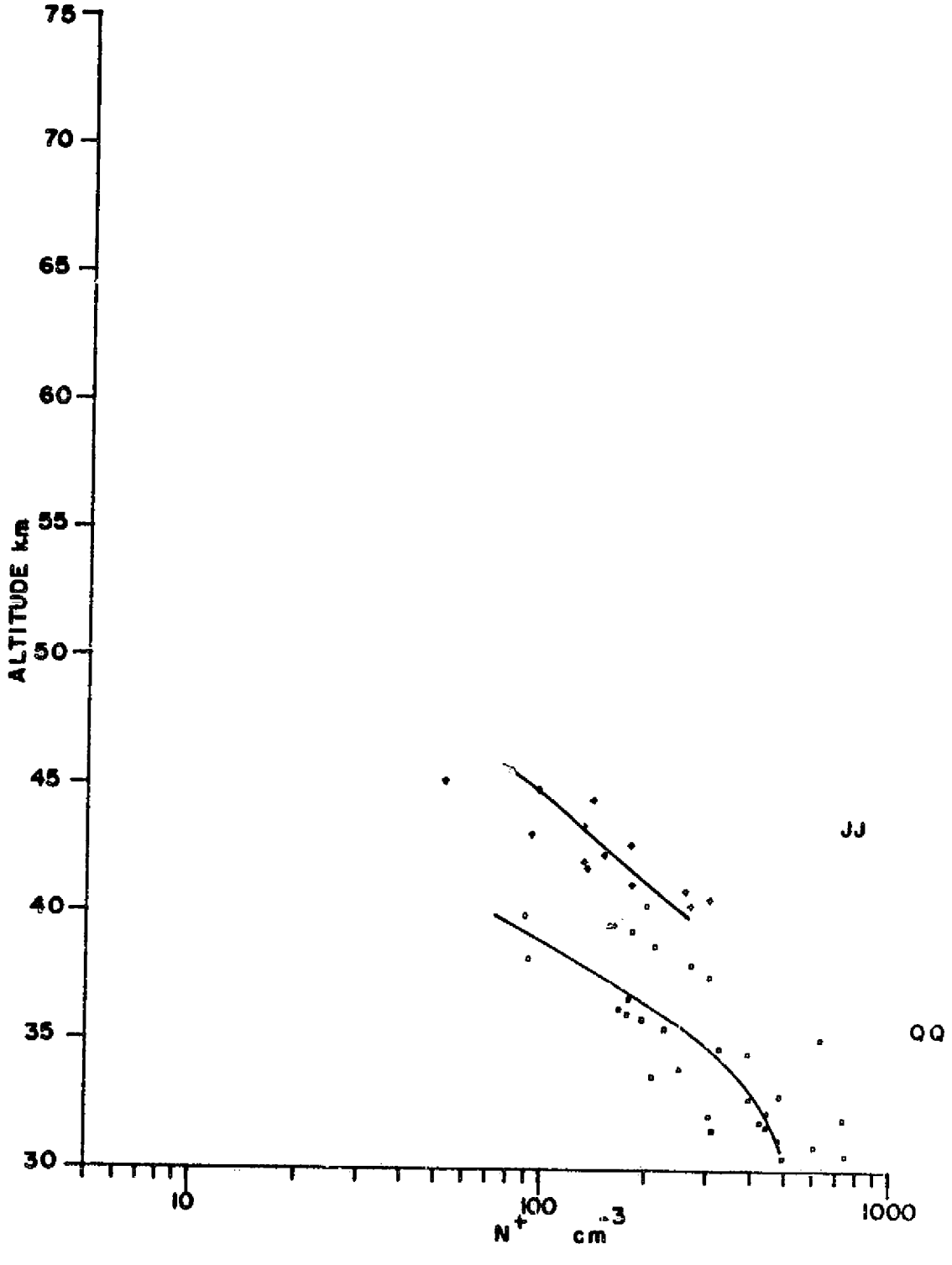

Figure 4.26: Observed Concentrations Families QQ and JJ

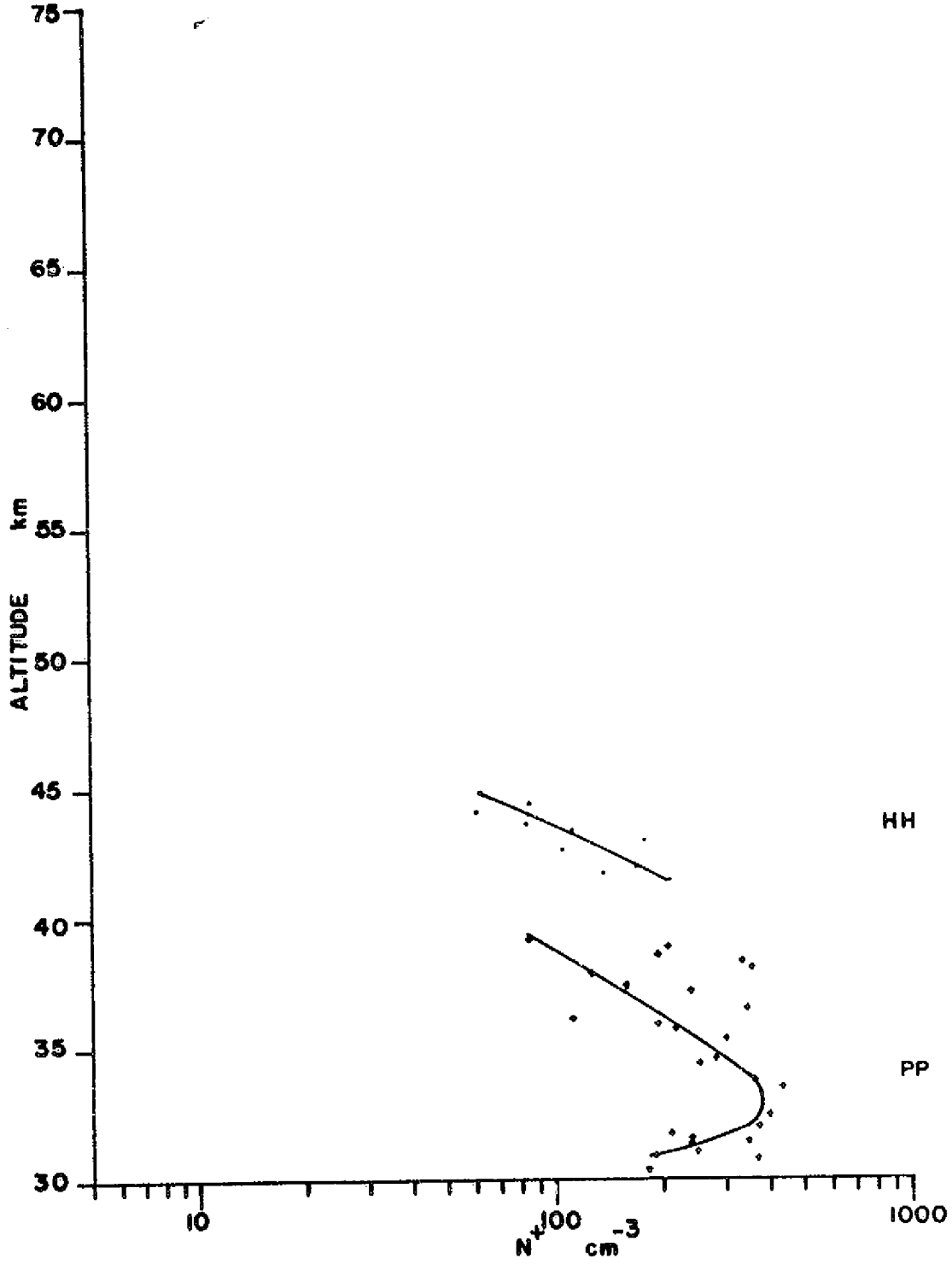

Figure 4.27: Observed Concentrations Families PP and HH

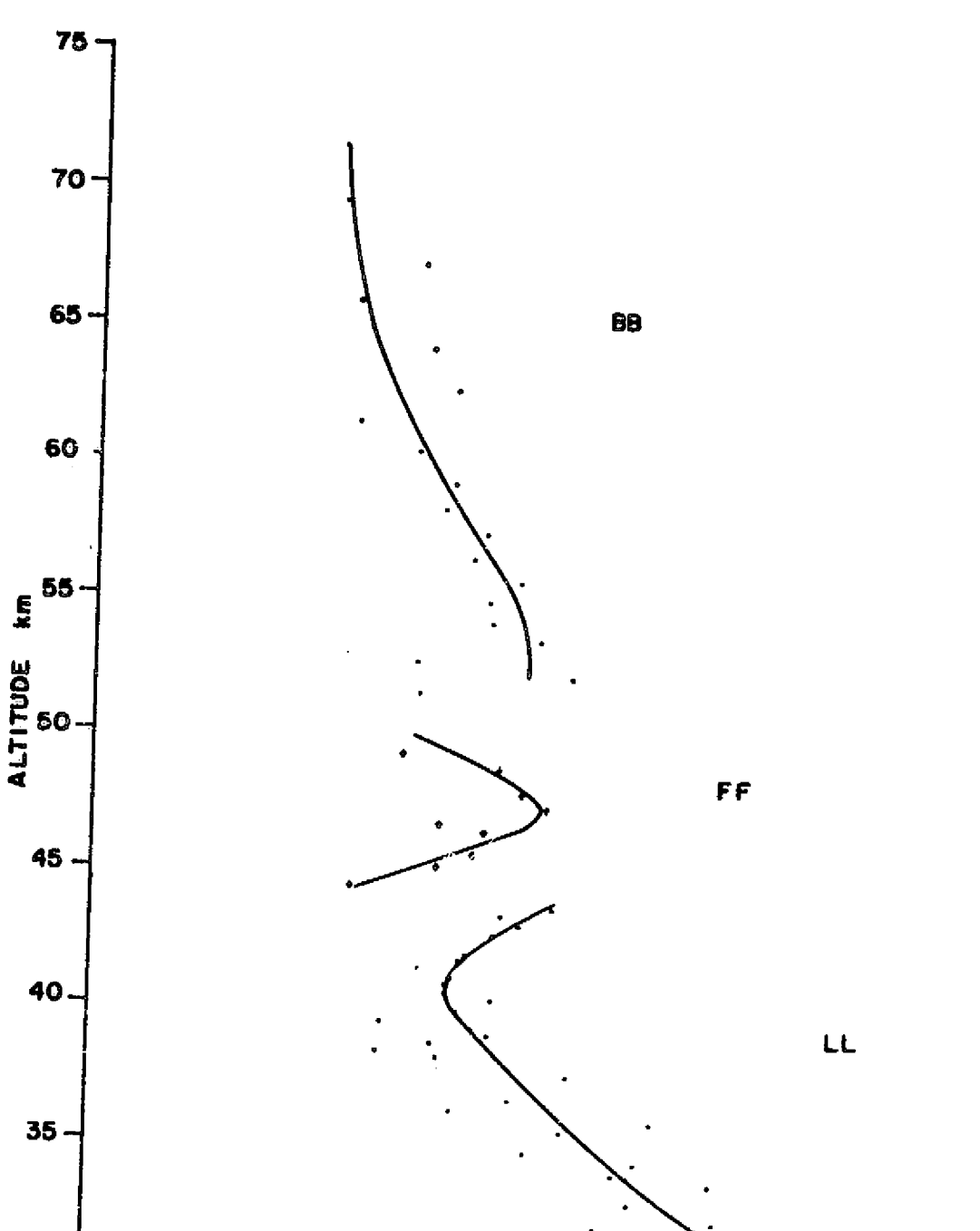

Figure 4.28: Observed Concentrations Families LL, FF, and BB

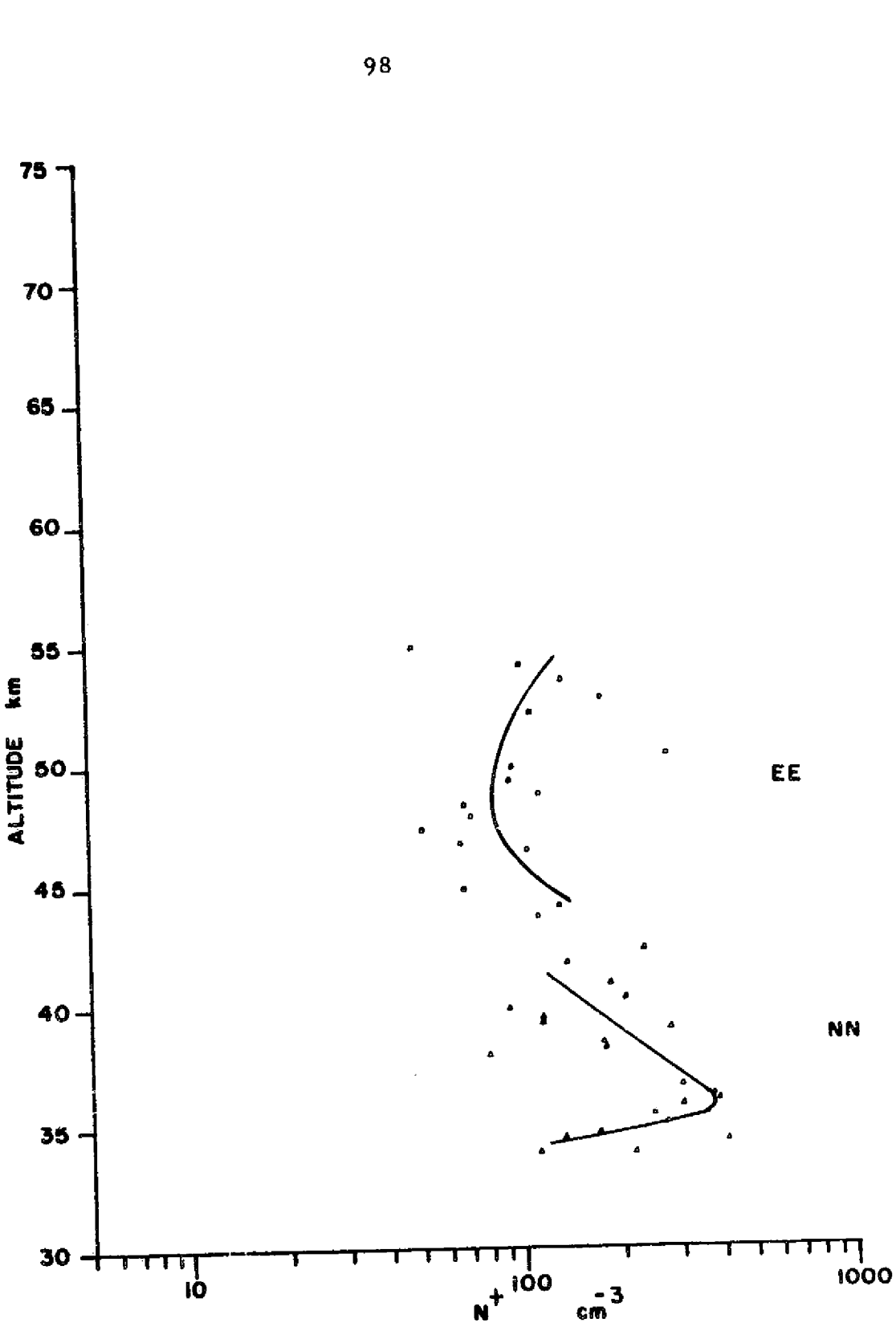

Figure 4.29: Observed Concentrations Families NN and EE

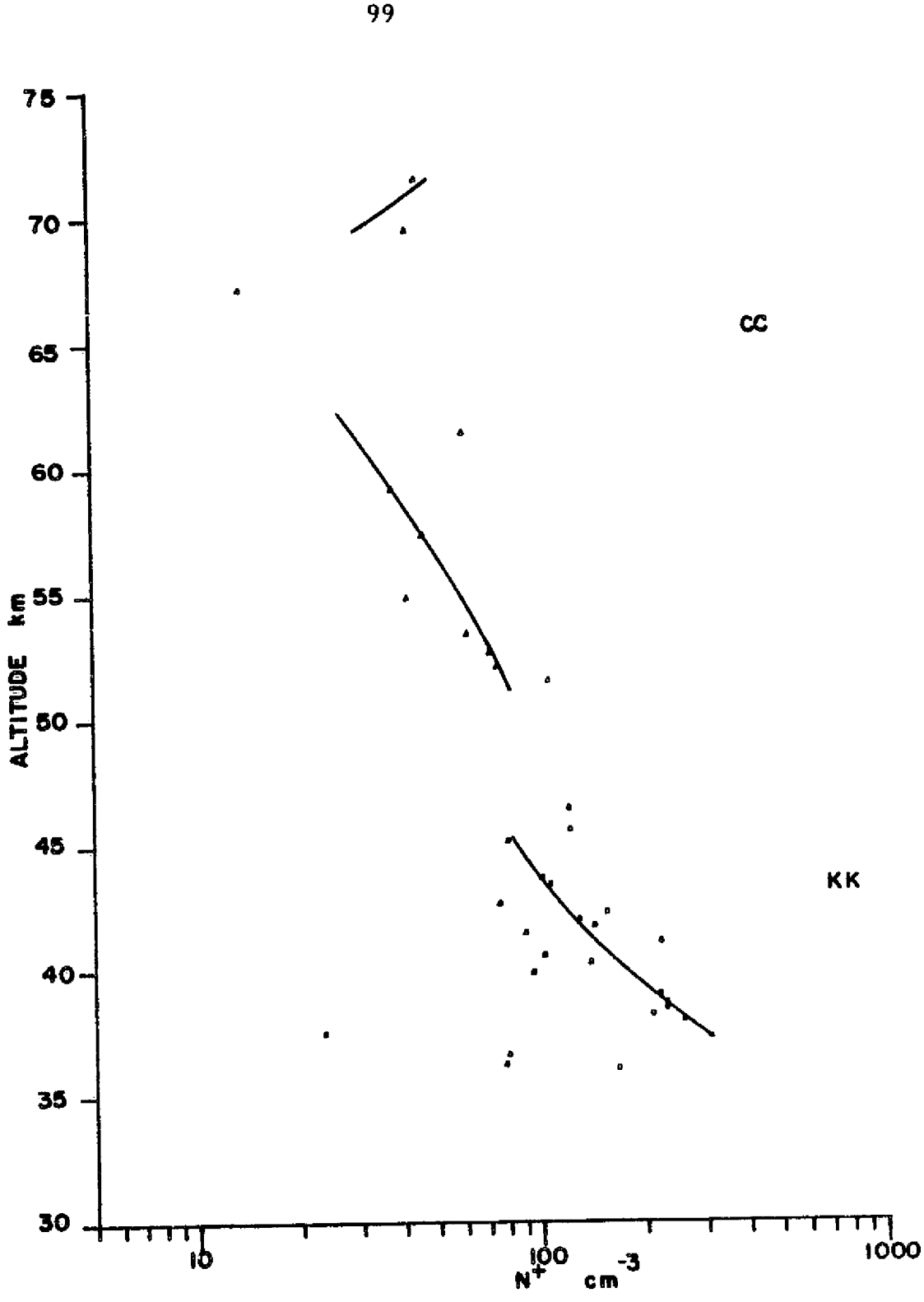

Figure 4.30: Observed Concentrations Families KK and CC.

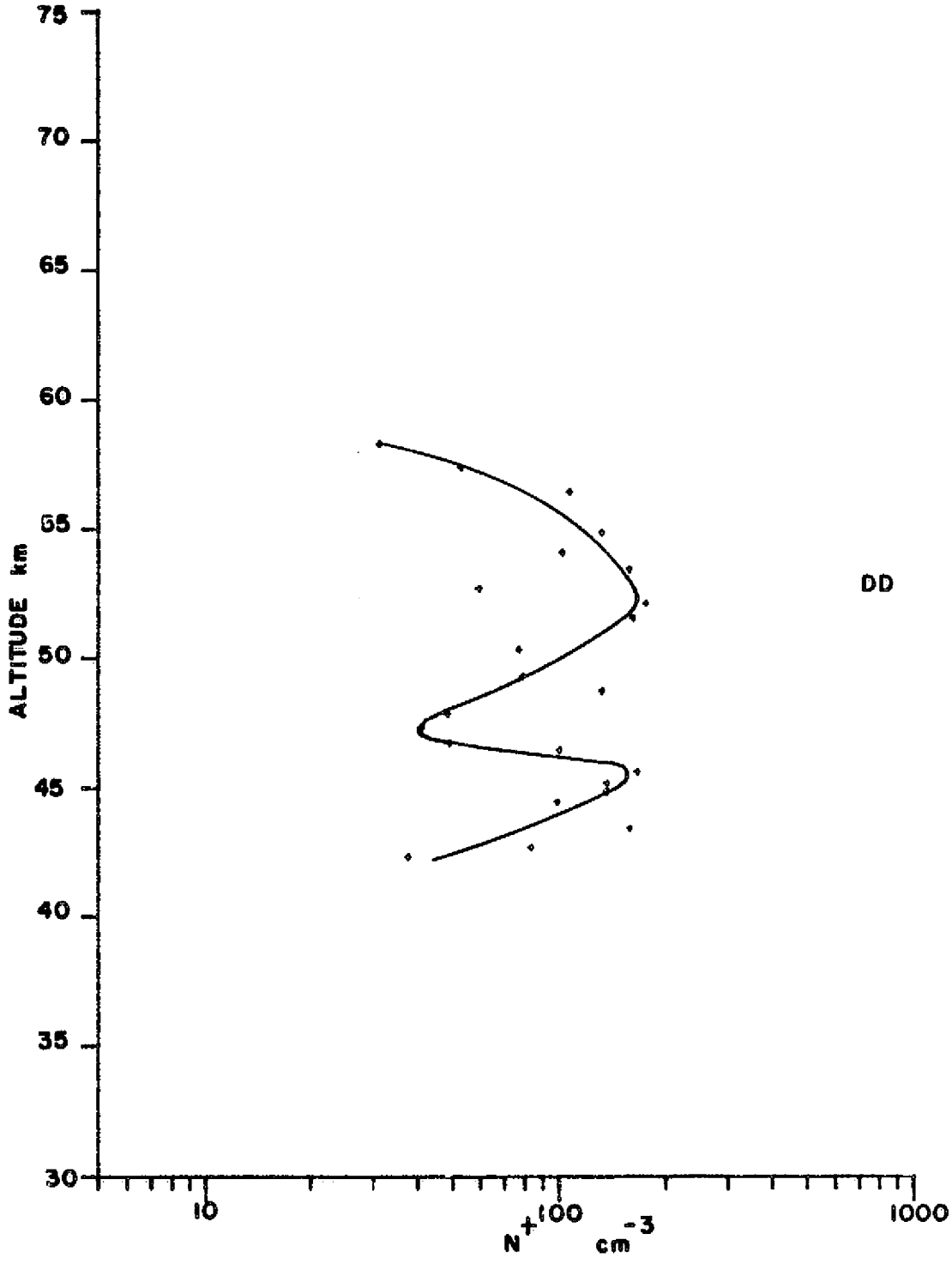

Figure 4.31: Observed Concentration Family DD

is more askew.

When a family by family comparison for lamp on-lamp off conditions is made, S to SS, R to RR, etc., the ion concentrations are found to be essentially the same, considering the scatter of the data. Of particular interest is the fact that the concentration of ion family L (Figure 4.21) is very similar to the concentration of family LL (Figure 4.26). This suggests that the effect of the lamp in this altitude region is primarily to dissociate the light ions of family L to even lighter ions of family LL and neutral water molecules. Table 4.3 presents the observed conductivity change between family L and family LL. Comparing Table 4.3 to Table 4.2, the best description is that family L is $H_3O^+ \cdot (H_2O)_3$ which is dissociated by the Lyman α source to $H_3O^+ \cdot (H_2O)_2$. A more definite determination will require a more detailed theory of how the mobility of the hydrate depends on its size.

The concentration data at higher altitudes shows varying trends, sometimes with minimums and maximums. This suggests that as the temperature changes and the concentration decreases with altitude, the relative importance of each hydrated ion type changes. It should be noted also that as the altitude is increased, heavy ions disappeared while new light ions appeared.

At the highest altitudes, the NO^+ is thought to be the major ion. Families B, MM, CC, and AA show a sharp concentration minimum around 65 km similar to that observed with the blunt probe. This corresponds to the crossover between solar Lyman α production and cosmic ray production. One disturbing result is the reduction of concentration observed with the lamp on (Figures 4.19 and 4.20).

Table 4.3: Percent Mobility Change

Altitude km	Percent Change
34.	8.6
34.5	15.3
35.	15.3
35.5	14.8
36.	12.2
36.5	15.9
37.	15.3
37.5	15.9
38.	18.0
38.5	18.6
39.	18.6
39.5	19.7
40.	19.1
40.5	19.1
41.	20.2
41.5	19.1
42.	18.6
42.5	19.7
43.	18.6
43.5	19.1
44.	20.2

It is felt that this is due to an induced surface charge on the window of the lamp produced by the strong Lyman α flux. This surface charge may be large enough to deflect the high mobility ions of this region away from the entrance of the Gerdien condenser. A possible solution to this problem will be discussed in Chapter V.

4.3 Astrobee D Flight History

The Astrobee D payload described in Chapter III was test-fired from White Sands Missile Range on July 15, 1975, 1403 GMT. The radar-observed altitude is shown in Figure 4.32. This payload used a 28 foot disk gap band parachute rather than the inflatable ring Starute of the Super Arcas payload. As can be seen in Figure 4.33, the maximum descent velocity was less for this payload; however, inspection of the data shows a much stronger angle of attack component, which makes the determination of multiple ion types more difficult.

During calibration environment tests a trimpot in the logarithmic differentiator was observed to change positions. Since absolute accuracy on this channel was not necessary for the proof of the concept, this was not deemed critical. In general, the logarithmic section worked properly, but the transitions between ion types occur too quickly to be easily discerned. Slope fitting to the direct data channel is easier.

During the actual flight the trimpot used to adjust the dV/dt compensation was observed to vary. (These trimpots were of a new type not previously used.) The intermittent contact of this trimpot produced varying amounts of noise directly into the electrometer. As a result, only a small fraction of the data was useable.

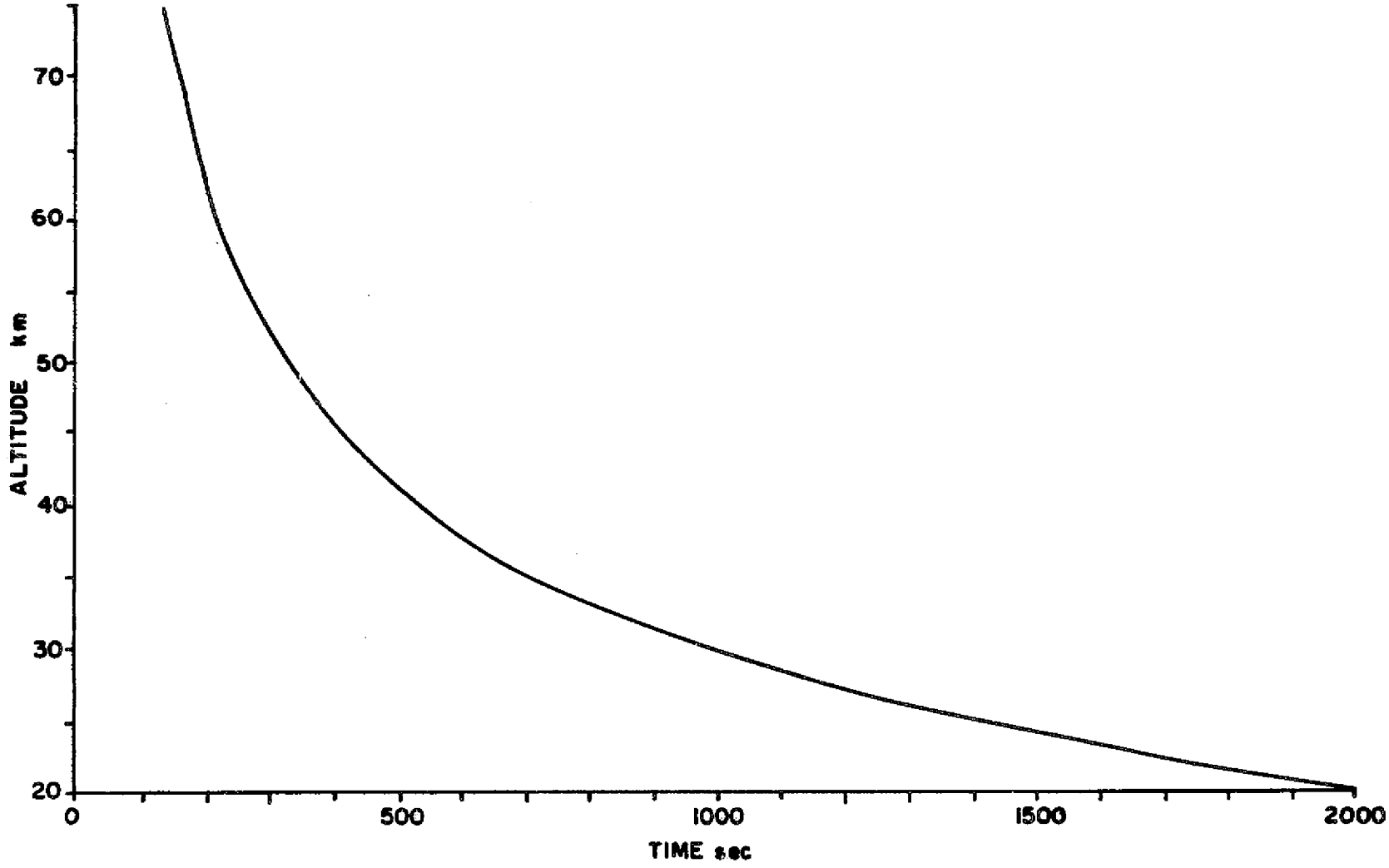

Figure 4.32: Altitude vs. Time for Astrobee D Payload

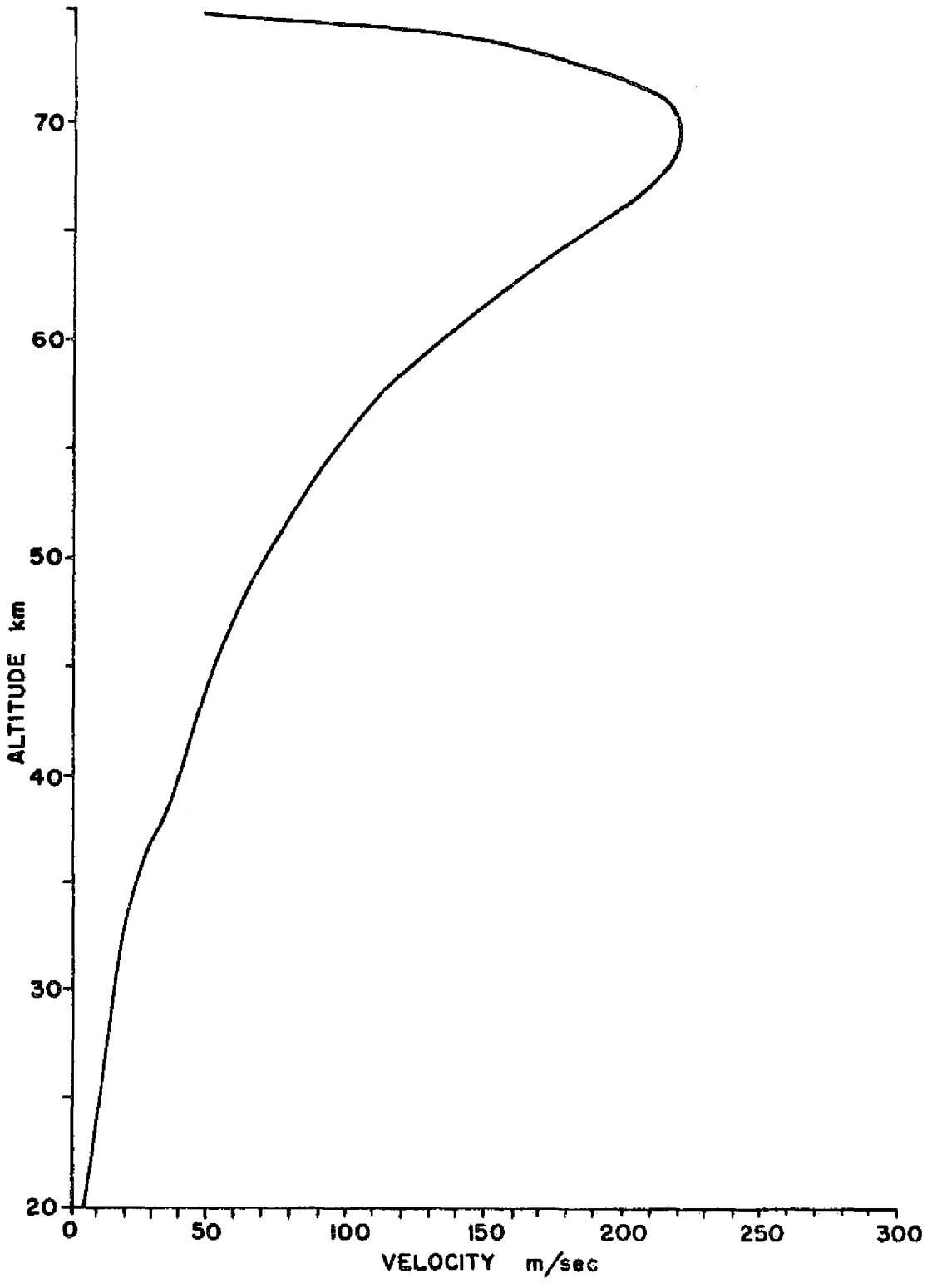

Figure 4.33: Altitude vs. Velocity for Astrobee D Payload

4.4 Astrobee D Payload Data

Figure 4.34 presents the observed mobilities for the lamp off while Figure 4.35 shows the results for the lamp on. The most interesting thing at the 70 km region is the apparent absence of the heaviest group when the lamp is on (six data points for lamp off, one data point for lamp on). This suggests that these heavy ions, perhaps ice particulates, are dissociated by the Lyman α radiation.

At the lower altitudes, there are not enough data points to determine particular family types, but there is some indication of a difference with the lamp on or off. The concentrations are presented by Figure 4.36 for the lamp off and Figure 4.37 for the lamp on. The concentration for the lamp on has a deeper minimum than that for the lamp off, again probably due to a surface charge on the window face.

No observable change in low altitude conductivity due to the lamp was observed, but the noise-produced scatter in the data was so large that the small percentage difference would not be possible to detect. Also this particular lamp intensity was three times smaller than that of the Super Arcas payload.

In general, the data from the Astrobee D flight supports the results from the Super Arcas flight.

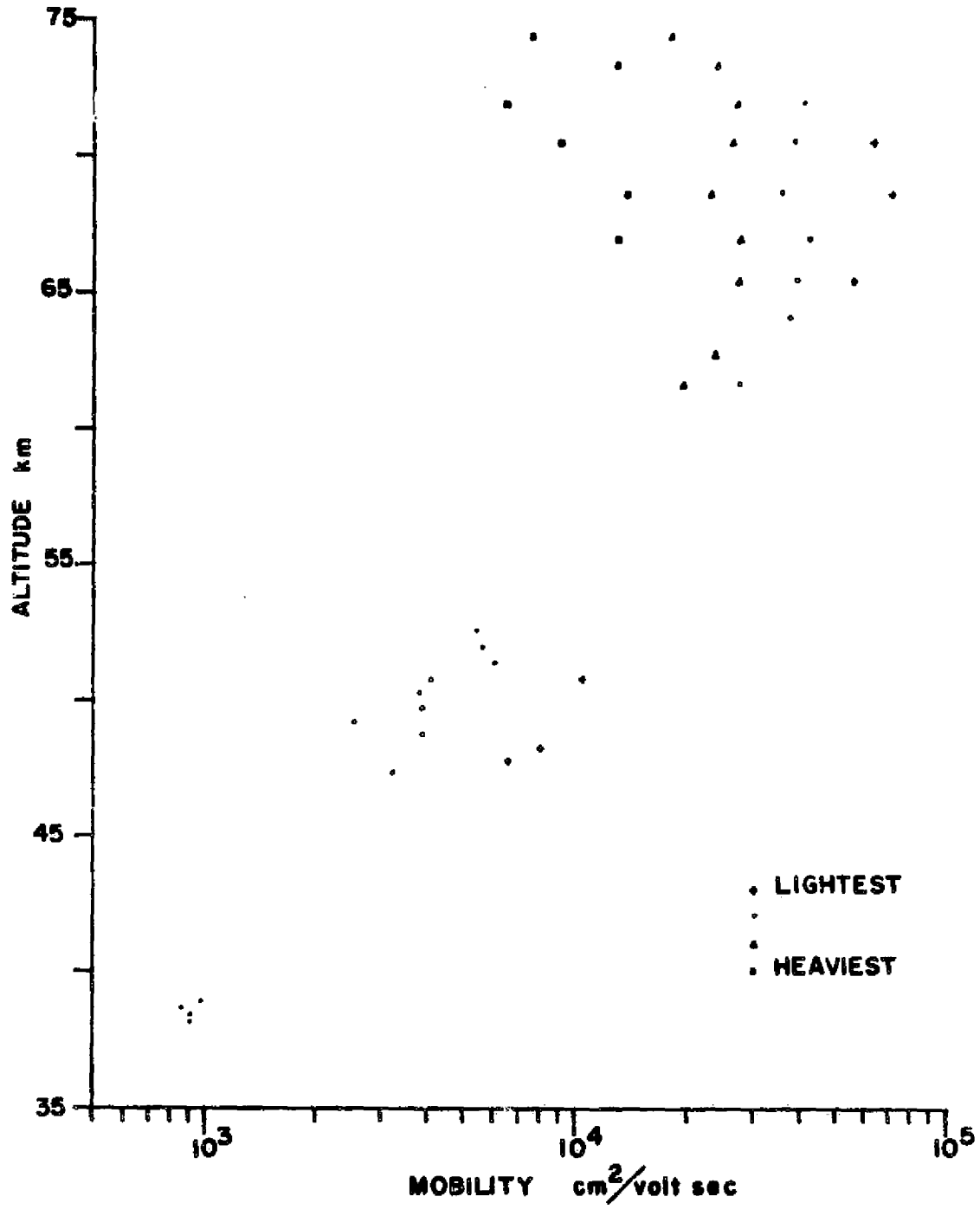

Figure 4.34: Observed Mobilities, Lamp Off

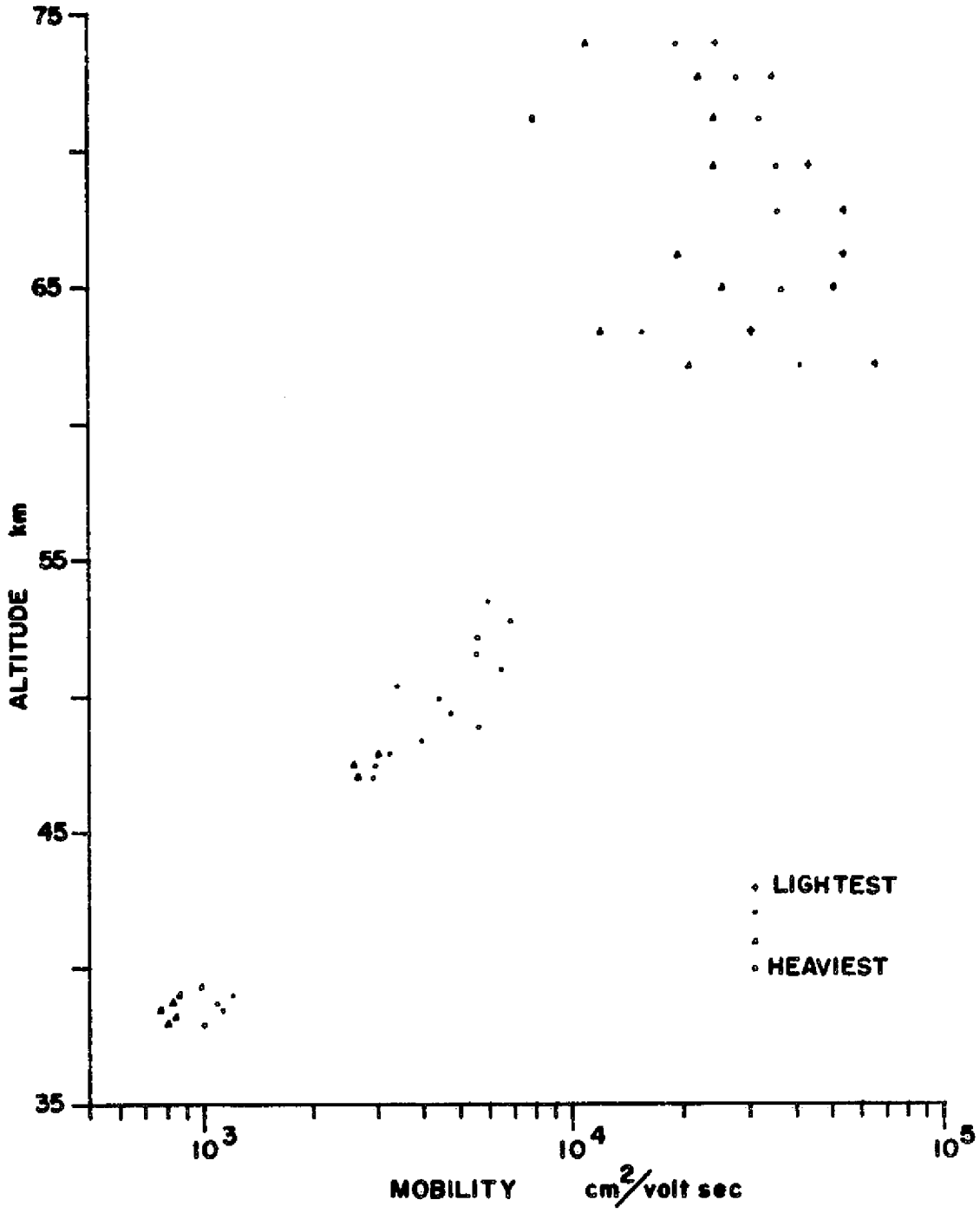

Figure 4.35: Observed Mobilities, Lamp On

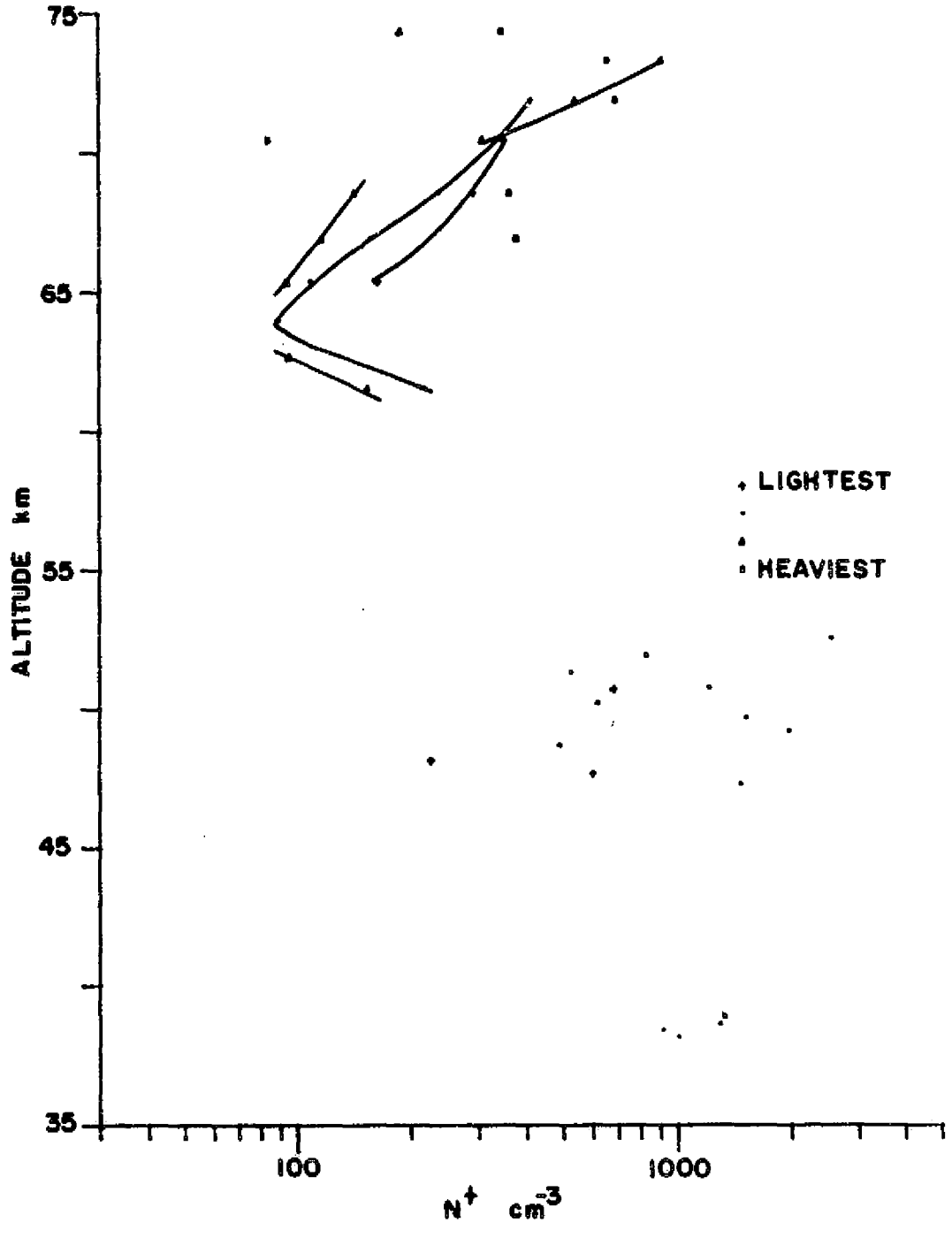

Figure 4.36: Observed Concentrations, Lamp Off

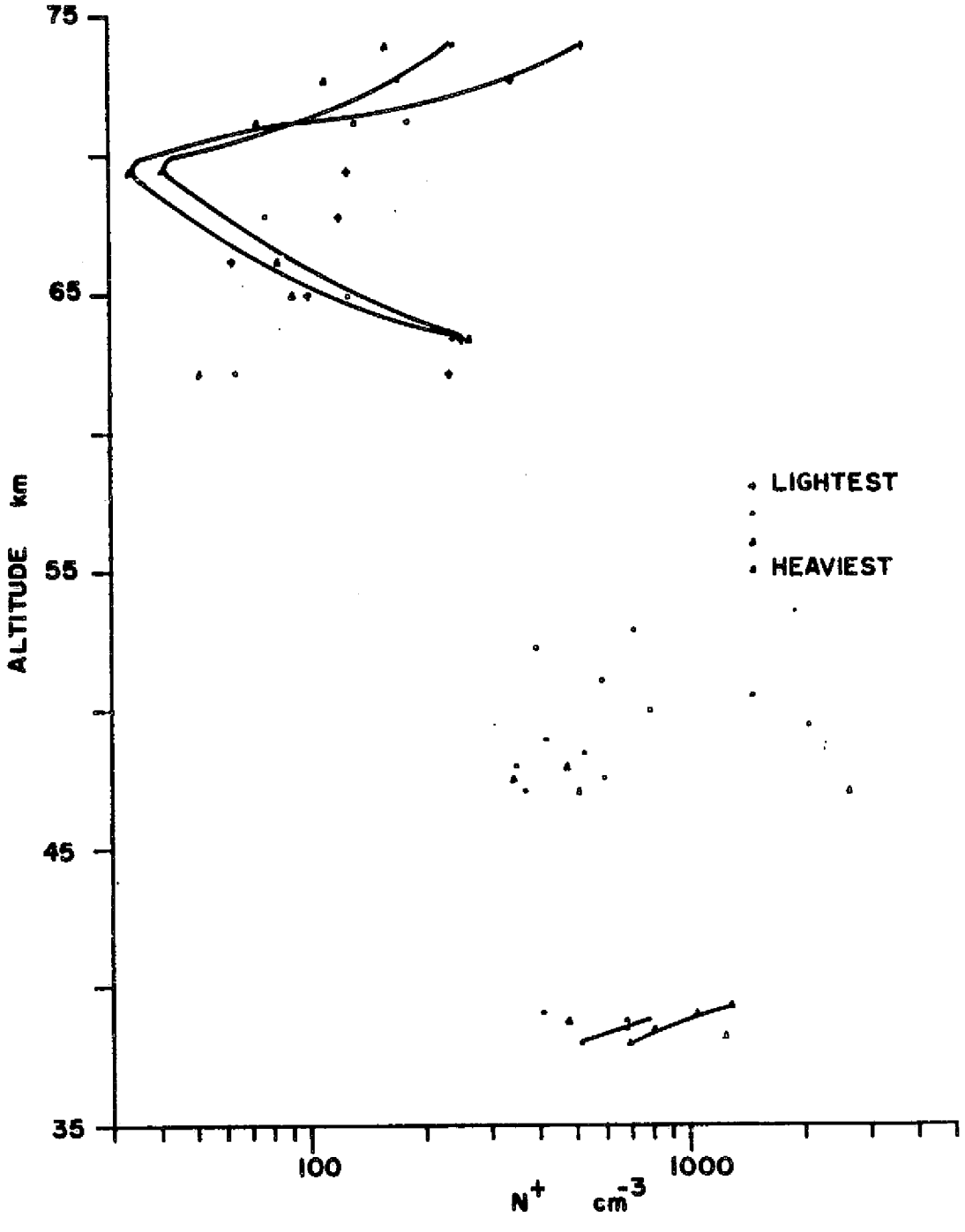

Figure 4.37: Observed Concentrations, Lamp On

CHAPTER V

SUMMARY AND RECOMMENDATIONS

5.1 Summary

A subsonic Gerdien condenser has been developed for mesospheric and stratospheric measurements. The inclusion of a Lyman α ultraviolet source has provided information about the effect of Lyman α radiation. It has been found that in the 30-50 km region, the increased conductivity observed with the lamp on is due to a change in mobility, not concentration. This is probably due to dissociation of a hydrated ion, as such artifically produced positive conductivity may not be an indication of NO concentration.

Contrary to some belief, ions can be separated into groups by mobility with a fair degree of consistency. There is some evidence that at 70 km, heavy ions (possibly ice particulates) are dissociated by Lyman α radiation.

The observed mobilities of this work are compared with that of Rose and Widdel (1972) in Figure 5.1. The mobilities of the Super Arcas flight are somewhat higher than expected, perhaps due to the more restricted aerodynamic flow of this payload (Figure 3.8) compared to the more open geometry of the Astrobee D payload which is in better agreement with expectations.

The unusually large mobility values from the Super Arcas flight could be due to either the higher latitude or fragments produced during an energetic auroral breakup. An in-flight calibration of the mobility instrument would be useful.

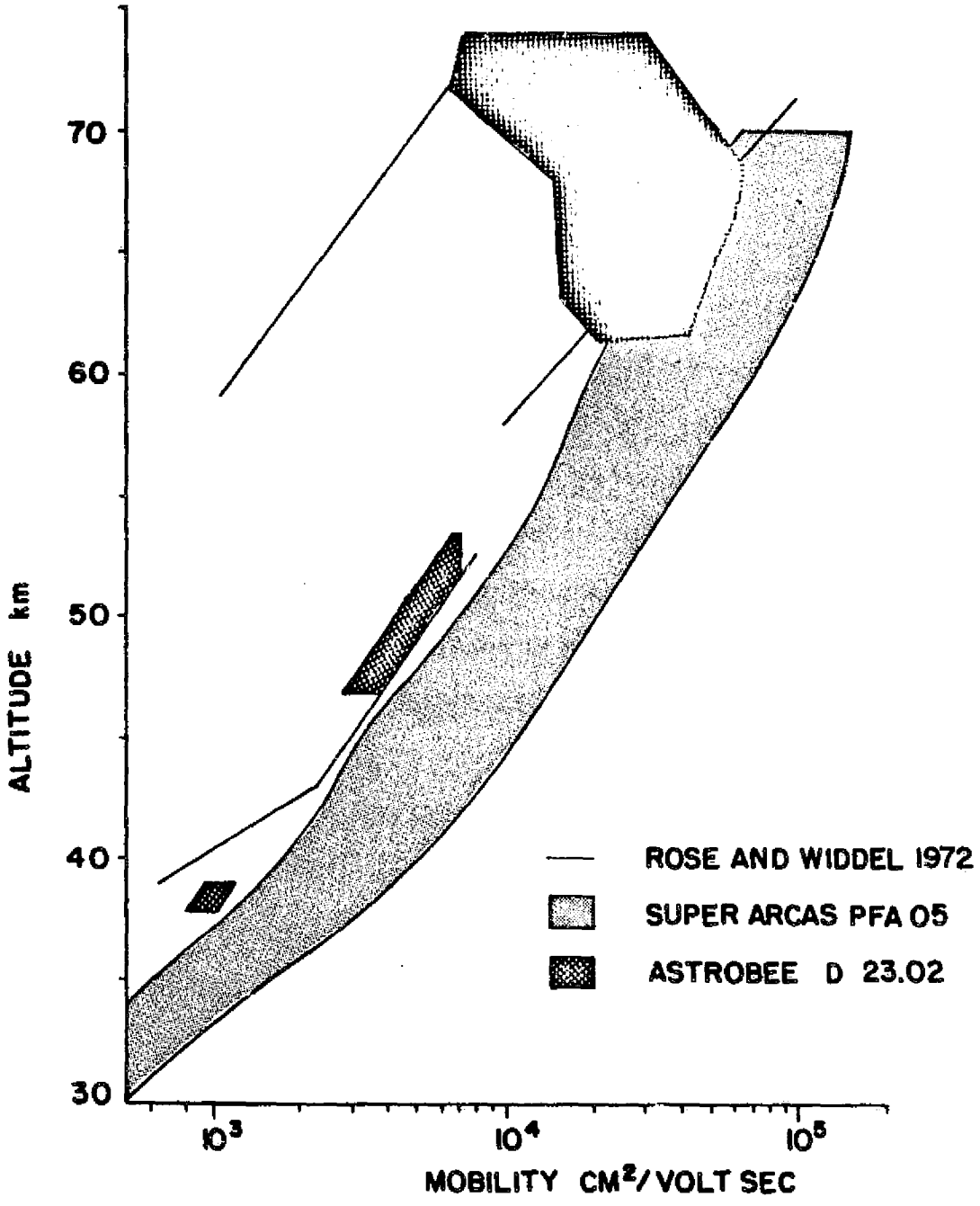

Figure 5.1: Comparison of Observed Mobilities to that of Rose and Widdel

5.2 Recommendations

Two payload modifications are being incorporated for the next launches.

A double ring collector with two electrometers will be used. The ratio of L_3 to L_1 will be 17/16, while at the same time the collector current of the front section of length L_1 will also be measured. This will increase the resolution of the system and should make the data reduction easier.

The insulating rings between the collector and guard sections are being redesigned so that only an air gap is at the outer surface. It is felt that surface charges on exposed insulating rings may produce erratic results.

To reduce the possible effect of a surface charge on the window of the lamp forcing away the high mobility ions, a Faraday shield around the front of the lamp will be used. With the lamp recessed into the center post, the surrounding guard section will shield any such surface charge. The collimation of the beam which results will reduce the expected production by a factor of two.

More difficult problems still remain, such as providing a real time lamp intensity monitor and measuring the fluid flow through the system.

Laboratory and theoretical studies should be done to identify the actual constituents of the different mobility groups observed so that the data can be applied to improving models of the atmosphere.

REFERENCES

Ackerman, M., D. Frimout, C. Muller, D. Nevejans, J. C. Fontanella, A. Girard, and N. Louisnard, Stratospheric nitric oxide from infrared spectra, Nature, 245, 205, 1973.

Barth, C. A., Rocket measurement of the nitric oxide dayglow, J. Geophys. Res., 69, 3301, 1964.

Blackwood, O., The existence of homogeneous groups of large ions, Phys. Rev., 16, 85, 1970.

Bossolasco, M., and A. Elena, C. R. Acad. Sci., 256, 4491, 1963.

Bourdeau, R. E., and E. C. Whipple, private communication in A subsonic probe for the measurement of D-region charged particle densities, R. G. Willis, Scientific Report No. 245, Ionosphere Research Laboratory, The Pennsylvania State University, 1965.

Bourdeau, R. E., E. C. Whipple, and J. F. Clark, Analytical and experimental electrical conductivity between the stratosphere and ionosphere, J. Geophys. Res., 64, 1363, 1959.

Bowhill, S. A., E. A. Mechtly, C. F. Sechrist, Jr., and L. G. Smith, Rocket ionization measurements on a winter day of high absorption, Space Res. VII (Edited by R. L. Smith-Rose), North-Holland Publishing Co., Amsterdam, 246, 1967.

Brasseur, G., and M. Nicolet, Chemospheric processes of nitric oxide in the mesosphere and stratosphere, Aeronomica Acta A-No. 113, Institut d'Aeronomie Spatiale de Belgique, 1973.

Buttler, W. P., Pseudo-saturating power converter, Technical Support Package for NASA TECH BRIEF 72-10042, 1972.

Chesworth, E. T., The role of ice particulates in the electrification of the air in the mesosphere, Ph.D. Thesis in Physics, The Pennsylvania State University, 1974.

Chesworth, E. T., and L. C. Hale, Ice particulates in the mesosphere, Geophys. Res. Lett., 1, 347, 1974.

CIRA 1972, COSPAR International Reference Atmosphere, North-Holland Publishing Co., Amsterdam, 1965.

Cole, R. K., and E. T. Pierce, Electrification in the earth's atmosphere for altitudes between 1 and 100 kilometers, J. Geophys. Res., 70, 2735, 1965.

Conley, T. D., Mesospheric positive ion concentrations, mobilities, and loss rates obtained from rocket-borne Gerdien condenser measurements, Radio Sci., 9, 575, 1974.

Cuffin, B. N., A circular slot antenna for use on ionospheric probes, Scientific Report No. 346, Ionosphere Research Laboratory, The Pennsylvania State University, 1965.

Farrokh, Hashem, Design of a simple Gerdien condenser for ionospheric D-region charged particle density and mobility measurements, Scientific Report No. 433, Ionosphere Research Laboratory, The Pennsylvania State University, 1975.

Fehsenfeld, F. C., and E. F. Ferguson, Origin of water cluster ions in the D region, J. Geophys. Res., 74, 2217, 1969.

Ferguson, E. E., D-region ion chemistry, Rev. Geophys., 9, 997, 1971.

Fontanella, J. C., A. Girard, L. Gramont, and N. Louisnard, Vertical distribution of NO, NO_2 and HNO_3 as derived from stratospheric absorption infrared spectra, Proc. Third Conf. CIAP, DOT-TSC-OST-74-15, 217, 1974.

Gee, E. L., A subsonic D-region probe experiment using an ultraviolet source to produce ions and free electrons, Scientific Report No. 286, Ionosphere Research Laboratory, The Pennsylvania State University, 1966.

Hale, L. C., Parameters of the low ionosphere at night deduced from parachute borne blunt probe measurements, Space Research VII, North-Holland Publishing Co., Amsterdam, 1967.

Hale, L. C., Positive ions in the mesosphere, COSPAR Symposium on Lower Ionosphere (Proceedings), Akademie Verlag, Berlin, 219, 1974.

Hale, L. C., Private Communication, 1975.

Hale, L. C., D. P. Hoult, and D. C. Baker, A summary of blunt probe theory and experimental results, Space Research VIII, North-Holland Publishing Co., Amsterdam, 320, 1968.

Hale, L. C., D. P. Hoult, and R. G. Willis, Preliminary results of rocket measurements of D-region ion density, Electron Density Profiles in Ionosphere and Exosphere, edited by J. Frihagen, North-Holland Publishing Co., Amsterdam, 108, 1966.

Israel, H., and L. Schulz, The mobility-spectrum of atmospheric ions--principles of measurements and results, Terr. Magn. Atmos. Elec., 38, 285, 1933.

Knoll, M., J. Eichmeier, and R. W. Schön, Properties, measurement and bioclimatic action of "small" multi-molecular atmospheric ions, Advances in Electronics and Electron Physics, edited by L. Marton, Academic Press, New York, 177, 1964.

Leiden, S. F., Private Communication, 1975.

Loewenstein, M., J. Paddock, I. Poppoff, and H. Savage, In-situ NO and O_3 measurements in the lower stratosphere from a U-2 aircraft, Prof. Third Conf. CIAP, DOT-TSC-OST-74-15, 213, 1974.

Meira, L. G., Rocket measurements of upper atmospheric nitric oxide and their consequences to the lower ionosphere, J. Geophys. Res., 76, 202, 1971.

Mitchell, J. D., An experimental investigation of mesospheric ionization, Scientific Report No. 416, Ionosphere Research Laboratory, The Pennsylvania State University, 1973.

Mitra, A. P., Nitric oxide in the mesosphere and its variation, Space Research IX, North-Holland Publishing Co., Amsterdam, 418, 1969.

Mitra, A. P., and J. N. Rowe, Ionospheric effects of solar flares - VI. Changes in D-region ion chemistry during solar flares, J. Atmos. Terr. Phys., 34, 795, 1975.

Neher, R. V., Cosmic-ray particles that changed from 1954 to 1958 to 1965, J. Geophys. Res., 72, 1527, 1967.

Nicolet, M., and A. C. Aikin, The formation of the D-region of the ionosphere, J. Geophys. Res., 65, 1469, 1960.

Paltridge, G. W., Experimental measurement of the small-ion density and electrical conductivity of the stratosphere, J. Geophys. Res., 70, 2751, 1965.

Patel, C., E. Burkhardt, and C. Lambert, Spectroscopic measurements of stratospheric nitric oxide and water vapor, Science, 185, 1173, 1974.

Pedersen, A., Measurements of ion concentrations in the D-region of the ionosphere, Uppsala Jonosfärobservatorium Report No. 15, Uppsala Ionospheric Observatory, 1966.

Pontano, B. A., and L. C. Hale, Measurements of an ionizable constituent of the low ionosphere using a Lyman alpha source and blunt probe, Space Research X, North-Holland Publishing Co., Amsterdam, 208, 1970.

Rose, G., and H. V. Widdel, Results of concentration and mobility measurements for positively and negatively charged particles taken between 85 and 22 km in sounding rocket experiments, Radio Sci., 7, 81, 1972.

Rose, G., H. V. Widdel, and R. Borchers, A mesosphere payload to measure the concentration and mobility of positive and negative ions in the height range between 72 and 40 km, Journal of the British Interplanetary Society, 24, 215, 1971.

Rusch, D. W., Satellite ultraviolet measurements of nitric oxide fluorescence with a diffusive transport model, J. Geophys. Res., 78, 5676, 1973.

Schiff, H. I., Measurements of NO, NO_2 and HNO_3 in the stratosphere, Can. J. Chem., 52, 1536, 1974.

Sechrist, C. F., Jr., A theory of the winter absorption anomaly at middle latitudes, J. Atmosph. Terr. Phys., 29, 113, 1967.

Shapley, A. H., and W. J. G. Beynon, Nature, 206, 1242, 1965.

Siddiqui, Javed M. H., Ultraviolet source for rocket measurements of nitric oxide in the upper atmosphere, Scientific Report No. 421E, Ionosphere Research Laboratory, The Pennsylvania State University, 1974.

Strobel, D. F., Nitric oxide in the D-region, J. Geophys. Res., 77, 1337, 1972.

Tisone, G. C., Measurements of NO densities during sunrise at Kauai, J. Geophys. Res., 78, 746, 1973.

Toth, R., C. Farmer, R. Schindler, O. Raper, and P. Schaper, Detection of nitric oxide in the lower stratosphere, Nature, 244, 7, 1973.

Watanabe, K., Photoionization and total absorption cross section of gases, J. Chem. Phys., 22, 1564, 1954.

Watanabe, K., Ultraviolet absorption in the upper atmosphere, Geophysics, 5, Academic Press, New York, 153, 1958.

Whipple, E. C., An improved technique for obtaining atmospheric ion mobility distributions, J. Geophys. Res., 65, 3679, 1960.

Whitten, R. C., and I. G. Poppoff, Physics of the Lower Ionosphere, Prentice-Hall, Inc., Englewood Cliffs, 1965.